South Dakota State University

Open PRAIRIE: Open Public Research Access Institutional Repository and Information Exchange

Electronic Theses and Dissertations

2021

Bio-Inspired Materials for Electrochemical Sensors

Matthew Joseph Hummel

BIO-INSPIRED MATERIALS FOR ELECTROCHEMICAL SENSORS

BY MATTHEW JOSEPH HUMMEL

A dissertation submitted in partial fulfillment of the requirements for the

Doctor of Philosophy degree

Major in Biological Sciences

Specialization in Agricultural and Biosystems Engineering

South Dakota State University

2021

DISSERTATION ACCEPTANCE PAGE

Matthew Hummel

This dissertation is approved as a creditable and independent investigation by a candidate

for the Doctor of Philosophy degree and is acceptable for meeting the dissertation

requirements for this degree. Acceptance of this does not imply that the conclusions

reached by the candidate are necessarily the conclusions of the major department.

Zhengrong Gu
Advisor   Date

Van Kelley
Department Head   Date

Nicole Lounsbery, PhD
Director, Graduate School   Date

This dissertation is dedicated to many individuals who made my academic career fulfilling and successful. First, I dedicate this to my wife, Ailin, for her unwavering commitment and support. As we both have pursued our doctoral degrees, you have been understanding of the rigor and stress that research can bring as well as a constructive critic who has always driven me to improve. Much of the work present in this dissertation is a direct result of our discussions. You are always kind to me; you are my very best friend.

I also dedicate this work to my parents, Laura and Kelly Hummel, my siblings, Alexandra, Benjamin and William, and my brother-in-law David for their encouragement to pursue and complete my higher education and always believe in my ideas. I was lucky enough to spend the entirety of my education with them nearby, which has both helped me step away from my work when needed and has stimulated my creativity. Each of you are intelligent, kind people who have helped me every step of the way.

Finally, this work is dedicated to my adviser Dr. Zhengrong Gu, and my lab mates Shun Lu, Hongxing Jia, and Matthew Cole, thank you for your teaching, your patience, and your willingness to help me. As a biologist transitioning into the field of electrochemistry and materials science, I could not have chosen a better lab for learning the fundamentals while also being given the freedom to pursue my own ideas and funding.

ACKNOWLEDGEMENTS

To the Agricultural, Biosystems, and Mechanical Engineering Department at South Dakota State University, I wish to express my deepest gratitude for providing an environment in which I could learn a new discipline while interacting with scientists, lecturers, producers, and students with whom I could exchange ideas, propose projects, and learn more about how agricultural engineering is truly at the cutting edge for the future of innovation.

TABLE OF CONTENTS

LIST OF FIGURES AND TABLES

CHAPTER 1 FIGURES

CHAPTER 2 FIGURES

CHAPTER 2 TABLES

CHAPTER 3 FIGURES

CHAPTER 3 TABLE

CHAPTER 4 FIGURES

CHAPTER 4 TABLES

APPENDIX A FIGURES

APPENDIX B FIGURES

ABSTRACT

BIO-INSPIRED MATERIALS FOR ELECTROCHEMICAL SENSORS

MATTHEW JOSEPH HUMMEL

2021

Electrochemical biosensors are a rapidly growing research area that has greatly improved its specificity, accuracy, and precision in the detection of biomolecules in contemporary literature and industry alike. Typically, these systems exist in a three-electrode conformation with a working electrode functioning as the anode, a counter electrode functioning as the cathode, and a reference electrode allowing for the control of potential in the system. The method by which these sensors work is through the sharing of electrons via redox reactions with the target molecule and the working electrode or modifications on its surface. By exploiting the function of biomaterials that participate in natural substrate-binding redox phenomena, new opportunities for detecting critical molecules in complex situations can be created. In this dissertation, three distinct electrochemical biosensors were created by mimicking natural phenomena and implementing materials that directly or indirectly participate in the corresponding reactions.

First, a dopamine sensor was created via a composite of lignin-derived graphene oxide and the marine algae-derived polysaccharide kappa carrageenan. Different ratios of GO, a known electrooxidizing catalyst of dopamine, with kappa carrageenan were used to create a binder-free film for dropcasting on the working electrode. It was designed on the principle of its interactions with the nervous system when injected in rats to induce

analgesia, interfering with standard dopamine behavior. The system demonstrated a linear range of 1 - 250 μmol L^{-1} and a limit of detection of 0.14 μmol L^{-1} (s/n=3).

In the second chapter, a sensor for the human and animal health hazard nitrite was constructed using the transition metal sulfide NiS. Transition metal sulfides are the catalytic center for nitrite oxidation to nitrate in nitrogen fixing bacteria found in the environment. This section utilized a novel electrodeposition method for creating a binder-free layer of NiS on the surface of the glassy carbon electrode. This system demonstrated a linear range of 0.04 – 1 μM, 1 – 5.3 μM and a detection limit of 0.01 μM.

For the final chapter, a novel sensor was created for the cryoprotective sugar trehalose, an indicator of bacterial contamination in meat and produce without any electrochemical assay precedent. This system utilized the interactions found between alkali earth metal ions and trehalose in which the two molecules form complexes. Magnesium phthalocyanine, which is a commercially available dye, as well as synthesized magnesium tetraphenylporphyrin and calcium tetraphenylporphyrin were implemented as drop-casted coatings on the working electrode to electrodeposit trehalose on the surface and detect its oxidation via squarewave anodic stripping voltammetry in the complex media Luria-Bertani broth. The system was also used to gauge fluctuations in *E. coli* in broth by autoclaving the cultures and directly testing the media containing lysed bacteria. The system demonstrated a linear range of 0.25 mM – 100 mM, with magnesium *meso*-tetraphenylporphyrin exhibiting the highest repeatability.

CHAPTER I: INTRODUCTION

Section 1.1 An Introduction to Electrochemical Biosensors

1.1.1. Background and History of Electrochemical Biosensors

Detecting all manner of biological substances is a critical part of ensuring food, travel, healthcare, and other aspects of daily life are safe and consistent. Much of what maintains a high quality of life is owed to accurate and precise diagnostic tools [1]. These biosensors, as they are termed, have been rooted in agriculture and medicine for decades [2]. A biosensor can be qualitative or quantitative and "senses" its target molecule through interactions with a chosen substrate that elicits a perceptible change [3]. This can present as a change in color, an emission of fluorescence, alteration of viscosity of the sample, or a change in electrochemical properties among others [4, 5]. The latter method has gained popularity in recent literature because it offers the distinct advantages of scalability, stable components, and rapid results.

The earliest cases of applied electrochemical sensors employed two electrodes but encountered the significant issue of not being able to accurately control applied potential across the two electrodes [6, 7]. This was further improved through the advent of the three-electrode system in 1942 by Archie Hickling, which allows control of the applied potential via a material with clearly defined redox events [6]. Initially, a mercury drop electrode was used as a reference electrode due to its predictable oxidation at ~+0.2 V, but it created issues for the analysis of other molecules that oxidized in a similar range [8]. As the materials science field develops and expands the use of new materials, Ag/AgCl became a predominant choice for the reference electrode and is currently used

due to its predictable redox behavior and relative inertness and safety in a variety of media [9]. As such, electrochemical methods will often report their potentials versus an Ag/AgCl electrode. Due to this versatility and ease-of-use, electrochemical devices have transitioned from laboratory techniques to products that improve the quality of life.

1.1.2. Modern Electrochemical Sensors and the Obstacles They Face

Previously treated as an analytical technique with little use outside of a lab, electrochemical devices have attracted a growing interest as their use for point-of-care devices for medical and sanitary diagnostics [10, 11].

Figure 1. 1. A comparison of Medisense's ExacTech pen and card electrochemical blood glucose system commercially released in 1987 versus today's FreeStyle Libre continuous glucose monitoring system

One of the first instances of an electrochemical sensor transitioning from the laboratory to home-use is the coulometric glucometer. As early as 1987, electrochemical blood glucose monitoring has been accomplished with low volumes of blood due to a glucose oxidase-based electrochemical sensor that relies on the redox signature of glucose

oxidase binding to its substrate glucose and generating an oxidation peak [12]. Medisense's ExacTech was the one of first electrochemical system to commercially offer this type of detection [13]. Currently, continuous glucose monitors (CGMs) exist based on coulometric detection of glucose oxidase activity in interstitial fluid via a transdermal microneedle patch that samples via microcapillaries such as the Abbott Freestyle Libre (**Fig. 1.1. right).** Now, electrochemical sensors have started to encroach on other scientific and commercial fields, simplifying processes that were once restricted to labs and hospitals.

One notable biosensing example that emphasizes the promise of electrochemical sensors at home and in the field is the electrochemical gas sensor for monitoring sanitation and emissions of companies. The company Honeywell, among others, has had electrochemical sensors for multi-detection of volatile organic compounds, CO-, and other noxious gases for >30 years based on amperometric detection [14]. Such sensors have grown to dominate the markets that demand for systems that require little direct input and maintenance from the operator so that they can run continuously.

Electrochemical sensors today are poised to enter a growing market but still encounter drawbacks that limit their applicability to most commercial sensing functions. Mainly, the issue of interferents interacting with modifications to the electrode slows electrochemistry's progress into commercial use [15]. When relying on specific biocomponents like antibodies and enzymes, electrochemical sensors are limited to the parameters at which these components are stable and cannot easily exceed their detection

limits in traditional settings as a result [16].

Section 1.2. The Fundamentals of Applied Electrochemistry

1.2.1. Redox Behaviors and the Nernst Equation

Electrochemistry, as it pertains to biosensors, is the study of the flow of chemical energy in the form of electrons as it passes from a chosen reactive species to an electrode or the modification on its surface [17]. **Figure 1.1** illustrates a reduction/oxidation (redox) event and demonstrates how the reaction needs an electron donor and an electron acceptor to proceed. If considering this process from the perspective of electrochemical sensors, "A" can be interpreted as the analyte you are trying to detect and "B" as the electrode that interacts with said analyte. The applied potential from the potentiostat drives the flow of electrons and elicits the reaction on the surface of the working electrode. The subsequent exchange of electrons results in a signal that can directly or indirectly correlate with the reaction depending on factors like diffusion, binding affinity for the substrate, pH, and temperature [18-20].
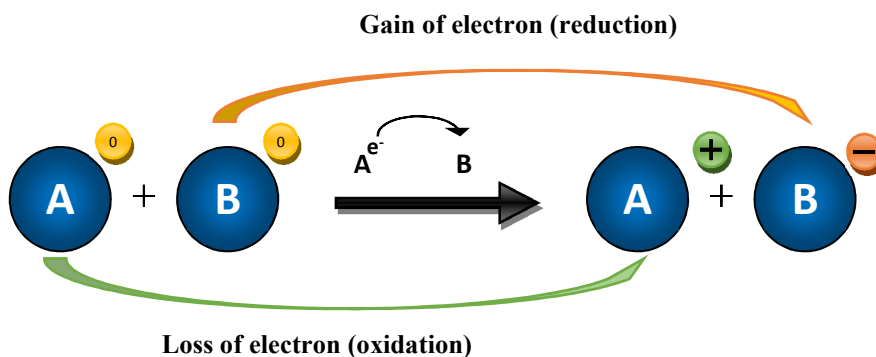
Figure 1. 2. An illustration of how a reduction/oxidation (redox) reaction proceeds with A (the electron donor) and B (the electron acceptor) representing two reactants.

As with all electrical systems, electrochemical sensors must obey Ohm's Law, a fundamental part of the behavior of electricity which is given in **Equation 1.1A and 1.1B**.

Direct Current: $\qquad V = IR$ $\qquad\qquad$ **Equation 1.1A**

Alternating Current: $\quad E = IZ$ $\qquad\qquad$ **Equation 1.1B**

Where V is voltage or potential for DC and E is potential for AC (measured in volts), I is current (measured in Amperes), R is resistance (measured in Ω), and Z is impedance (also measured in Ω, but with frequency as a component). For AC currents, Ohm's law may not be as simple due to the influence of certain elements in a circuit such as inductors or capacitors. To compensate, values may be imaginary numbers calculated using features from the AC wave form such as phase angle and frequency [21, 22].

By accounting for these factors, assumptions can be made about the behavior of an electrochemical system based on key equations. One such equation is the Nernst Equation (**Eq. 1.2A and 1.2B**).

Half Cell Reduction: $\qquad E_{red} = E_{red}^{\ominus} - \frac{RT}{zF} \ln \frac{a_{Red}}{a_{Ox}}$ $\qquad$ (**Equation 1.2A**)

Full Cell: $\qquad E_{cell} = E_{cell}^{\ominus} - \frac{RT}{zF} \ln Q_r$ $\qquad$ (**Equation 1.2B.**)

Where E_{red} is the actual half-cell reduction potential, $E_{red}^{\ominus}$ is the standard half cell reduction potential, E_{cell} is the actual cell potential (electromotive force) at desired

temperature, $E_{cell}^{\ominus}$ is standard cell potential, R is the universal gas constant (R =

8.31446261815324 J K^{-1} mol^{-1}), T is the temperature in Kelvins, z is the number of

electrons transferred in the full cell reaction, F is the Faraday constant in coulombs per

mole of electrons (F = 96485.3321233100184 C mol^{-1}),a_{Red} is the activity of the reduced

form of the relevant species and a_{Ox} is the activity for the oxidized form of the relevant

species in mol L^{-1}, Q_r is the reaction quotient of the cell [23-25].

Through use of the Nernst equation, we can determine the potential at which an analyte

of known characteristics will reduce. Conversely, if we already know the reduction

potential and confirm it with various techniques such as voltammetry, we can calculate

the standard potential, number of electrons transferred, and approximate activity of the

redox reaction (usually in concentrations of reactants in mol L^{-1}). Given its great utility,

the Nernst equation is a central feature of electrochemistry and often accounted for in the

design of different electrochemical systems. It is also intrinsically connected to another

central equation of electrochemistry: the Randles-Sevcik equation.

1.2.2.The Randles-Sevcik Equation

By utilizing common electrochemical techniques such as sweeping (linearly increasing

and/or decreasing) voltage while monitoring current, we can make assumptions about the

electrochemical environment and apply them to the Randles-Sevcik equation to help us

determine the role of the diffusion of our chosen analyte across the surface of the

electrode. This is useful because most electrochemical sensors rely on these predictable

behaviors for extrapolating data such as current sensitivity of the electrode to the analyte

over a period of time [26]. The equation (**Eq. 1.3.**), simplified for solutions at 25°C,

considers current obtained at maximum as well as the number of electrons transferred

between the active chemical species in a redox event (typically one).

For a solution at 25°C: $i^p = 2.69 \; x \; 10^5 \; n^{\frac{3}{2}} A D^{\frac{1}{2}} C v^{\frac{1}{2}}$ (**Equation 1.3.**)

Where i^p is current maximum in Amperes, n is number of electrons transferred in the

redox event, A is electrode area in cm^2, D is diffusion coefficient in cm^2 s^{-1}, C is

concentration in mol/cm^3, and v is scan rate in V/s [27, 28].

The Randles-Sevcik has utility to characterize diffusion-related phenomena for multiple

methods in electrochemistry and is frequently referenced to justify certain behaviors of

reactions such as asymptotic relationships of current with time, Warburg impedance in

AC impedance spectroscopy, and many other phenomena commonly witnessed while

characterizing electrochemical systems [29, 30]. Using the Nernst equation and the

Randles-Sevcik equation, electrochemistry has become a powerful tool for studying the

dynamics of complex chemical interactions and quantifying these phenomena accurately

and precisely.

1.2.3. Utility of Electrochemistry: What Can It Detect?

Because of the variety of materials and methods available in electrochemistry, we can

characterize reaction kinetics, reversibility, and inhibitory effects of different materials in

a single system through the use of voltammetric methods among others [31]. In

biosensing, this affords a relatively new method to traffic redox reactions from enzymatic

processes, a core component of biological phenomena [32]. Being that they are not

limited to redox reaction detection, biosensors can also be capacitive. This means the

system relies on a change in electrochemically active surface area to gauge binding of

analyte to electrode which causes a shift in charging and discharging behavior when

treated like a capacitor [33-35].

This same type of principle can be applied to a different type of electrochemical

biosensor; one based on impedance or resistance. In this system, changes the analyte

causes to the electrode or its coating cause a change in the AC impedance measurement

(meaning the current used to detect resistance is applied with a frequency rather than a

direct current, measured in Ω). This method can be particularly useful when calculating

different features responsible for this resistance such as resistance of the buffer which the

experiment takes place in, resistance of the charge transfer from analyte to electrode, and

resistance caused by diffusion-related behavior across the surface of the electrode [36,

37]. To further delve into the intricacies of these methods, it is best to first know the roles

and compositions of each of the electrodes in the system.

Section 1.3. Anatomy of a Three-Electrode System

1.3.1. Establishing the Role of Each Electrode

The hallmark of modern electrochemistry is the three-electrode system which affords the

user the control over the relationship of potential versus time. This is accomplished

through the unique properties exhibited by each electrode. The standard conformation of

a three-electrode electrochemical cell as well as a screen-printed electrode are shown in

Figure 1.3. Each electrode's role in the electrochemical cell is as follows:

- A working electrode (anode, [-]) [abbreviated as WE] for detecting an electrochemical event, this electrode is usually modified with a substrate to induce a desired reaction with an analyte in the aqueous solution.

- A counter electrode (cathode, [+]) [abbreviated as CE] for measuring the current and completing the circuit of the working electrode.

- A reference electrode [abbreviated as RE] consisting of a material with a known reduction potential (usually Ag/AgCl or silver calomel) used to control and monitor voltage.
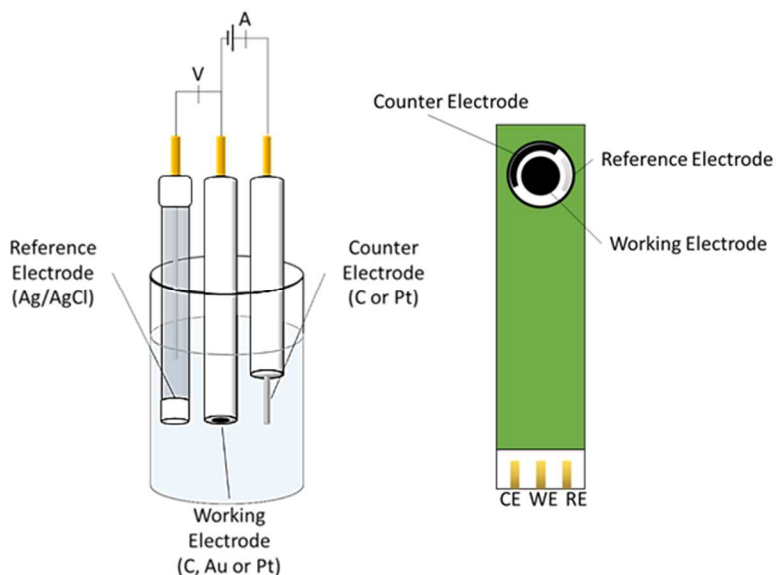
Figure 1. 3. A standard three-electrode system in an electrochemical cell consisting of a reference electrode, working electrode, and counter electrode respectively (left) and the same system on a screen-printed electrode, which are used with low volume droplets an

1.3.2. Innovation with the Three-Electrode System

As electrochemical sensors and their associated platforms have matured, new options for easy-to-use technology have become available. One major innovation in the field is the screen-printed electrode and its derivatives. Consisting of three conductive ink electrodes that are printed on a ceramic or polymer substrate, screen-printed electrodes allow users to work with minute liquid samples (~50μL). **Figure 1.3.** depicts a typical three-electrode system on the left and the newer, one-time use screen-printed electrode on the right. Both operate by standard electrochemical methods, but the screen-printed electrodes are generally single use, diminishing in quality after fouling of the electrode. Conversely, the standard three-electrodes can be polished with a series of micron-sized alumina powders and then reused repeatedly but required large enough volumes of buffer to be completely immersed.

Section 1.4. An Overview of Voltammetric Methods

1.4.1. Principle of Voltammetry

Voltammetry can be defined as controlling the relationship between potential, current, and time in an electrochemical cell via different wave forms of potential versus time [38]. As previously mentioned, voltammetric methods are made possible by the reference electrode in the three-electrode system and can vary from characterization to quantification depending on the chosen waveform of potential vs. time.

1.4.2. Overview of Different Voltammetric Methods

Voltammetry and its associated methods can reveal vastly different aspects of an electrochemical sensing environment due to the waveform of potential versus time. With simpler methods, where voltage is increased and decreased in a linear pattern, characteristics such as capacitance of the electrode, locations of oxidizing and reducing potentials, and stable potential windows of your chosen buffer can be easily discovered [39]. These methods can also lack the specificity, sensitivity, and quantitative nature of more complex methods and are generally best for characterization of the electrode, analyte, and buffer rather than direct quantification in most instances [40, 41].

The following methods are examples of the great utility and versatility of voltammetry as well as its potential shortcomings. The format of the following figures can be interpreted as the potential vs. time waveform provided by the potentiostat on the left and the current vs. potential elicited from that waveform on the right.
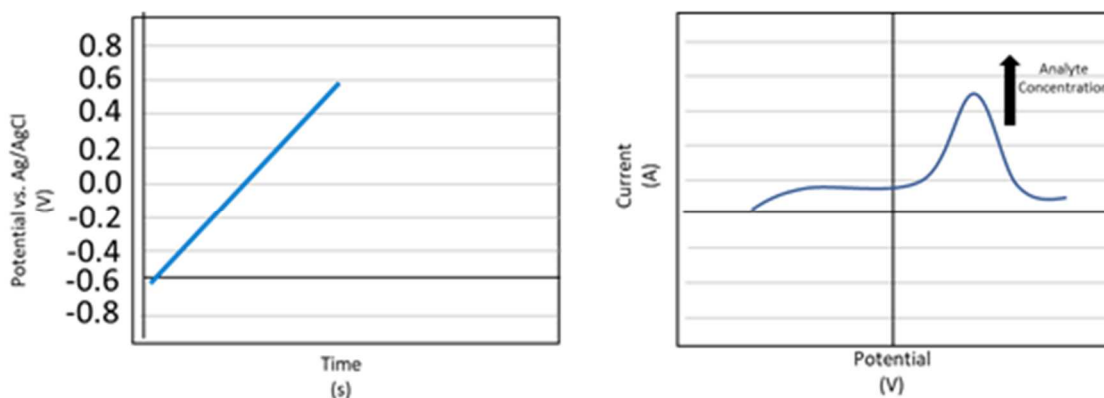
Figure 1. 4. Linear sweep voltammetry with potential vs. time relationship (left) and an example of current vs. potential resulting from this method in the presence of an oxidizing species (right)

Linear-Sweep Voltammetry (LSV) – LSV (**Fig. 1.4.**) is the electrochemical method in which potential is increased or decreased from point A to B in a linear function. Being one of the simplest voltammetric techniques, LSV offers great utility in assessing where reactions occur within a potential window but lacks the quantitative aspect of other more complex methods in voltammetry. One notable task LSV can accomplish is determining the overpotential of a reaction.

Overpotential, which can also be termed as the thermodynamic potential, is the potential difference (in volts) between equilibrium of the species where current is low on the voltammogram and the peak current at which the catalyst material on the electrode is facilitating a redox reaction [42]. The relationship between catalyst or electrode behavior towards an analyte and the voltammogram are not always easily interpreted visually. Conveniently, the Tafel equation can help quantify these changes and display better mechanistic properties of a reaction and its efficiency (**Eq. 1.4)** [43].

$$\text{For anode and cathode respectively: } \eta = \pm A \times \log_{10}\left(\frac{i}{i_0}\right) \quad \textbf{Equation 1.4.}$$

Where η is overpotential (in V), A is the Tafel slope (slope of potential/log current in mV/current decade, e.g., 10^{-5}A to 10^{-4}A on a log scale), i is current density (A/cm^2), and i_0 is exchange current density (A/cm^2, current density when there are no redox peaks at around 0 V). Tafel curves are useful because they can help explain whether a reaction favors a reduced or oxidized form of the reactant as well as determine what the rate of the reaction and corrosion potential is when used in tandem with other electrochemical

methods. This is determined via the charge transfer coefficient, which can be calculated with the Butler-Volmer equation [44]. The charge transfer coefficient is useful in electrochemistry as it can tell us how electrons move at the interface of the electrode and electrolyte, which could change in response to binding events as in a biosensor. One must, however, account for the splitting of water and the Tafel curve dynamics that are associated with that reaction in aqueous media [43]. With an understanding of LSV's utility and features, one can easily transition to a closely related, powerful method known as cyclic voltammetry (CV).
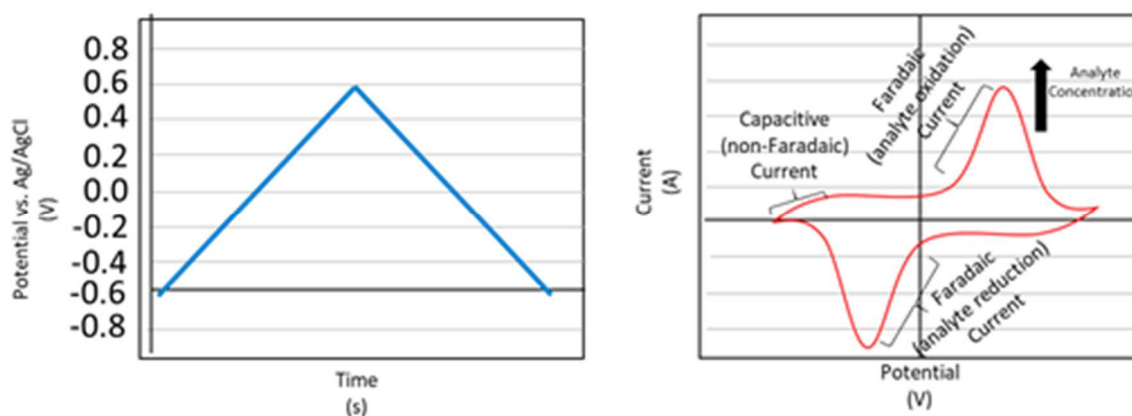
Figure 1. 5. Cyclic voltammetry with potential vs. time relationship (left) and current vs. potential resulting from this method in presence of a redox species (right)

Cyclic Voltammetry (CV) – CV is very similar to LSV in that both utilize a linear change in potential from point A to point B, creating a potential window (**Figure 1.5**). Where they differ is that CV charges from point A to point B and then "discharges" from point B to point A for a set number of cycles. By using cyclic voltammetry, one can witness the oxidation event (forward scan) and the reduction event (reverse scan) in the same plot and gauge how it changes from cycle to cycle. This attribute is particularly

valuable because cyclic variation in CV is often a sign of instability on the electrode or in the solution[45].

Additionally, CV creates a unique geometric "duck" shape when redox peaks are present. Because of this, reversibility of the reaction can be assessed by calculating the half wave potential or $E^{1/2}$, which is the potential on the voltammogram halfway between the reduction peak and oxidation peak respectively and can be a good proxy for standard cell potential E^0 [46]. This can change depending on factors such as indicator used, reference electrode used, and the type of buffer in which the reaction is taking place.

Another useful feature of CV as it pertains to biosensing is its ability to quantify capacitance, which does not require the presence of redox peaks. This is accomplished by calculating the area inside a single cycle of the cyclic voltammogram that forms a geometric shape. The area corresponds directly to the capacitance of the system in Farads, also known as $\frac{Amperes \times seconds}{Volt}$. Phenomena that can change the capacitance are typically associated with the expansion of the electrochemically active surface area on the electrode, which can be either increased or reduced by species binding/dissociating from the surface when a reaction with an analyte takes place. It should be noted, however, that electrochemically active surface area may not necessarily correlate directly to actual surface area as it is a measure of the surface area that participates in the flow of electrical energy.

By assessing the change in capacitance via CV, we have a powerful tool for measuring change on the surface of an electrode. This is especially useful if the electrode has anti-fouling agents such as bovine serum albumin on the surface to prevent the binding of any non-specific material, allowing for a specific probe with a known capacitance where one can monitor the change in peak current retention over a number of cycles. Despite all of its potential, cyclic voltammetry still lacks the element of direct quantification and is best used in tandem with other methods. One appropriate method for direct quantification of a redox species is differential pulse voltammetry.
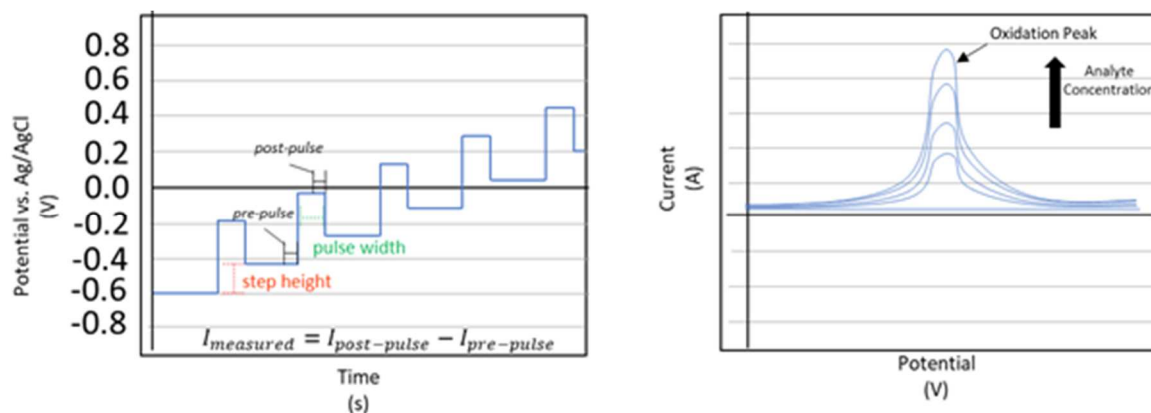
Figure 1. 6. Differential pulse voltammetry with potential vs. time relationship (left) and current vs. potential resulting from this method in presence of an oxidizing species (right)

Differential Pulse Voltammetry (DPV) – Differential pulse voltammetry is one of the most widely implemented methods of electrochemistry for direct quantification of redox species using a complex waveform of potential vs. time. It is a derivative of two separate, simpler methods used in tandem; being staircase voltammetry (where the potential is increased in steps) and normal pulse voltammetry (where the potential is pulsed at regularly spaced intervals increasing in intensity) [47]. The resulting waveform, shown in **Figure 1.6**, results in a regular pulse on a steadily increasing potential. Current is then

measured on the pre-pulse and post-pulse periods and the difference between the two readings is reported. This method is sufficiently sensitive for quantitation because it minimizes the capacitive current that LSV and CV show very prominently. Without this capacitive current, subtle reactions such as the binding of an analyte in the femtomolar range, can be reported without the large background of capacitance formed via the physical interfaces of the electrode and the electrolyte.

This method has been implemented with great success for the detection of multiple species at a time, provided their current peak potentials do not overlap. One classic case of this phenomenon is a dopamine, ascorbic acid, and uric acid multi-sensor [48]. All three of these analytes can be found in human blood but are able to be sensed simultaneously, as the different potentials required to detect the respective molecules are approached chronologically. As a result, one can see a peak for ascorbic acid, dopamine, and uric acid respectively in the same run. This has been successfully accomplished in systems with significant modifications to the electrode so that the reacting species' interactions with the coating is specific and highly conductive. Such examples are dopamine detection with metal organic frameworks, transition metal oxides, or amino functionalized graphene [49-51].

While highly useful, DPV has issues that need to be mitigated with design. One issue that cannot be mitigated with design, however, is run-time. DPV is one of the slower methods utilized in electrochemistry as it typically scans between 2-10 mV s^{-1} in potential windows of 200-600 mV for most biosensors [52, 53]. Another prominent issue for DPV

is conductivity. While more sensitive than other methods, DPV needs highly conductive electrodes and coatings to mitigate impedance-related dampening of the signal. Furthermore, DPV is best for systems that rely on pristine environments or modifications to the electrode that prevent non-specific oxidation/reduction. If not considered, side reactions driven by the DPV potential vs. time waveform could elicit undesirable products, producing false positives or noisy background [54].

One potential strategy for this is to use differential pulse stripping voltammetry, which is available when using other similar methods such as square-wave voltammetry. In stripping voltammetry, a potential at which the reactant deposits and concentrates on the surface is held until sufficiently saturated. These deposition steps can be variable and run for as little as 30 seconds or potentially for hours. Then, the DPV program is run, and the layer accumulated on the surface is oxidized/reduced all at once, resulting in a prominent peak that can easily be detected by simpler potentiostat units. This strategy has been particularly effective for the deposition of metal ions such as lead, copper, and cadmium [55, 56]. This method is not limited to metal ions though and can be extended to complex biomolecules [57, 58].

Despite the great usefulness of the variety of electrochemical methods, voltammetric methodology alone cannot accomplish the need for a diverse array of biosensors required for the future. The implementation of new materials, composites, and electrolytes is key to innovating in electrochemical biosensors. While there are many potential inspirations

for new methods of detecting key molecules, finding inspiration in biology could be key to rapidly progressing biosensors from the lab to commercial and home use.

Section 1.5. Bio-inspired Biosensors

1.5.1. Incorporating Enzymes and Antibodies

Inspiration from biological phenomena is not a new concept in biosensors and is actually frequently used in both industry and academia. The aforementioned blood glucometer utilizes glucose oxidase bound to a cellulose strip for coulometric detection of circulating glucose levels. Some electrochemical enzyme-linked immunoassays (ELISAs) function on the same principle as standard ELISAs but instead of quantifying absorbance in a 96-well plate, they quantify an amperometric signal as in DPV or square-wave voltammetry [59]. As a well-established branch of electrochemical biosensors, immunosorbent assays have evolved into complex, unique systems.

One important component of increasing effectiveness of these sensors is controlling orientation of the enzyme or antibody to maximize both binding potential and charge transfer. Studies have accomplished this via UV curing of conductive resins, redox mediators, and field-effect transistor arrays [60-62]. Despite the effectiveness of these techniques in achieving alternative methods for contemporary assays, electrochemical biosensors are not limited to simply borrowing whole macromolecules from organisms and attaching them to the surface of an electrode.

1.5.2. Mimicking structural and electrochemical properties for non-enzymatic assays

Non-enzymatic assays are particularly attractive as a concept in electrochemical

biosensors because they could avoid the shortcomings of enzymes and antibodies such as

pH windows of stability, temperature limitations, binding interferents, and importantly,

cost of preparation [63]. The precedent for non-enzymatic biosensors is great but there is

a common theme of interferent-related loss of sensitivity because materials typically used

for non-enzymatic sensing have a wide range of molecules with which they can react

[64]. Increasing specificity through novel material coatings on the working electrode is a

straightforward method for mitigating these common issues.

Structural modifications to an electrode are an effective option for improving the catalytic

performance of biosensors. In oxidation mechanisms where a particular material's

behavior is well-understood, as in carbon's oxidation of dopamine, certain structures that

lack significant redox activity can be used to expand the surface area and create porous,

heterogenous composites that allow for more efficient catalysis [65]. So long as the

matrix chosen is sufficiently conductive and inert to the desired environment, this

principle can be extended to more complex mechanisms such as the in-vitro or in-vivo

detection of neurochemical modulators in neural tissue grown directly on electrodes [66].

One promising class of materials with biologically active behavior are metal-organic

frameworks (MOFs). MOFs are metal ion nodes surrounded by organic linkages which

form a complex structure that can exist as two-dimensional coatings, uniform

nanoparticles, and star-shaped polymers among others [67]. The unique benefit of these

structures is that they exhibit behavior similar to biosynthesized molecules with metal ligands such chlorophyll or hemoglobin but can be tuned for unique behaviors and interfaces [68]. In this work, biomaterials were utilized for their structural and chemical features that mimicked their utility in nature to create new sensing platforms.

Section 1.6 Bio-inspired Materials in this Dissertation

1.6.1. Chapter 2

In Chapter 2, the expansion of the surface area for lignin-derived activated carbon was investigated. This system was chosen because of several instances in biology where inspiration could be taken. The first inspiration was the Ampullae of Lorenzini, a electrochemical sensory organ in sharks and rays that consists of a series of small pores filled with the conductive glycosaminoglycan keratan sulfate. At the base of this pore lies nerve cells that are stimulated in response to subtle changes in potential caused by thrashing of prey, foraging behavior, and even the heartbeats of potential prey [69].

Because this system has evolved to be highly efficient for many species in the *Elasmobranch* clade, it would stand to reason there are elements of the system that could transpose to electrochemical detection of redox phenomena. However, keratan sulfate was prohibitively costly and difficult to procure for use in large amounts needed for experimentation. To solve this, alternative polysaccharides with similar structural features were investigated. Kappa-carrageenan was chosen as the proxy for keratan sulfate due to its linear disaccharide structure, sulfate functional groups for ion exchange, and aqueous stable structures when formed as hydrogel [70, 71].

To evaluate kappa carrageenan's potential as a proxy for keratan sulfate, it was applied in a dopamine sensing platform in which oxidation was theorized to occur on graphene oxide suspended in the composite.

1.6.2. Chapter 3

In Chapter 3, the role of transition metal sulfides in nitrite oxidation to nitrite was investigated via the compound NiS. Nickel sulfide was chosen due to both its unique structural properties and its similarity to the catalytic centers of the class of enzymes associated with nitrite oxidation for nitrogen-fixing bacteria in the Nitrogen Cycle [72, 73].

Bacteria often utilize transition metals in enzymes due to their excellent catalytic efficiency, but they are toxic in their ionic form and must be contained an organic structure. To serve this function, they generally coordinated to cysteine residues which are rich with sulfur to achieve homeostasis [74]. By directly utilizing a transition metal sulfide electrodeposited on the surface of a conductive carbon material, its efficiency as a catalyst for nitrite could be evaluated against more traditional methods.

1.6.3. Chapter 4

In Chapter 4, the cryoprotectant sugar trehalose was targeted because of its unique interactions with alkali earth metal ions. Trehalose had been found to form soluble complexes with magnesium chloride and calcium chloride when investigated as a route for fortification of dietary needs [75]. In fireflies, it was found to work in conjunction

with magnesium 2^+ ions in magnesium sulfate to stabilize luciferin against thermal inactivation [76, 77].

Verifying its interactions was accomplished by utilizing the alkali earth metal organic compounds magnesium phthalocyanine, magnesium meso-tetraphenylporphyrin and calcium meso-tetraphenylporphyrin as coatings containing a partially bound alkali earth metal ion for pre-concentration followed by oxidation of the sugar.

1.6.4. Foreword

This work attempts to apply biomaterials and their associated behaviors in novel implementations as electrochemical sensors. By utilizing their structural and electrochemical features, biosensing platforms with inspiration derived from natural occurrences were created. In each chapter, a new system is encountered with different electrochemical techniques employed for characterization and quantification of different biomarkers.

CHAPTER 2

Kappa-carrageenan/graphene oxide composite film for electrochemical sensing of

dopamine

Authors: Matthew Hummel, Shun Lu, Zebadiah Nelson, Hongxing Jia, Rajesh Pathak,

Yue Zhou, Zhengrong Gu*

*Corresponding author.

Email address: Zhengrong.Gu@sdstate.edu

Abstract:

A novel electrochemical dopamine sensor was fabricated based on a composite film solely consisting of kappa-carrageenan and hierarchical porous carbon drop-casted onto a glassy carbon electrode in a conventional three electrode system. Graphene oxide was synthesized in a one-step thermal conversion from base-catalyzed alkali lignin. Five ratios by mass of a novel hierarchical porous activated carbon and kappa-carrageenan were studied for dopamine quantification without synthetic binders such as polytetrafluoroethylene. Various tests were performed to explicate structure and electrochemical properties of the films. Utilizing differential pulse voltammetry for detection, the optimized 10:1 ratio system elicited a linear range of 1 - 250 μmol L^{-1} and a limit of detection of 0.14 μmol L^{-1}(S/N=3). Results suggested an effective new combination of materials for non-enzymatic dopamine sensing.

2.1. Introduction

Dopamine (DA), an important neural signaling catecholamine, is a valuable analyte for determining healthy and abnormal functions in the brain and other nervous tissue. Irregularities in its blood serum circulating levels are a hallmark of pathologies such as Parkinson's Disease, Alzheimer's Disease, substance addiction, hypertension, and mental illnesses [78, 79]. DA is a prime candidate for electrochemical detection due to its predictable oxidation at 0.20 V – 0.25 V on carbon material electrodes [80-82]. While there are several methods for the electrochemical DA detection, one of the most reliable is differential pulse voltammetry (DPV) due to predictable potential windows of DA oxidation and a relatively short run-time [83]. Therefore, electrochemical DA sensors based on voltammetry offer great potential as a point-of-care (POC) technology for clinical and home use alike. POC systems could offer rapid, on-site monitoring and simple operation so that hospital staff and at-home patients with minimal training may operate the system on their own safely [84, 85]. Circulating DA levels in a healthy adult are approximately 2.31 nmol L^{-1}, with Parkinson's disease-afflicted individuals at 3.24 nmol L^{-1} [86]. Achieving that level of sensitivity has proven to be difficult unless aided by costly materials such as gold nanoparticles or fluorescent probes[87, 88]. To fabricate a reliable electrochemical system that can accurately sense human serum levels of DA, new materials with unique DA interactions need to be sourced and applied.

Carrageenan is a linear, sulfated disaccharide occurring in high concentrations in several species of red algae and frequently used in food gelling applications. It has proven to be an effective film-forming agent with ion conductivity-enhancing properties in

applications outside of food such as energy storage [89, 90]. Part of this behavior can be attributed to carrageenan's formation of high-surface area, interlocking helices when dissolved in water and allowed to constitute to a gel [71, 91, 92]. One of the most readily available forms of carrageenan is the type kappa-carrageenan (KC). KC contains one sulfate group on the 4' carbon of its α-galactose unit, providing an excellent site for ion transfer [93, 94]. It has long been known to have interactions at the nexus of the nervous and immune systems, primarily in stimulating nociceptors and inducing hyperalgesia (increased sensitivity to pain stimuli) in rat models [95, 96]. Principally, this phenomenon is used to generate edemas for clinical trials, demonstrating a unique set of interactions with dopaminergic signaling, according to several studies [97-99]. This complex interaction provides a unique potential pathway to approach DA sensing work in conjunction with traditional carbon material-based biosensing.

Carbon materials such as graphene oxide (GO) and activated carbon all offer a host of uses in electrochemical biosensing. GO, a 2D sheet of sp^2 hybridized carbon, has garnered much attention in the electrochemical biosensing field due to its extremely high surface area, biocompatibility, and stability in adverse and benign environments [100, 101]. Furthermore, GO can effectively enhance redox reaction signals from the interaction of materials and target molecules adsorbed on its surface [102, 103]. One of the major limiting factors for incorporating GO and GO-like materials into widespread use is its cost and complicated manufacture from pristine graphite by Hummer's method [104]. However, new methods utilizing biomaterials as a source are being introduced to GO manufacturing processes. Many of these methods rely on Ni catalytic

thermochemical conversion or chemical vapor deposition [105, 106]. As an

electrochemical DA sensing material, carbon materials like GO and porous carbon have

led to major breakthroughs in sensitivity and selectivity [51, 106, 107]. Sourcing new

carbon materials for DA in tandem with new polysaccharides such as KC could lead to

valuable insights in the development of new POC DA sensors[108].

Herein, we investigated KC and a sheet-like, hierarchical porous activated carbon (GO)

as an electrochemical DA sensor. We utilized our own lignin-derived GO as a novel

conductive carbon material in conjunction with the KC to form a drop-casted composite

film in varying ratios of GO:KC by mass to determine the optimal proportion of carbon

material to polysaccharide for this application. The films were then tested for their ability

to detect DA in phosphate-buffered saline solution at room temperature in neutral pH.

The results were then compared to contemporary electrochemical DA sensors.

2.2 Experimental

2.2.1. Materials

Dopamine HCl, kappa-carrageenan in its sodium salt form, potassium hydroxide flakes,

and alkali lignin were purchased from Alfa-Aesar Chemical Reagent Co, Ltd (USA). No

further purification was required prior to methods described in the experiment.

2.2.2. Synthesis of lignin-derived hierarchical porous activated carbon

Alkali lignin was dissolved in 6 mol L^{-1} KOH in a 3:1 *w:w* ratio. The resulting viscous slurry was applied to Ni foam in a thin layer via spatula and allowed to dry in a vacuum oven overnight at 60 ℃. It was then converted directly on the Ni foam via a high-temperature plasma torch utilizing atmosphere as the plasma source and took approximately 30 seconds to convert from shiny dark brown to matte grey in appearance. The converted material was manually scraped from the nickel foam surface and dried in a vacuum oven at 60 °C for 16 hours. Magnetic separation of nickel particles was implemented to reduce sample contamination post drying.

2.2.3. Preparation of working electrode

1 g of kappa-carrageenan (KC) was dissolved in 100 mL 1% acetic acid to form a 10 g L^{-1} solution (100 mL total). The prepared GO was dispersed in water in a 4 g L^{-1} (100mL total) suspension and sonicated in an ultrasonic cleaning bath for 30 seconds followed by 15 seconds of vortexing to achieve a homogenous black solution. The KC and GO stock solutions were combined in five separate 20 mL aliquots with ratios by solids mass of GO: KC (10:1, 5:1, 1:1) and KC: GO (5:1, 10:1) to investigate optimal material concentrations. 20 uL of each solution was pipetted onto the surface of a polished glassy carbon electrode (3 mm diam.) to completely cover the surface. It was then allowed to dry at room temperature overnight to form a thin, gray film on glassy carbon electrode.

2.2.4. Physical characterization

Crystal structure of GO was analyzed with powder X-ray diffraction (XRD, Rigaku

SmartLab, λ= 1.5418 Å). The scanning electron microscopy (SEM, Hitachi S-3400N,

Japan) was utilized for imaging the sensing film. Transmission electron microscopy

(TEM) was conducted on a JEOL JEM-2100 electron microscope operating at an

accelerating voltage of 200 kV. STEM-Energy Dispersive X-ray Spectroscopy (EDS)

(Oxford) was used for elemental confirmation.

2.2.5. Electrochemical characterization & measurements

All electrochemical measurements were performed on an electrochemical workstation

(CHI-760E, Austin, Texas) with a standard three-electrode system. A glassy carbon

electrode (3 mm in diameter) modified with the GO: KC film, Pt wire, and Ag/AgCl

saturated in a KCl solution were selected as the working electrode, counter electrode, and

reference electrode, respectively. Electrochemical impedance spectroscopy (EIS) was

tested at a frequency of 100 kHz to 0.1 Hz at open-circuit potential with an AC

perturbation of 0.005 V in 0.1 mol L^{-1} PBS solution, 7.1 pH. Cyclic voltammetry, scan

rate 0.050 Vs^{-1}, was tested in the potential range of -0.6 – +0.4 V for 4 cycles.

Electrochemical determination was carried out in 0.1 mol L^{-1} phosphate buffered saline

(PBS) solution, 7.1 pH with 15 uL and 100 uL aliquots of 1 mM DA in 10mL of PBS

solution. 5 seconds of magnetic stirring via stir bar was utilized after the addition of each

dose of DA followed by a 2 second waiting period for solution turbulence to stabilize.

Differential pulse voltammetry (DPV) was chosen to quantify DA concentrations at a

scan rate of 0.004 Vs^{-1}, amplitude of 0.05 V, pulse width 0.0167 sec, pulse period 0.5 sec,

and quiet time of 2 sec in the potential range of 0.0 – 0.5 V. All tests were performed at a

pH of 7.1 at 25 ℃.

2.3. Results and discussion

2.3.1. Film characterization and discussion

The growing need for novel dopamine biosensing materials and matrices was the

motivating factor for us to include kappa-carrageenan in this study. Utilizing a simple

polysaccharide gel like kappa carrageenan is advantageous because it remains stable in

aqueous, neutral pH solutions for months and is sufficiently conductive on its own [109].

This offers great utility for in-field and at-home biosensors because they offer a

reasonable shelf-life for storage and use.
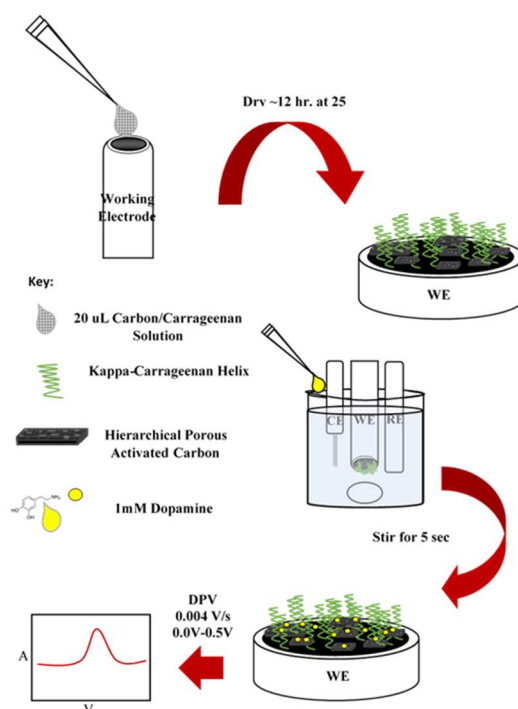
Figure 2. 1. Graphical schematic of the assembly and use of graphene oxide/kappa-carrageenan-based DA

sensor on a glassy carbon electrode using differential pulse voltammetry

Figure 2.1. demonstrates the theorized assembly of the GO and KC on the surface of the

glassy carbon working electrode. SEM images of the film are shown in **Figure 2.5 -2.8**.

According to the SEM images, the GO:KC composite film appears to assemble as

theorized in the **Figure 2.1** schematic. In an aqueous neutral solution with the lignin-

derived GO, the KC helical strands are likely to extend from the surface of the

hierarchical porous activated carbon and thus expands working electrode surface area for

target molecule capture and shown in **Figures 2.2A-C** and **S2.6** [110]. A higher surface

area is evident in **Figure 2.2C** and **Figure 2.2**, where double-layer capacitance was

calculated by cyclic voltammetry in a small, non-faradaic potential window at various

scan rates, using the slope of current density vs. scan rate to confirm increased surface

area [111, 112]. Without the interaction of the GO, KC forms a uniform, small-pored

surface with much lower surface area as in **Figure 2.8**.
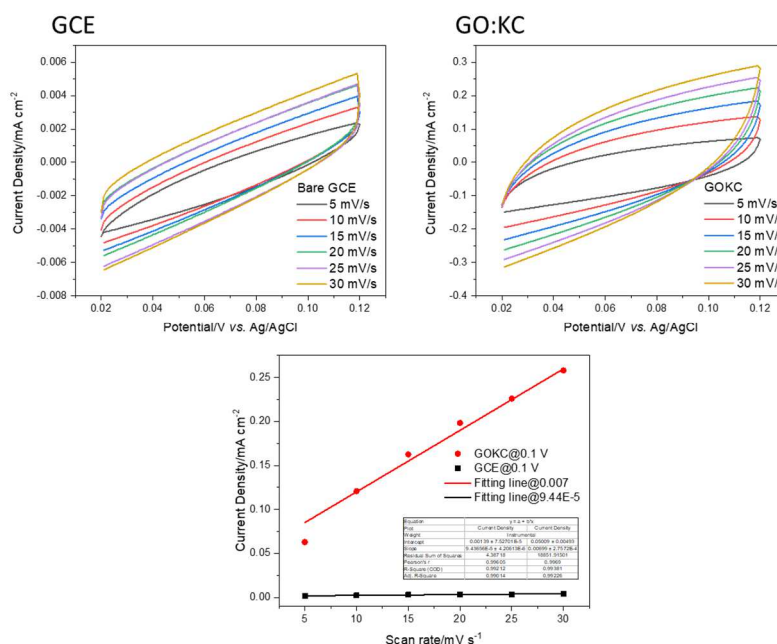
Figure 2. 2. Double-layer capacitance in 1X PBS for determination electrochemically active surface area
by cyclic voltammetry in a narrow potential range, scanning at 5, 10, 15, 20, 25, and 30 mV/s respectively
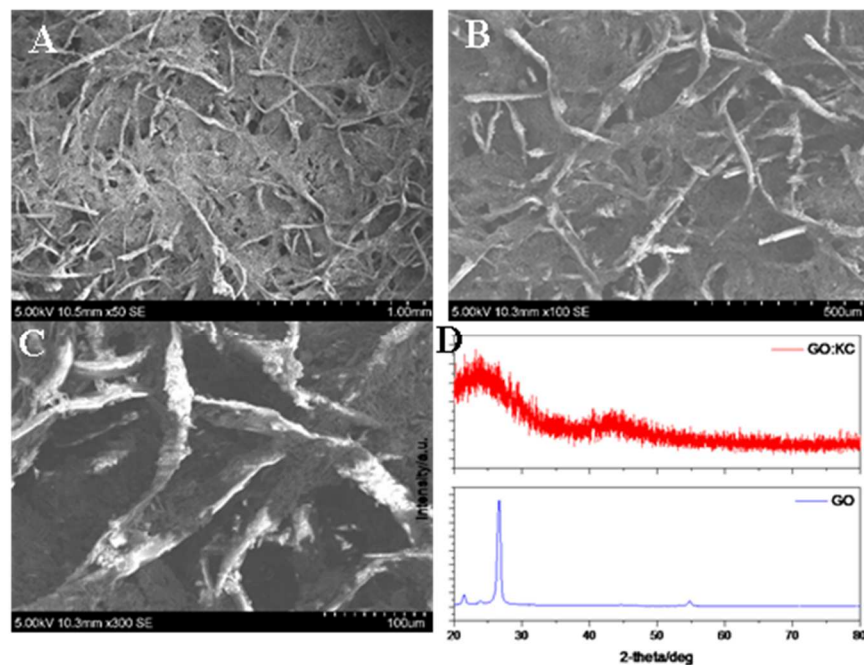
Figure 2. 4. A-C.) SEM images of 10:1 GO: KC @ 1mm scale, 500 um scale, and 100 um scale

respectively D.) XRD spectra of 10:1 GO/KC film and pure graphene oxide (GO))
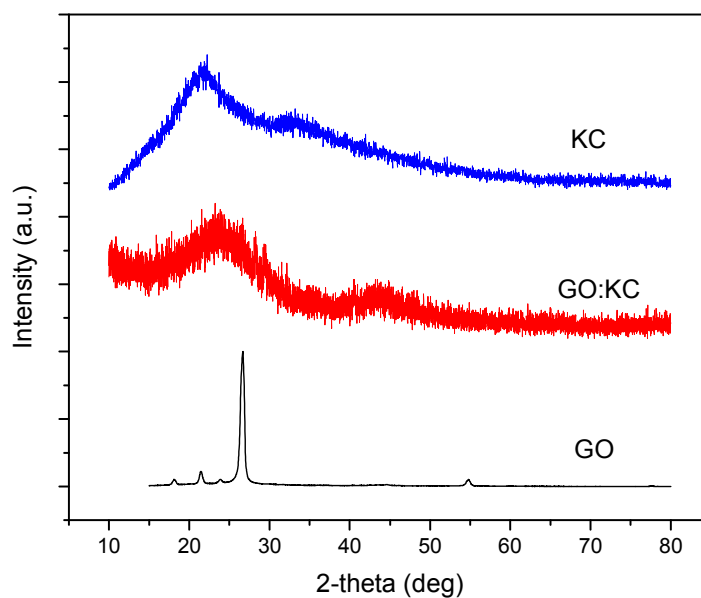
Figure 2. 3. Comparative XRD spectra of kappa carrageenan (KC), lignin-derived

graphene oxide (GO), and the composite film 10:1 GO:KC
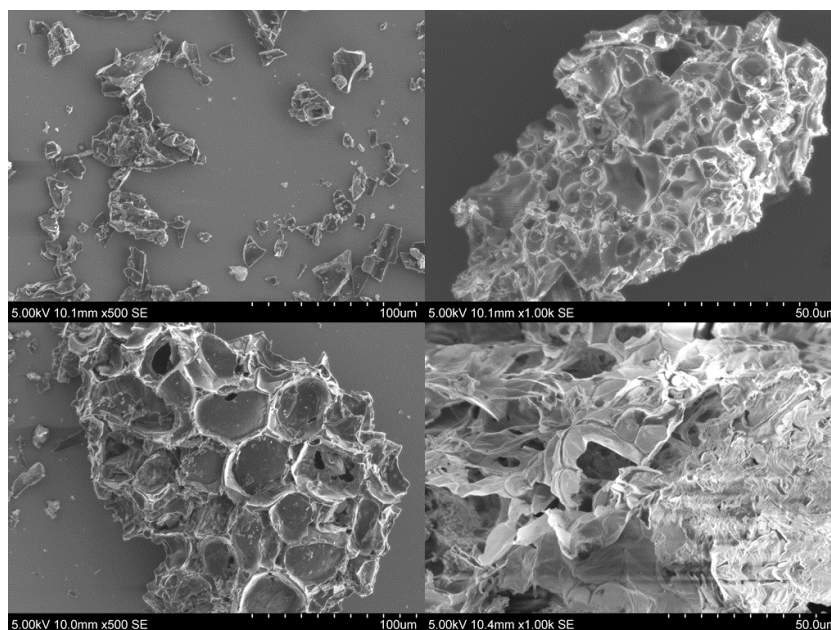
Figure 2. 5. Scanning electron micrographs of pure lignin-derived GO at x500 and x1000 magnificatio
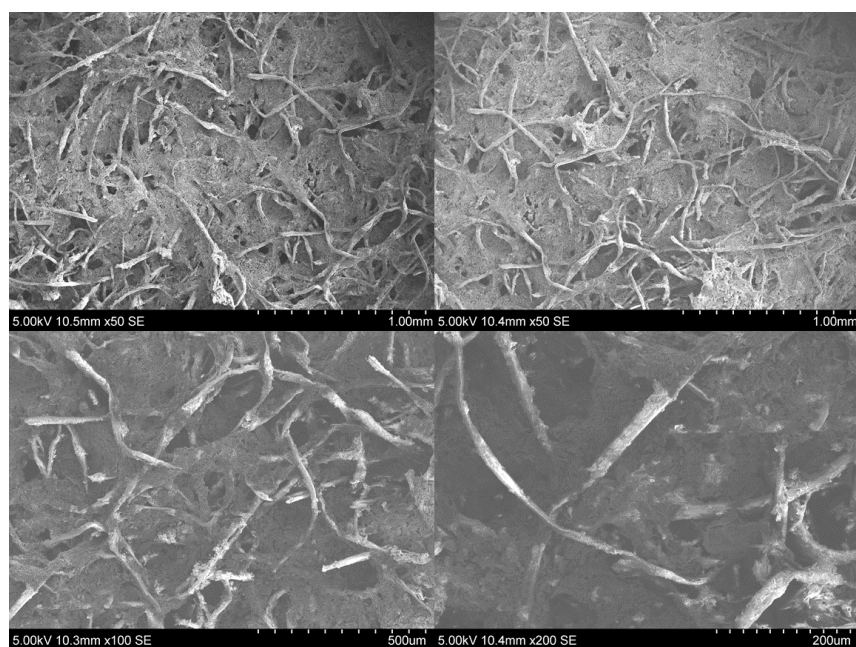
Figure 2. 6. Scanning electron micrographs of 10:1 GO:KC composite film at x50, x100, and x500
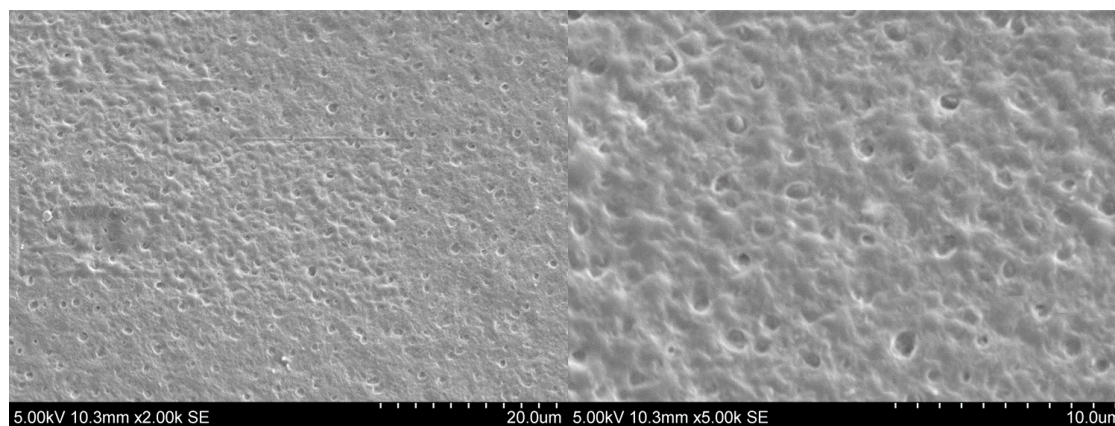
Figure 2. 7. Pure kappa-carrageenan film at x2k and x5k magnification
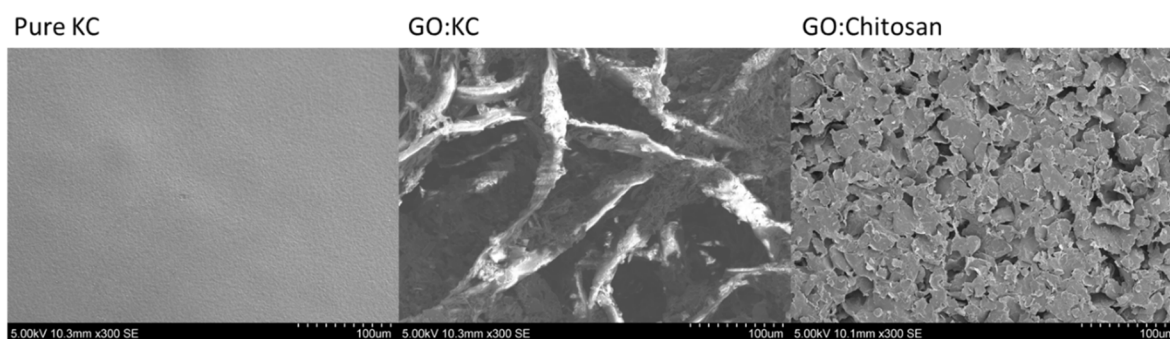
Figure 2. 8. Comparison of a pure kappa carrageenan film, a 10:1 GO: KC film, and a 10:1 GO: Chitosan film at x300 magnification

To confirm chemical composition of the film, X-ray powder diffraction was utilized (**Figure 2.3D** and **Figure 2.4**). The characterization confirmed a signature peaks of GO at 27.1° with a Miller Index of 002 confirm crystal lattice spacing of 0.35nm as shown in HR-TEM (**Figure 2.3B**). In the GO:KC film a broad band peak of $2\theta=24°$ and smaller peak at $2\theta=44°$ were observed, consistent with graphene and/or graphite [113]. KC was also present due to the broad peak at 24 degrees but was likely overshadowed by the broader carbon peak [114-116]. No peaks associated with Ni or NiO were located,

demonstrating a general success of simple magnetic separation of Ni from the sample

[117]. The broad band demonstrates a non-crystalline polymeric structure of the KC

helices [116].
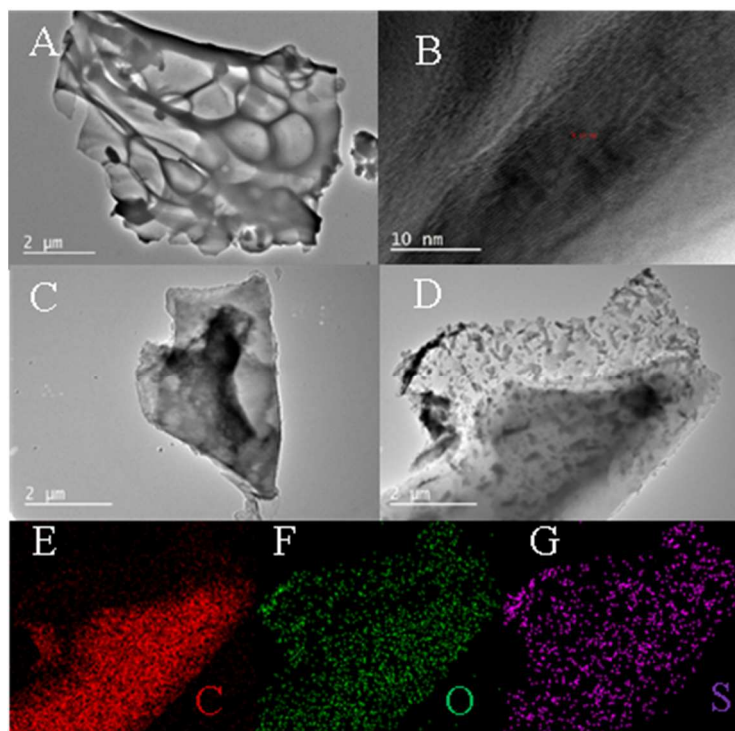
Figure 2. 9. TEM images @ 200kV A.) x2000 magnification of GO, B.) 10 nm scale HRTEM of GO

showing 0.33 nm crystal lattice spacing C.) 2um scale of 10:1 GO:KC film, D.) alternate view of 10:1

The spacing of crystal lattice was characteristic of graphene oxide (**Figure 2.9A**) and

0.35 nm spaced crystal lattice in the carbon material, consistent the XRD 002 reference

[118]. There were nano-sized, regularly interspersed pores in the surface of the kappa-

carrageenan (**Figures 2.9C-D**). The high porosity in the surface of the GO can likely be

attributed to the rapid conversion in atmospheric plasma at high temperatures followed by

rapid cooldown, as referenced in a previous study using comparable, albeit slower,

conversion methods [119]. KC's pores are a result of the spaces left between the

interlocking helices of the linear disaccharide, which auto-assembles to this conformation after dissolving in water and subsequently constituting as a gel [120]. STEM-EDX (**Figure 2.9D-G**) confirmed presence of carbon and oxygen due to the GO and KC. Sulfur is present solely due to the sulfate group in KC.
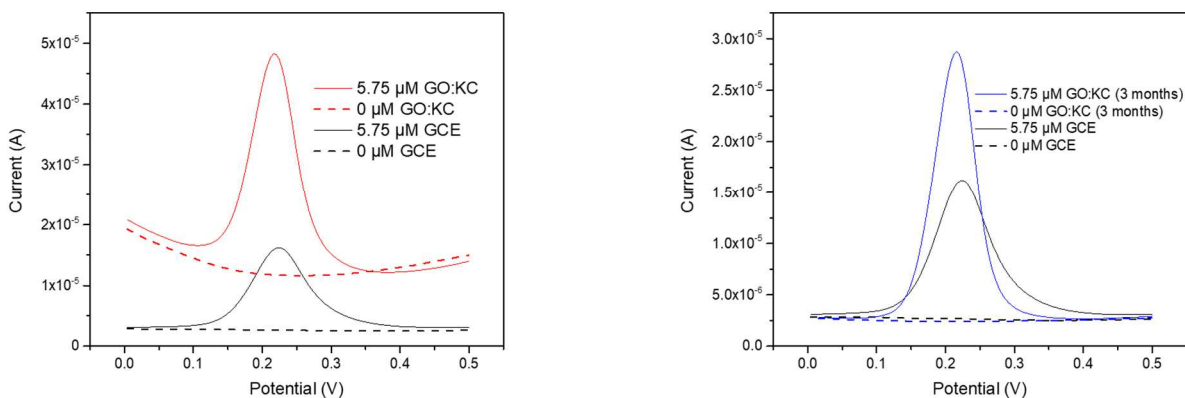
Figure 2. 10. Differential pulse voltammograms comparing performance of 10:1 GO:KC film when it was initially made and 3 months in storage as an aqueous solution vs. a glassy carbon electrode

To best capture the system's performance in pH neutral, room-temperature media, all electrochemical characterization, except for **Figure 2.11B** in $KFe(CN)_6$, was conducted in 0.1 mol L^{-1} PBS solution. Characterization has demonstrated comparable reactions to the control, a bare glassy carbon electrode, albeit at a higher amplitude in respect to current for differential pulse voltammetry, and cyclic voltammetry respectively, according to **Figure 2.10** and **Figure 2.11**. While initially DPV for GO:KC demonstrates a baseline of ~2 µA, storage of the solution lead to a significant drop in conductivity over a course of three months, shown in **Figure 2.10**. The loss of conductivity is likely attributed to the degradation of kappa-carrageenan into a related polymer poligeenan [121]. One study has shown a similar effect in weakly acidic solutions with pristine

kappa-carrageenan hydrolyzing to poligeenan [122]. Despite this loss in conductivity over storage, dopamine oxidation proceeded similarly in both new and 3-month-old solutions of GO:KC. Upon the addition of 5.75 µM DA, an oxidation peak of 0.23 V and 0.22 V for the bare GCE and film-modified electrode were observed, respectively. In this potential range, dopamine is oxidizing to form σ-dopaminequinone, an unstable product that can result in the fouling of the electrode and a loss of conductivity as it forms an insulating film [123, 124].
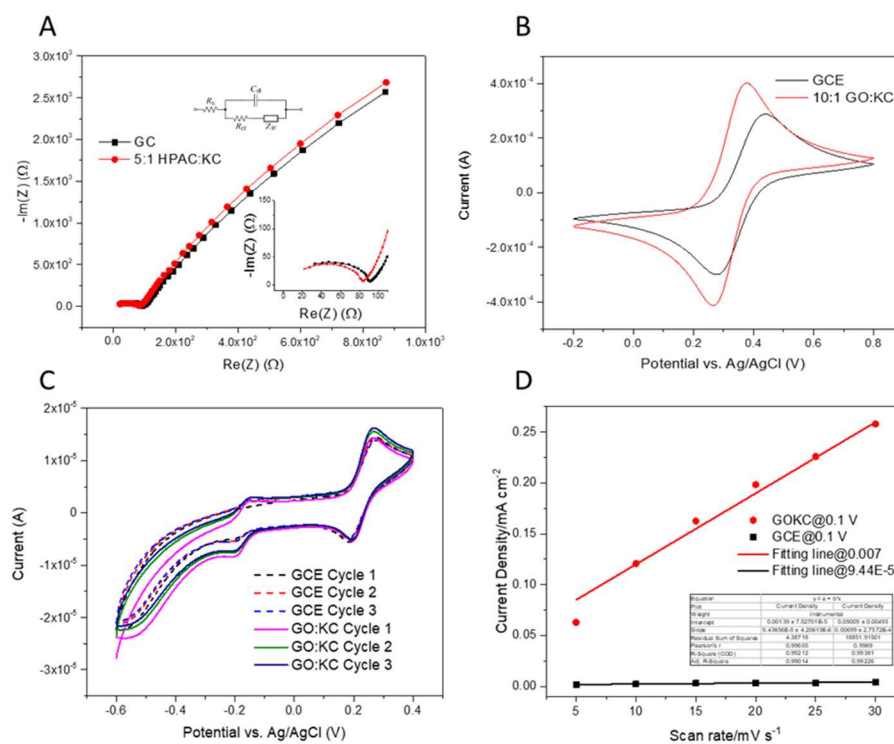
Figure 2. 11. Electrochemical characterization of the 10:1 GO: KC film vs. GCE, A.) EIS of electrode in 0.1 M PBS with Randles equivalent circuit used for fitting B.) Cyclic voltammogram of 10:1 GO: KC vs. GCE in K4Fe(CN)6 C.) Cyclic voltammogram of 10:1 GO: KC vs. GCE D.) Electrochemically active surface area for GO:KC film vs. GCE

This fouling effect was investigated in **Figure 2.11C**, where cyclic voltammetry at 0.05 V/s was carried out for 3 cycles in the presence of 5.75 µM of DA. For the GCE, the system remained relatively static over the course of the 3 cycles while the amplitudes of

the oxidation and reduction peaks in GO:KC appeared to marginally increase. This could

be a slight, but temporary effect of the dopamine oxidation products slightly expanding

the surface area of the porous film. The oxidation reaction responsible for the peak in the

0.2 - 0.3 V range is likely taking part on the GO and glassy carbon working electrode and

is the dominating reaction for both the bare working electrode and this sensor. An

additional redox reaction can be observed in the -0.2V - -0.1V potential window. One

possible explanation could lie in the synthesis of the GO. Because the GO is catalyzed in

a strong base and converted on the surface of nickel foam, there is a possibility of

potential doping of an NiO species during the high temperature plasma conversion. NiO

has been implemented as a DA sensor and shows similar redox behavior in that potential

window [125].

To analyze conductivity, electrochemical impedance spectroscopy was measured (**Figure 2.11A**). Electrochemical impedance spectroscopy demonstrated a lower Warburg

impedance value of 86 Ω than the control glassy carbon electrode's value of 94 Ω. This

indicates that the 10:1 GO: KC improved conductivity of the system. Charge transfer

impedance between the surface of the electrode and the film was found to be 20 Ω for the

10:1 GO: KC film and 35 Ω for the GCE. This reflects similar instance of lower

conductivity in the film. In KFeCN$_6$, cyclic voltammetry was conducted to assess this

change in conductivity. **Figure 2.11B** demonstrates an appreciable increase in the redox

peaks of the voltammogram, supporting the EIS results.

2.3.2. Identifying ideal GO: KC ratio for film
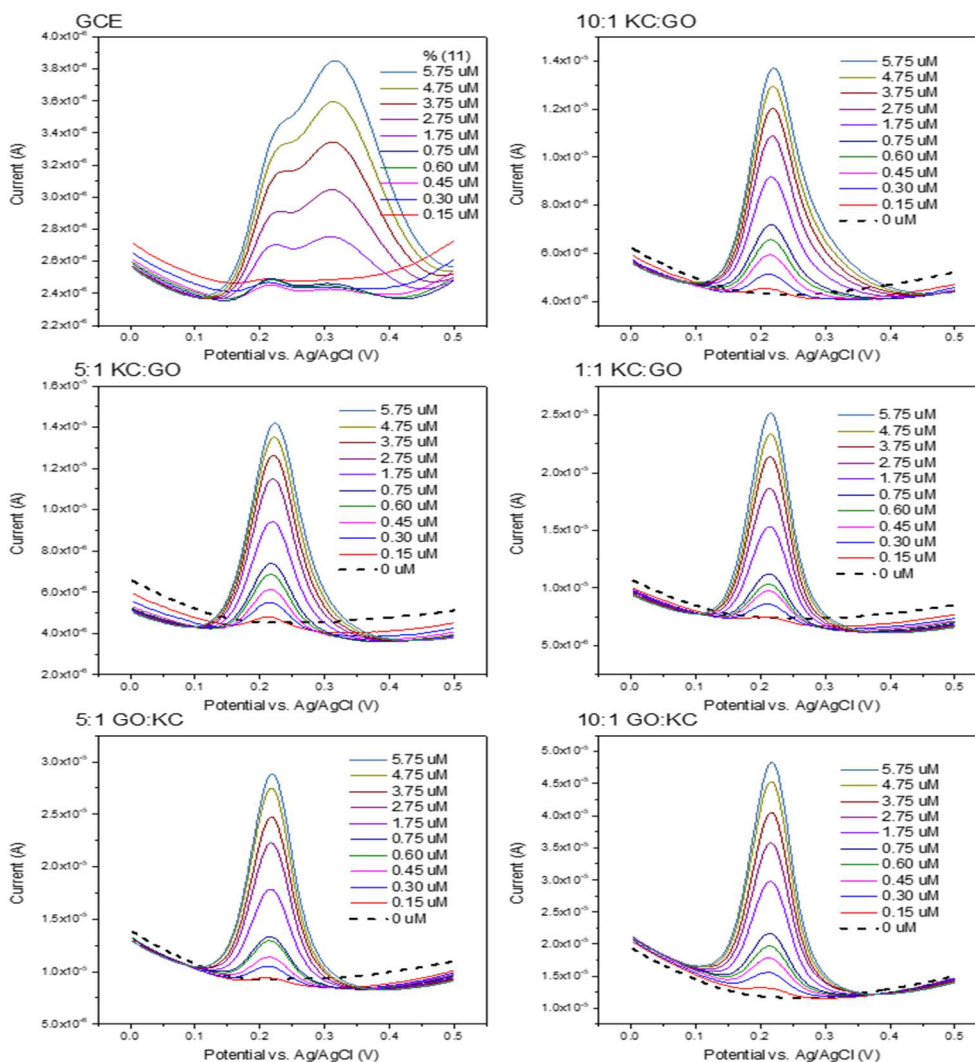
Figure 2. 12. DPV results of DA concentrations ranging from 150 nM – 5.75 uM, scanning rate 0.004

V/s, for bare glassy carbon electrode, 10:1 KC: GO, 5:1 KC: GO, 1:1 GO: KC, 5:1 GO: KC, 10:1 GO:

KC

To determine which ratio of material would be optimal for sensing DA, several

concentrations of GO: KC were tested. It was hypothesized that due to GO's higher

conductivity than KC, the limit of detection would be higher with an increasing

proportion of GO. This hypothesis was confirmed by differential pulse voltammetry in

Figure 2.12. A pure KC film on a working electrode demonstrated slightly higher

sensitivity to dopamine than the bare working electrode, which suggests it has interactions with dopamine. As predicted, having a higher proportion of conductive carbon to carrageenan would both provide a higher amplitude of peak current and more sites for KC helices to adsorb physically. As a result, the limit of detection with a S/N=3 was highest for 10:1 GO: KC at 0.15 μmol L^{-1} and a linear range of 1 μmol L^{-1} – 250 μmol L^{-1}, **Figure 2.13**.
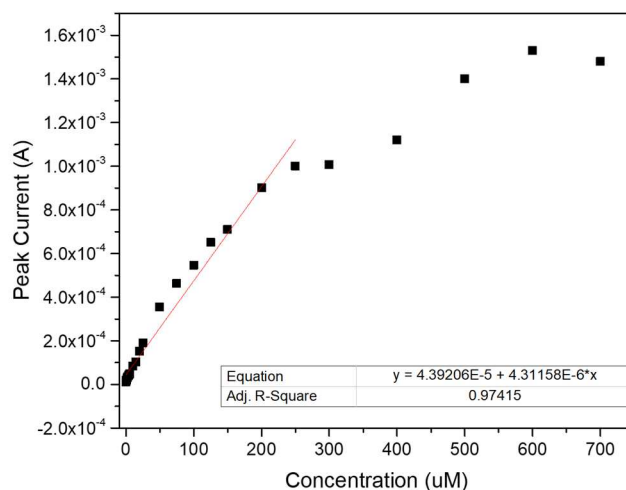
Figure 2. 13. Linear range of sensor based off differential pulse voltammogram peak current

Interestingly, the limit of detection did not scale uniformly with the increasing concentration of GO. Instead, the second highest limit of detection was determined to be 1:1 GO: KC. The lowest limit of detection was encountered with the 10:1 KC: GO film. This would suggest that a type of threshold exists in relying on GO's interactions with DA versus KC's interactions with DA. Three replications in 10:1 GO:KC, shown in **Figure 2.14**, were conducted to demonstrate repeatability. Overall, the modified electrode's standard deviation was relatively low and suggested the system had high repeatability between coatings, **Table 2.1**,
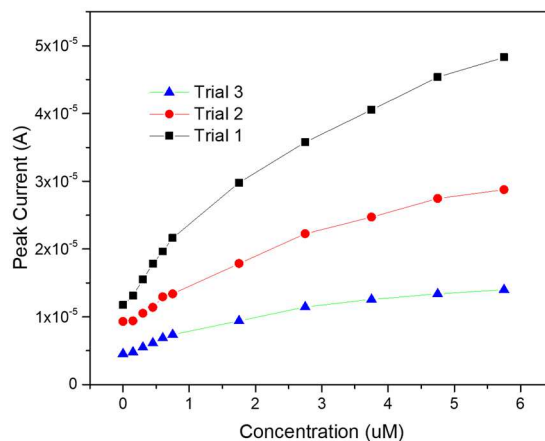
Figure 2. 14. Peak currents from DPV vs concentration of dopamine of three replications of 10:1 GO:KC composite film

Table 2. 1. Statistics for three replications of 10:1 GO:KC composite film

Data	N total	Mean	Standard Deviation	Minimum	Median	Maximum
10:1 GO:KC Replications	3	1.77E-05	1.17E-05	4.55E-06	1.34E-05	4.83E-05

This information could be useful in examining more extreme ratios of the two materials. One potential explanation for this phenomenon could lie in the orientation of the KC helices on the GO's surface. KC's helices best film forming occurs in 1.0-2.5% solutions by mass in 1% acetic acid [126]. In the 10:1-1:1 KC:GO ratios, this interaction between acetic acid and KC may have been disrupted due to the GO's own interactions with KC and acetic acid. By having high amount of KC, GO's interactions with KC dominate, while having lower amounts of KC still retain the film-forming properties of KC while avoiding most of the interactions between GO and KC. As shown in **Figure 2.15**, having a 5:1 ratio of GO:KC resulted in a slightly higher R^2 value than the 10:1 GO: KC film,

despite of its slightly lower sensitivity. Higher concentrations of KC resulted in more

stable, cohesive films that adhered to the surface of the GCE better during testing.
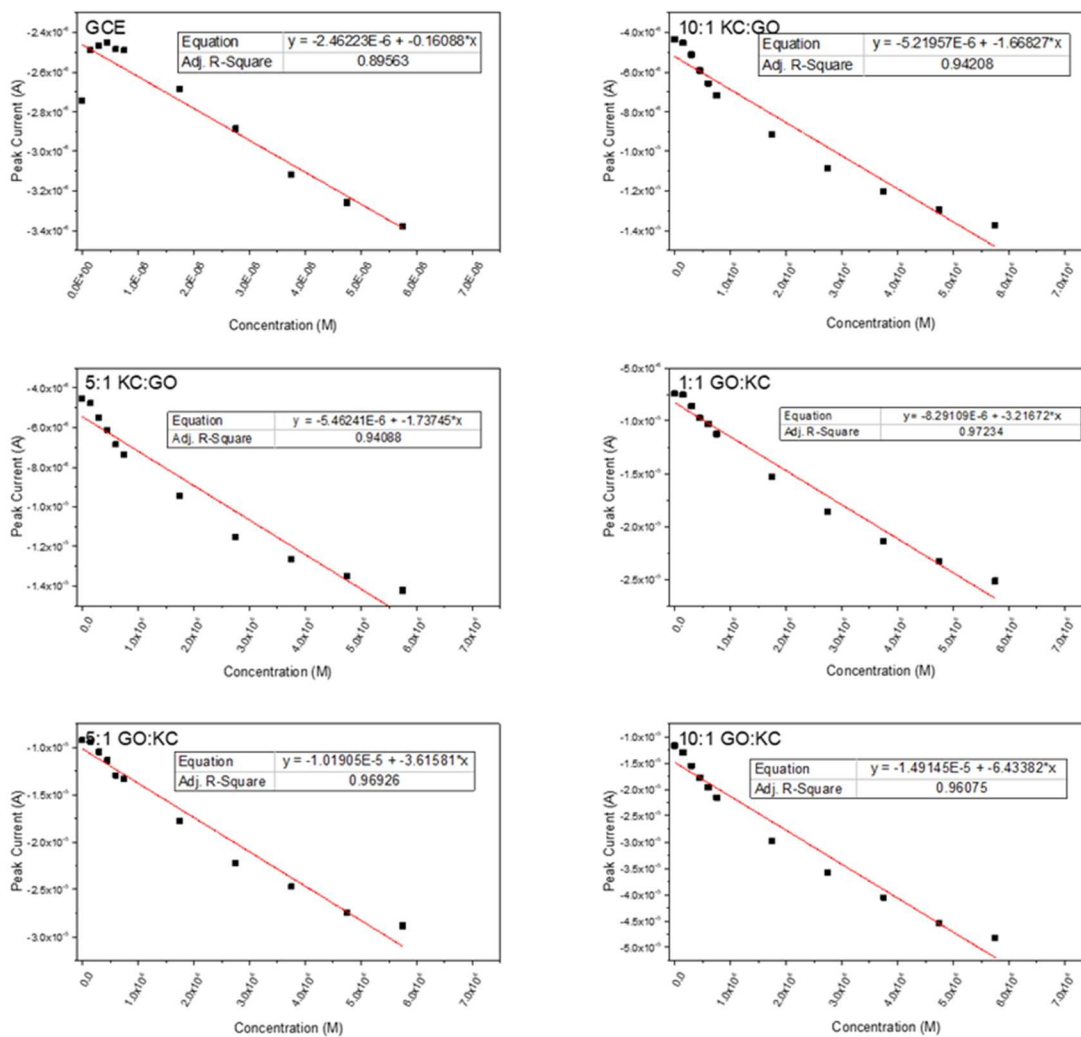
Figure 2. 15. Linear fit of -DPV peak current values of DA concentrations from 150 nM – 5.75 μm. for bare

glassy carbon electrode, 10:1 KC: GO, 5:1 KC: GO, 1:1 GO: KC, 5:1 GO: KC, and 10:1 GO: KC

2.3.3. Comparison to contemporary electrochemical dopamine sensors

As shown in **Table 2.2**, DA sensing with this research's platform is competitive with

contemporary systems of 2019 in terms of linear range and limit of detection. A major

advantage the GO: KC film has over most DA sensors is its simple method of preparation

and low-cost materials. Notably, no adhesive polymer such as PTFE, Nafion, or PVDF

was necessary in adhering the film to the surface of the GCE. Instead, the adhesive

properties of the composite itself were relied upon with a high degree of success.

Table 2. 2. Comparison of this work to 2019 electrochemical sensors of DA, LOD based on S/N=3 for all studies

EC Sensor Composition	Method	Linear Range (μmol L^{-1})	Limit of Detection (μmol L^{-1})	pH	Reference
Onion-like carbon	SWV	12-24	1.24	7.0	**[127]**
Graphite/varnish ink	DPV	30 – 800	0.13	6.1	**[128]**
PANI^a-Au NPs^b/graphite	DPV	1– 100	0.86	7.0	**[81]**
GO: KC	DPV	1 – 250	0.232	7.1	***(this work)***

a.   *PANI: polyaniline*

b.   *Au NPs: gold nanoparticles*
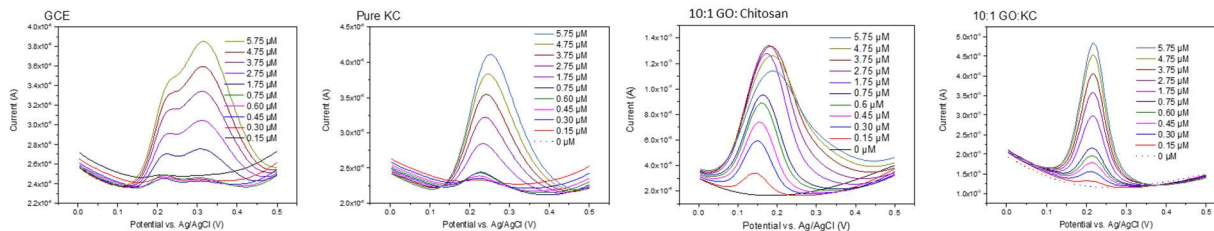
Figure 2. 16. Comparison of glassy carbon electrode, pure kappa carrageenan film, 10:1 GO: Chitosan and

10:1 GO:KC composite film from 0.15 µM - 5.75 µM

To assess KC's role in this system, it was compared to another commonplace

polysaccharide, chitosan. 10:1 GO: Chitosan was synthesized in an identical method to

10:1 GO: KC and is displayed in **Figure 2.16**. While initially competitive with GO:KC at

low concentrations of DA, chitosan is unable to perform as well and is significantly less

conductive, with a baseline of ~4µA compared to GO:KC's ~20µA.

The major benefit of KC in this is system is its conductivity and simplicity. With a 3'

SO4- group, there are significant opportunities for manipulation and functionalization

[129]. One such study implemented a heavy metal ion sensing system with KC by

forming a composite with the thiolated amino acid cysteine [130]. KC's high surface area

and labile properties were responsible for its high selectivity and sensitivity. In the future,

other carrageenans could be investigated to assess the effects of location and number of

the SO4- groups and whether they increase conductivity and stability of the

electrochemical sensing platform.

2.4. Conclusions

Having a higher ratio of GO: KC resulted in a higher limit of detection than other samples due to higher conductivity and subsequent amplification of the signal. Compared to other electrochemical DA sensors, this system demonstrates a high degree of sensitivity and ease-of-use. Improvements in selectivity and sensitivity as well as targeting different molecules could easily be in reach via functionalization of the kappa-carrageenan and/or activated carbon. This research substantially extends the scope of materials that can successfully be applied to electrochemical DA sensing work. This system has much potential for future modification and implementation. Due to KC's highly reliable gel forming properties at neutral pH and GO's conductive, highly porous structure, this composite offers many avenues for future research. Carrageenan's non-starch, helical composition lends to a bio-inspired formation suitable to the detection of more than just DA. Heavy-metal ion sensing has already been investigated with KC utilizing a complex with l-cysteine to prevent sheet stacking on the electrode surface.

2.5. Acknowledgements

undergraduate researchers Amber Schuster and Emily Leupp for their critical input in preliminary design of the sensor.

2.6. Conflict of interests

There are no conflicts of interest to disclose in this work.

CHAPTER 3

One-step electrodeposition of nickel sulfide for electrochemical detection of nitrite

Authors: Matthew Hummel, Shun Lu, Hongxing Jia, Wei He, Yue Zhou, Zhengrong Gu*

*Corresponding author.

Email address: Zhengrong.Gu@sdstate.edu

Abstract:

Nitrite is a natural byproduct of the Nitrogen Cycle and a food preservative that poses significant risks to human and animal health when encountered in large concentrations via food and water sources. To prevent significant exposure to the molecule, an effective electrochemical sensing platform was developed by a one-step electrodeposition of nickel sulfide on the surface of a glassy carbon electrode. The facile method produced a thin layer on the surface of the glassy carbon that was characterized with x-ray diffraction and scanning electron microscopy. The electrochemical performance of the system was linearly responsive to nitrite concentrations from of $0.04 - 1$ μM, $1 - 5.3$ μM and a detection limit of 0.01 μM and presented a promising new strategy to rapidly detect the molecule. Because the electrodeposition method was so simple, it offers the unique advantage of being transposable to multiple electrode types such as nickel foam and carbon fiber in the future.

Keywords: nickel sulfide, electrodeposition, sensor, nitrite, simple synthesis

3.1. Introduction

Nitrite (NO_2^-) is a naturally occurring oxyanion and an integral part of the nitrogen cycle that has many applications in food preservation, antibiotics, anti-corrosives, and fertilizers [47, 72]. Despite its value, nitrite is toxic due to its negative impact on the oxygen carrying capacity in the blood and its carcinogenic and cardiovascular effects upon long-term, regular exposure [131, 132]. Due to these potential health and safety hazards, the demand for highly accurate nitrite detection in drinking water, food products, and animal feed is great. To meet this demand, many strategies have been developed for detecting nitrite including spectrophotometry, chromatography, and electrochemical methods [133-136].

Electrochemical methods for detecting nitrite have the appealing advantage of being robust systems that are easy to use [137]. The primary non-enzymatic mechanism by which they detect nitrite involves the electrooxidation of nitrite to nitrate at a specific potential on the carbon or platinum working electrode in a three-electrode conformation [138]. In addition to this simplistic method of detection, electrochemical detection also relies on cheap, abundant materials and instrumentation in comparison to other nitrite detection systems [139]. While this process affords a rapid method to accurately quantify nitrite, it suffers from slow reaction kinetics on the traditional carbon-based working electrodes and requires modification to become competitive with other methods [140]. These modifications have included carbon nanotubes, transition and noble metal nanoparticles, metal organic frameworks, and graphene coatings among others [141-145].

One promising option for modification of electrodes for electrochemical detection of nitrite is by mimicking chemical features in the redox centers of the enzymes responsible for their oxidation. Transition metal sulfides are present in the catalytic region of nitrite oxidoreductases containing molybdenum conjugated to sulfides and cysteine residues in the nitrifying bacteria *Nitrobacter [73]*. Nitrite oxidoreductases are the only known method employed by organisms to oxidize nitrite to nitrate and are key to the nitrification process in soils and water [146, 147]. Utilizing transition metal sulfides has already proven advantageous in other electrochemical applications such as energy storage and catalysis [148, 149]. Nickel sulfide is one transition metal sulfide that is particularly effective for nitrite oxidation. This is due to nickel's already excellent catalytic activity and nickel sulfide's ability to hydrogenate nitrogenous compounds [150]. Specifically as a nitrite oxidation catalyst, nickel sulfide has been employed successfully on carbon nanotubes for the detection of nitrite with a linear range of 1 μM to 4.2 mM [151]. Nickel sulfide is also environmentally innocuous and present throughout nature in mineral forms such as heazlewoodite and, furthermore, is simple to synthesize [152].

Electrodeposition is one such way to synthesize transition metal compounds with unique structural properties such as nickel sulfide [153]. Utilizing electrodeposition, several studies have demonstrated the assembly of nanocrystalline layers with tunable properties based on the deposition potential waveform [154, 155]. The process also benefits from utilizing safer, more convenient buffers than traditional non-electrochemical methods which streamlines the process for future commercial implementation [156]. The deposition of transition metal oxides and sulfides is a growing option for increasing

conductivity and has seen increased attention in energy storage because of the variable oxidation state driving rapid redox reactions [157].

In this work, a nickel sulfide coating was synthesized via a one-step electrodeposition method. Next, the electrodeposited sample on a glassy carbon electrode (NiS@GCE) worked as the binder-free electrode for nitrite detection. Benefiting from the excellent conductivity of the GCE and more exposed active sites, the as-prepared electrode shown good electrochemical behavior to nitrite in buffer. Additionally, the in-situ electrodeposition method also provides a simple way to develop an electrochemical sensing platform with standard, readily available materials that require minimal modification.

3.2. Experimental

3.2.1. Chemicals and reagents

Nickel(II) nitrate hexahydrate, thiourea, sodium nitrite, and PBS buffer solution were purchased from Fisher Scientific (USA) and used without further purification or alteration.

3.2.2. Materials preparation

Formation of NiS on the glassy carbon electrode (GCE) was achieved via electrodeposition by cyclic voltammetry in a nickel(II) nitrate (10 mM) and thiourea (10 mM) solution in water (7 pH). Parameters for the cyclic voltammetry deposition were a scan rate of 20 mV s^{-1} from -1.2 V – -0.1 V for 50 cycles with an Ag/AgCl reference electrode and a platinum wire counter electrode.

3.2.3. Physical characterization

Structure of the electrodeposited NiS was evaluated using X-ray diffraction

measurements performed on a D/Max-III (XRD, Rigaku Co. Ltd., Japan) using Cu Kα

radiation λ = 0.15406 nm at a scanning rate of 5°/min and operated at 34 kV and 26 mA.

Scanning electron microscopy (SEM, Hitachi S4800, Japan) was carried out to visualize

structural features of the electrodeposited NiS versus bare carbon aerogel paper, which

served as a proxy for the similar GCE. Transmission electron microscopy (TEM) was

conducted on a JEOL JEM-2100 electron microscope operating at an accelerating voltage

of 200 kV. STEM-Energy Dispersive X-ray Spectroscopy (EDS) (Oxford) was used for

elemental confirmation.

3.2.4. Electrochemical measurements

All electrochemical measurements were carried out using an electrochemical workstation

(CHI 760E, CH instruments. Inc., USA) with a typical three-electrode system consisting

of the working electrode (WE), counter electrode (CE) and reference electrode (RE).

Herein, the glassy carbon electrode (GCE, $1*2$ cm^2) was used as the WE, the Pt wire and

the saturated Ag/AgCl electrode as the CE and RE, respectively. The electrocatalytic

performance of NiS@GCE was investigated by cyclic voltammetry (CV) and I-t in 0.1 M

PBS buffer solution (pH 7). The electrochemical impedance (EIS) measurements were

performed inside the three-electrode electrochemical cell. EIS study was performed within

frequency range of 100 kHz to 0.1 Hz with an AC amplitude of 10 mV. An equivalent

Randles circuit model with Warburg impedance was used to fit the data to calculate the

charge transfer resistance R_{ct} for each catalyst system. All potentials were referenced to the

Ag/AgCl electrode if not specified. All the tests were carried out at room temperature (~25 °C).

3.3. Results and discussion

3.3.1. Physical characterization of the NiS-modified Glassy Carbon Electrode

Electrodeposition of NiS layers was achieved with cyclic voltammetry from -1.3 V – -0.1 V for 50 cycles (**Fig. 3.1**). In response to the potential applied by cyclic voltammetry in a basic buffer, the reaction between Ni^{2+} ions from nickel nitrate with the negative sulfur ion liberated from the sulfide group in thiourea occurred, depositing NiS on the surface of the GCE. This resulted in an increasing oxidation potential at -0.1 V while scanning from the negative to positive voltage at a scan rate of 50 mV/s. **Figure 3.1** demonstrates the increasing anodic wave signifying an increased oxidation potential at -0.1 V as well as an increasing reduction potential at -1.3 V while scanning from positive to negative potential.
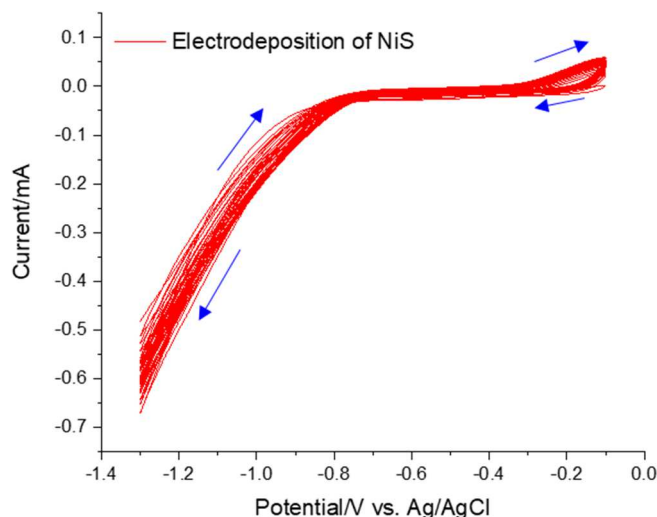
Figure 3. 1. Electrodeposition of NiS on the glassy carbon electrode using cyclic voltammetry, scan rate 20 mV s-1 for 10 cycles.

To characterize changes in the surface of the electrode pre- and post-deposition, carbon

aerogel paper was used as a proxy for the GCE due to their similarity in composition and

conductivity. Scanning electron microscopy was performed to visually characterize the

surface of the bare carbon electrode and demonstrates the bare carbon in **Figure 3.2A**.

Post deposition, a thin layer of NiS can be observed as a fine residue on the carbon

surface. Powder x-ray diffraction confirmed the addition of NiS in **Figure 3.2D** with

small signature peaks of NiS indicating that NiS is present but may not be fully

crystalline, as the peaks are broad and do not distinguish easily from the background of

the carbon [158]. This suggests that unlike the previous study in nickel sulfide formation

using high temperature (400-600°C), the electrochemical method of synthesis with

thiourea and nickel nitrate presented in this paper omits the use of a time-consuming

calcination step at the cost of a high degree of NiS crystallinity, which agrees with

another study synthesizing non-crystallized NiS [159]
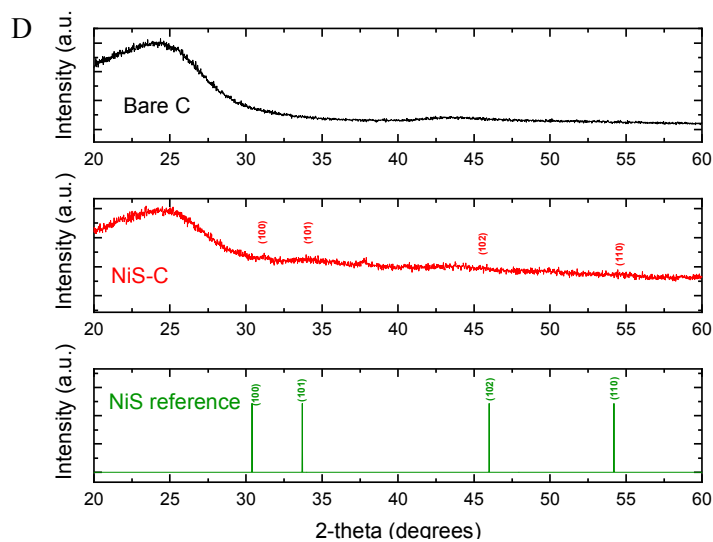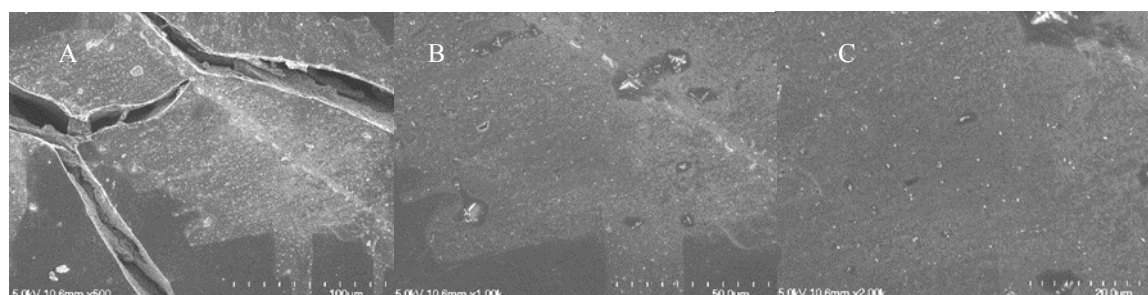
Figure 3. 2. Scanning electron micrographs of NiS electrodeposited on carbon as a powdery white layer with small individual crystals (A-C) at x500, x1000, and x2000 magnification and (D) powder x-ray diffractogram of bare carbon versus NiS on carbon (ICDD # 03-064-

To further examine the physicochemical properties of the material, transmission electron microscopy with energy dispersive x-ray spectroscopy was performed and are shown in **Figure 3.3.** EDX mapping and peak analysis indicated homogenous dispersion of Ni and S on the material's surface, confirming its composition as NiS. STEM (top left) displays the semi-crystalline particles and is consistent with their appearance in other works [160, 161]. These particles also appear similar in shape and appearance to the small residues found in **Figure 3.2** on the surface of the carbon post-deposition. Overall, NiS electrodeposition onto carbon appears to successfully proceed in standard buffers but suffers from non-crystallinity because it lacks the conditions demonstrated by other works using high temperatures and dry conditions to facilitate the growth of well-defined crystals.
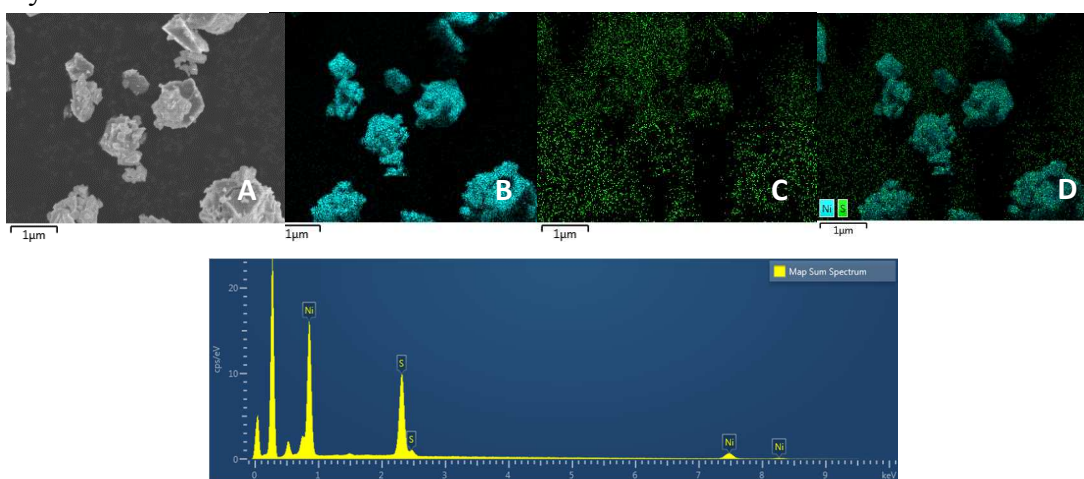
Figure 3. 3. STEM image of NiS (A) EDX data of NiS with Nickel in cyan (B), Sulfur in green (C), overlay of EDX surface maps (D) and peaks (E).

3.3.2. Electrochemical behavior of NiS@GC electrode

Once deposition of an NiS layer was confirmed and NiS was evaluated with XRD and

EDS, the prepared electrode was used in a 0.1 M PBS buffer solution (7.0 pH) to

determine if a 0.1 M concentration of nitrite could elicit a distinguishable response using

cyclic voltammetry (**Figure 3.4**). As **Fig. 3.4 left** shows, the potential of the rising anodic

(oxidizing) current changes from 1.15 V to 0.95 V while oxidation potential at 1.2 V

doubles from 1.0×10^{-5} A to 2.0×10^{-5} A. This response is in agreement with our previous

nitrite detection on NiP and shows a similar increase in anodic current response as a

result of the charge transfer from nitrite to the NiS layer coating the electrode [136].

Electrochemical impedance spectroscopy (EIS) confirmed a lower charge-transfer

resistance (R_{ct}) for the NiS modified electrode through the calculation of the semi-circle

diameter of the Nyquist plot (**Figure 3.5, right**) . The bare GCE demonstrated an R_{ct}

value of 970 Ω while the NiS modified electrode's R_{ct} was significantly lower at 761 Ω.

A lower R_{ct} value can be as a lower energy threshold required for the desired reaction to

take place [162].   This notable decrease of charge transfer resistance confirms presence

of NiS on the surface of the electrode and shows that reaction kinetics for NiS should be

greatly improved versus a bare glassy carbon electrode due to its increase in conductivity.
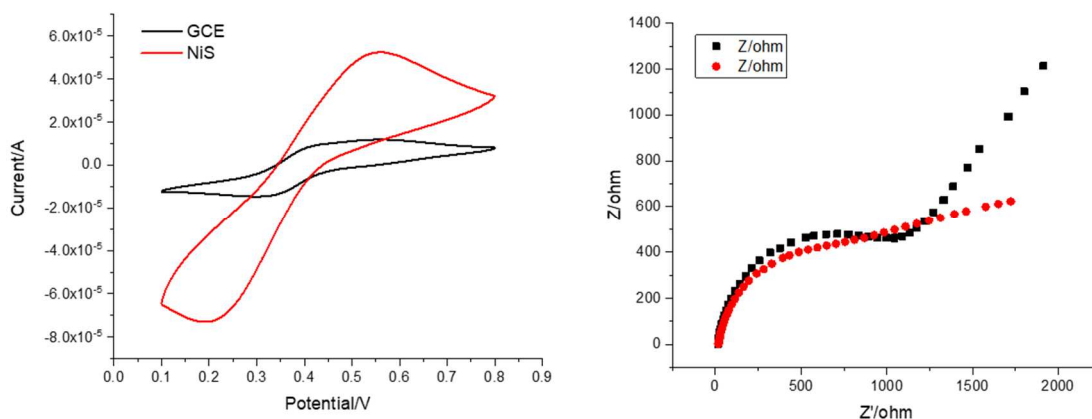
Figure 3. 4. Comparison of the bare GCE (black) to the NiS@GCE (red) using cyclic voltammetry, scan rate 50 mV s-1 (left) and electrochemical impedance spectroscopy, frequency=100 kHz to 0.1 Hz, AC perturbation of 10 mV (right) in 55.0 mM K3Fe(CN)6/0.1 M KCl solution

3.3.3. Electrochemical performance for nitrite sensing

To verify if NiS is a suitable material as a catalyst for electrooxidation of nitrite, a bare GCE and the electrodeposited NiS@GCE were used for the detection of 0.1 M nitrite in PBS solution. **Figure 3.5.** demonstrates both a greater capacitance due to the larger overall area of the voltammograms as well as an increased sensitivity to nitrite with smaller overpotential (~0.95 V for GCE vs. 0.9 V for NiS). This lower energy requirement agrees with electrochemical characterization performed in this study and demonstrates that the more conductive NiS displays superior catalytic activity to glassy carbon. **Figure 3.6.** shows how the NiS@GCE electrode displays a symmetric voltammogram with greater peak current values at 0.6 V. This higher value and greater overall area of the voltammogram with increasing scan rate indicates that the double-layer capacitance is higher for the NiS@GCE electrode than for the bare GCE, meaning that conductivity and surface area are correlatively high [163, 164].
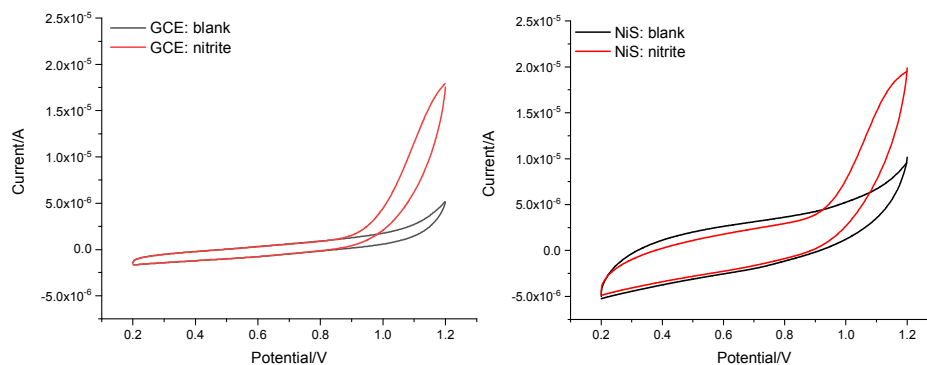
Figure 3. 5. Cyclic voltammograms of a bare GCE in PBS in absence and presence of 0.1 mM nitrite and NiS@GCE in presence and absence of 0.1 mM nitrite
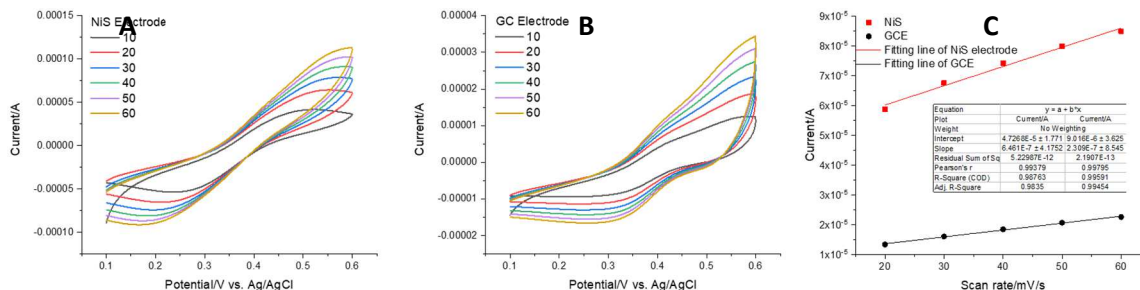
Figure 3. 6. Cyclic voltammetry at 10 mV sec-1 – 60 mV sec-1 scan rates to assess double-layer capacitance of the NIS@GCE (A) and the bare GCE (B) in K3Fe(CN)6/0.1 M KCl solution. Slope of the charging current at 0.6 V versus scan rate (C) gives double-layer capacitance

3.3.4. Electrocatalytic mechanism of nitrite oxidation

To characterize the mechanism by which the NiS oxidized nitrite to nitrate and what may influence that mechanism's efficiency, cyclic voltammetry was performed in 0.1 M PBS (7.4 pH) to assess the effect of scan rate on anodic current response of nitrate oxidation. **Figure 3.7.** demonstrates a linear correlation with the oxidation peak and the square root of scan rate as shown by the fitting equation i_p (A) $= 2.78 \times 10^{-4} + 1.66 \times 10^{-5} v^{1/2}$ ($R^2 = 0.9961$). This emphasized that the mechanism is dependent on diffusion of nitrite across the surface of the NiS electrode according to the Randles-Sevcik equation. This type of diffusion is common across the surface of electrodes and results in a linear relationship between scan rate and the square root of time [165].
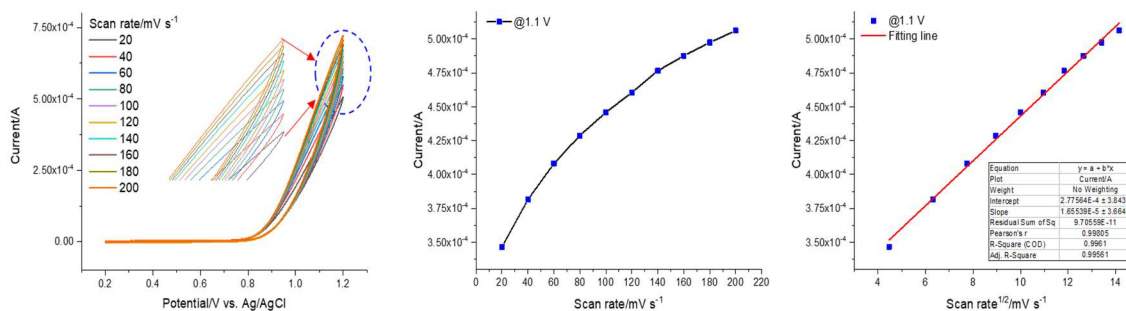
Figure 3. 7. (a) cyclic voltammograms showing the effect of scan rate on anodic current response of nitrite oxidation at 1.2 V. (b) oxidation peak current values at 1.1 V versus their respective scan rates (c) peak current values versus the square root of the scan

3.3.5. Amperometric response to nitrite

Gauging the amperometric response of the NiS@GCE electrode versus time helps support the diffusion-based mechanism **Figure 3.8** demonstrated as well as indicate the presence of any unexpected interactions at the surface of the electrode over a period during a held voltage while exposed to the analyte. In **Figure 3.8,** 0.1 mM nitrite was added to 0.1 M PBS (7.4 pH) to evaluate the relationship with the square root of time. As in Figure 3.8, the amperometric response versus the square root of time was linear and demonstrates the typical diffusion-controlled process for the detection of nitrite ions across the NiS@GCE surface [112].
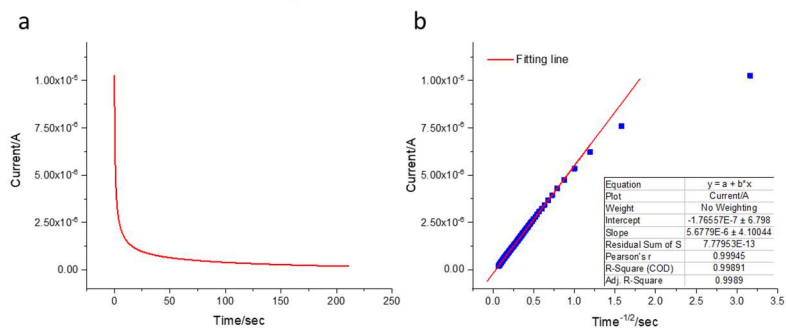
Figure 3. 8. (a) amperometric response of NiS@GCE to 0.1 mM nitrite in 0.1 M PBS (pH 7.0) at potential of -1.2 V. (b) plot of I vs. t-1/2 derived from amperometric I-t curve (blue) with linear fitting (red)

Assessing NiS@GCE's ability to detect different concentrations of nitrite was carried out

with an *i-t* test with a 1.1V held potential to quantify amperometric response and

establish a calibration curve. **Figure 3.10** demonstrates the staircase-shaped response to

nitrite in 0.1 M PBS with increasing nitrite concentrations of 0.01 μM x 10, 0.02 μM x

10, 0.100 μM, 0.200 μM x 10, and 0.4 μM x 10 respectively in **Figure 3.10A**. Current

stability was good for concentrations of 0.01 μM – 8000 μM as shown by the flat, stable

current response of each dose. Linearity was found for two distinct ranges of data with

0.01 – 1 μM (R^2=0.9536) and 1 – 5.3 μM (R^2=0.9934). Good linearity for both ranges

separately suggests a slight change in reaction kinetics as more nitrite oxidizes on the

surface of the NiS-modified GCE. This could be associated with fouling of the electrode

resulting in a drop of conductivity in the system[166]. Using the slope of the calibration

curve, 5.0797 x 10^{-5} A/μM was determined as the sensitivity of the system. At the lower

linear range of the system, 6.5047 x 10^{-5} A/ μM was demonstrated, indicating a drop in

sensitivity after ~1 μM concentrations. Potentially, nitrite could be fouling the surface of

the electrode and contributing to this drop in sensitivity. Overall, these results are in

agreement with our previous study of NiP@nickel foam [136]. The limit of detection was

determined to be 0.01 μM (s/n=3) and a limit of quantification of 0.05 μM.

For further improvement of the system, implementing more conductive materials such as

graphene or carbon nanotubes to form a composite during the deposition step could allow

for better overall sensing performance while maintaining the simplicity of the system.

This would proceed by allowing the NiS to grow on a higher surface area material with

higher conductivity than the bare glassy carbon electrode. As more nanotube/NiS would

deposit, more surface features would form providing area for seeding of NiS crystal and better development of the catalytic component of the system as found in our previous work implementing carbon nanotubes with cobalt phthalocyanine. In our previous work, this exhibited higher overall sensitivity than the current system and represents a realistic path forward for further increasing the utility of this novel platform [112]. Incorporating bimetallic complexes has also demonstrated improved electrochemical behavior in other transition metal sulfide-focused studies and has potential to improve nitrite detection via the same mechanisms [167, 168]
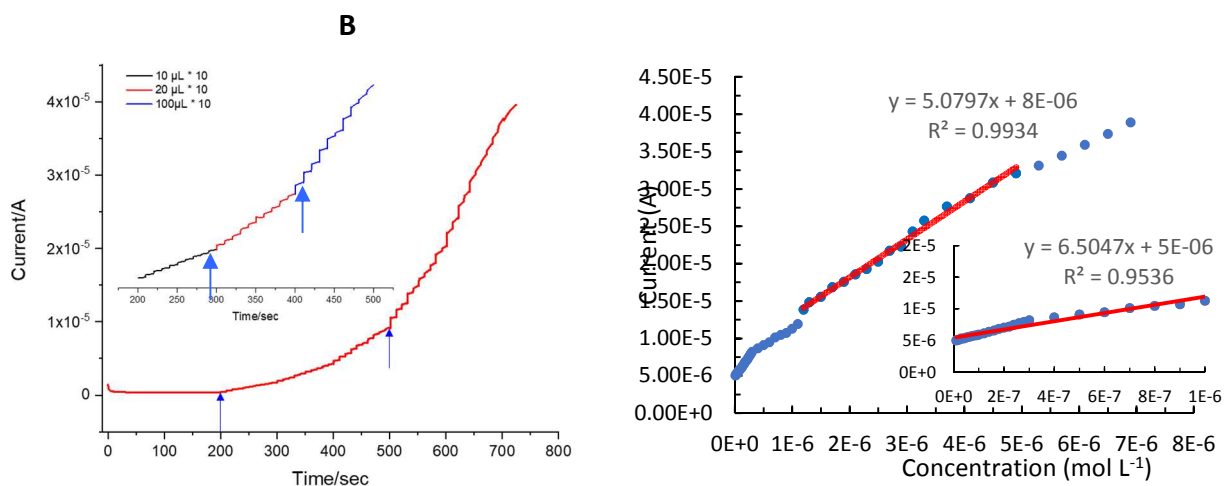
Figure 3. 9. (A) I-t response at 1.1V of NiS@GCE to 10 doses of 10 ɥL (black), 20 ɥL (red), and 100 ɥL (blue) of 0.01 mmol L-1 nitrite solution added to 10mL of 0.1 M PBS (pH 7) buffer solution in upper graph inlay giving a nitrite sensing range of 0.01 μM – 1 μM

3.3.6. Comparison to Other Electrochemical Nitrite Sensors

Compared to other nitrite sensing platforms, as shown in **Table 3.1.**, this platform

performed well in the low concentration range, which is critical for detecting the trace

amounts of nitrite that are generally responsible for continuous dosing in media such as

baby formula and other similar food products. In higher concentration ranges, this

platform was less stable and exhibited some effects that can typically be associated with

fouling of the electrode and subsequent losses in conductivity. Because of this, it is

noteworthy to assess for the effects of other

Table 3. 1. Comparison of nitrite detection performance of this paper to contemporary electrochemical nitrite sensors

Electrode Material	Electrochemical Method	Linear range ($\mu mol\ L^{-1}$)	LOD ($\mu mol\ L^{-1}$)	Ref.
Au Pd/rGO*	Amperometric	0.05 – 1000	0.02	[169]
Ag Nanoplatelets	Amperometric	10 - 1000	1.2	[170]
B-MnO$_2$** nanorods	Amperometric	0.29 – 26090	0.29	[171]
NiS	Amperometric	0.04 – 5.3	0.01	[*this work*]

*Gold-palladium on reduced graphene oxide
**beta-manganese dioxide nanorods

3.4. Conclusions

To conclude, a simplistic method to electrodeposit an NiS catalyst on a glassy carbon

electrode was accomplished with cyclic voltammetry. The modified electrode displayed a

robust electrochemical response to nitrite using the i-T method with a linear range of 0.04

– 1 µM, 1 – 5.3 µM and a detection limit of 0.01 µM. The facile synthesis of the NiS

layer on the electrode affords this method great versatility to a variety of working

electrodes in a three-electrode system and presents a novel method to detect nitrite with

excellent stability and sensitivity. Improvements to the NiS@GCE could include the incorporation of conductive carbon materials such as graphene or carbon nanotubes to both increase surface area and conductivity as well as provide a space for seeding more NiS crystals versus the bare GCE.

3.5. Acknowledgements

3.6. Conflicts of Interests

There are no conflicts of interest to disclose in this work.

CHAPTER 4

Alkali Earth Metallophthalocyanine and Metalloporphyrins for the Electrochemical

Detection and Quantification of Bacterial Trehalose

Matthew Hummel*, Hongxing Jia*, Ailin Guo, Abdullah Maruf, Shun Lu, Wei He, Yue

Zhou, Zhengrong Gu**

Co-first authors

**Corresponding author, zhengrong.gu@sdstate.edu*

Abstract:

Trehalose is a naturally occurring disaccharide synthesized by a large variety of microbes including deadly pathogenic *Salmonella* and *E. coli*. Despite its omnipresence, detection of trehalose is difficult and requires advanced chromatographic methods like HPLC-RID or LC-MS/MS. In this work, trehalose was rapidly quantified on a screen-printed electrode modified with three molecules: magnesium phthalocyanine, magnesium *meso*-tetraphenyl porphyrin, and calcium *meso*-tetraphenyl porphyrin. Detection of trehalose consists of two steps: electrodeposition for 30 seconds at -1.2 V followed by electrooxidation via squarewave anodic stripping voltammetry. All samples were quantified in lysogeny broth at concentrations of 0.25 mM – 100 mM for *n=4* trials with minimal processing. Of the three molecules, magnesium phthalocyanine displayed the greatest mean sensitivity at 1.89 x 10^{-5} A/mol but exhibited high standard deviation between trials. Magnesium *meso*-tetraphenyl porphyrin demonstrated a lower sensitivity but also the lowest standard deviation and highest linearity. Trehalose in broth data for the three molecules was then used as a standard calibration curve for detection of lysed *E. coli* trehalose grown in the same broth medium for 0h, 12h, 24h and 48h incubation in 4°C and 37°C, respectively. Whole sample concentrations peaked in both 4°C and 37°C at 48h corresponding with the higher number of total colony forming units. Concentration per colony forming unit peaked at 12 h for 4°C while they linearly decreased for 37°C. Overall, the system demonstrated highly repeatable, rapid quantification of trehalose in a complex media and is a promising alternative to more intensive methods.

4.1. Introduction

The need for rapid microbe-targeted biosensors is critical to preventing outbreaks in communities by monitoring the products they consume as well as ensuring quality in microbial processes like fermentation. Advancing such technology has been key to containing health hazards through rapid, robust systems that exist on-site in hospitals, meatpacking plants, and other facilities with a high potential of spread [172]. Electrochemical biosensors are a promising avenue of research for developing simple, fast detecting units which enables operation by minimally trained personnel or patients themselves [173-175]. Expanding electrochemical biosensing targets to molecules integral to many microbes' survival would greatly advance our capabilities for monitoring infection, survival, and growth stages. Therefore, rapidly detecting the polysaccharide trehalose could allow real-time monitoring of a large host of microbes responsible for these processes [176-178].
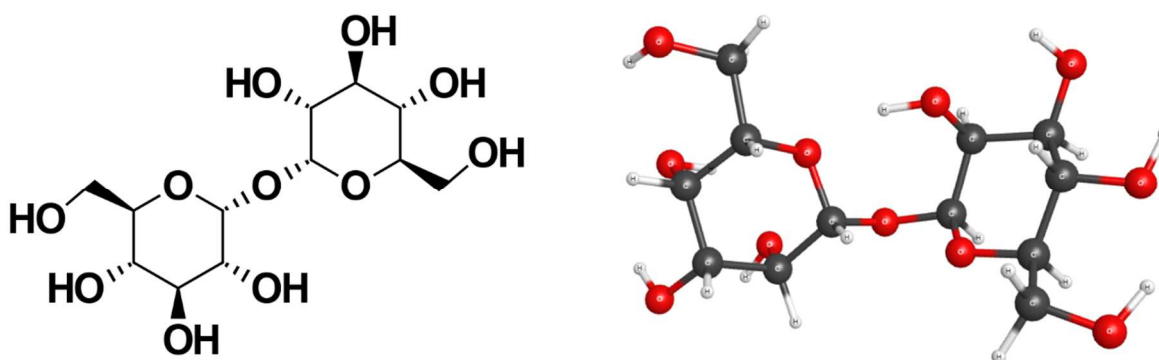
Figure 4. 1. 2D trehalose structure (left) and 3D Gaussian optimized structure (right) exhibiting α-1,1 bond between two D-glucose units

Trehalose is a non-reducing sugar naturally synthesized in organisms ranging from bacteria to the plant kingdom but is notably absent in vertebrates and most plants [179]. This molecule (**Fig 4.1**) consists of two α-glucose units bound by a 1,1 glycosidic bond, resulting in a disaccharide very resistant to acid hydrolysis with antioxidant and anti-desiccant properties [180]. Several studies have concluded trehalose plays a large supporting role in pathogenicity and survival of *E. coli*, *Salmonella spp.*, and *Mycobacterium* among other bacteria and fungi and may present an opportunity for detection of these organisms as a quantitative biomarker [181-183]. One such study concluded detection of trehalose and its enzyme trehalase's activity in patient sputum could accurately detect active *Mycobacterium spp.* infections such as tuberculosis [184].

In commercial meat and produce, trehalose is not inherently present in high concentrations of un-aged meat, fresh fruit, and vegetables except in cases of moderate to advanced contamination by *E. coli*, *Salmonella,* fungi, and other microbes [185, 186]. However, trehalose has gained widespread use as an additive to meat and processed products for its protective role from freezing and desiccation. This comes with the possible consequence of providing a rich support for bacterial growth for newly established pathogens on the products that were still within acceptable numbers during inspection [187]. Due to its growing potential use in the food industry and its role as a signature molecule in both fungi and bacteria, detecting trehalose has great potential for monitoring food quality but is generally hindered by costly, time-consuming methods.

Current methods of detecting trehalose are highly sensitive but generally limited to lab

settings. Until recently, high-performance liquid chromatography with a refractive index

detector (HPLC-RID) was the only truly quantitative method for detection of trehalose

[188]. In a study comparing contemporary trehalose detection options available, LC-

MS/MS, HPLC-RID, and a trehalase enzyme kit from only one commercial source were

identified. These methods were all able to surpass a detection limit of millimolar levels of

trehalose isolated from bacterial lysate but suffer from timely preparation and the need

for costly equipment that would be unrealistic in most commercial food processing

settings that require high throughput [189]. While highly sensitive systems as described

in Hayner et al. 2017 are valuable, the working concentrations of trehalose in

contaminated samples would likely not require such sensitivity for detection of bacterial.

Bacterial trehalose concentrations in *E. coli* cultures have been evaluated and conclude an

intracellular production rate of 20-200 mM of trehalose depending on environmental

stressors [190, 191].

There are multiple natural phenomena that act as potential inspiration for the detection of

trehalose. The catalytic centers of the trehalose-6-phosphate synthase (TPS) enzyme and

the de-phosphorylating enzyme trehalose-6-phosphate phosphatase (TPP) present a

unique opportunity for immobilizing trehalose to the surface of the working electrode.

The immobilization of trehalose-6-phosphate which is driven by a Mg^{+2} ion in TPP is

theorized to act primarily on the phosphate group but also shows interactions with

hydroxyl groups present on the glucose subunits [192]. This behavior was better

characterized with trehalose and some structural analogs such as maltose and acarbose

[193]. The importance of the Mg^{+2} ion in TPS and TPP has been confirmed by multiple sources through selectively removing the magnesium ion via EDTA, resulting in strongly reduced catalytic activity of the enzymes [192, 194]. Trehalose interactions with alkali earth metal ions are not limited to enzymes and are documented in alkali earth metal halide salts as well. These studies modeled an interaction of the Mg^{+2} and Ca^{+2} ions in $MgCl_2$ and $CaCl_2$ could preferentially form metal complexes via alkali earth metal ion interactions with O-4 and O'-4 for Mg^{+2} and O-3, O'-2 groups for Ca^{+2} on trehalose [75]. The calcium-trehalose O-3, O'-2 chelation was further supported via crystallography in a follow-up study [195].

In this study, we assessed the ability of alkali earth metal ions Mg^{+2} and Ca^{+2} in the molecules phthalocyanine and *meso*-tetraphenyl porphyrin as films on disposable screen-printed electrodes to electrochemically deposit and subsequently quantify by oxidation the sugar trehalose using squarewave anodic stripping voltammetry. We then employed the non-enzymatic sensing platform as a method for quantifying *E. coli* trehalose in lysogeny broth culture liquid.

4.2. Materials and Methods

4.2.1. Chemicals

Magnesium phthalocyanine (99% purity), Magnesium acetate tetrahydrate (>99% purity), Calcium acetate hydrate (99% purity), meso-tetraphenyl porphyrin (97%), methanol, reagent grade, sodium acetate (99% purity), dimethylformamide (DMF), D-(+)-trehalose

dihydrate, and lysogeny broth-Miller (granulated) (LB) were purchased from Fisher Science (USA).

4.2.2. Alkali Earth Metal Porphyrin Synthesis

Synthesis of magnesium (II) *meso*-tetraphenyl porphyrin (MgPr).

$Mg(OAc)_2 \cdot 4H_2O$ (260 mg, 1.21 mmol) was added to a suspension of *meso*-tetraphenyl porphyrin (300 mg, 0.49 mmol) in 30 mL of DMF. Then the mixture was heated up to reflux, and NaOAc (40 mg, 0.49 mmol) was added. The reaction was kept stirring and refluxing under argon atmosphere overnight. After the reaction mixture was cooled to room temperature, the solvent was removed under vacuum and the precipitate was washed thoroughly by centrifugation with deionized water (20 mL×3) and MeOH (20 mL×4) until the supernatant was colorless. The residue was dried in vacuum oven to give MgPr as a red purple powder (260 mg, 84%).

Synthesis of calcium (II) *meso*-tetraphenyl porphyrin (CaPr).

$Ca(OAc)_2 \cdot H_2O$ (850 mg, 4.8 mmol) was added to a suspension of *meso*-tetraphenyl porphyrin (300 mg, 0.49 mmol) in 30 mL of DMF. Then the mixture was heated up to reflux, and KOH (400 mg, 7.13 mmol) was added. The reaction was kept stirring and refluxing under argon atmosphere overnight. After the reaction mixture was cooled to room temperature, the solvent was removed under vacuum and the precipitate was washed thoroughly by centrifugation with deionized water (20 mL×3) and MeOH (20 mL×4) until the supernatant was colorless. The residue was dried in vacuum oven to give CaPr as a red powder (300 mg, 94%).

4.2.3. Experimental Setup and Measurements

All electrochemical analysis was performed on a CHI-760E electrochemical workstation

(CH Instruments, USA). 2.5 µL of a 2 mg/mL suspension of either magnesium

phthalocyanine, magnesium *meso*-tetraphenyl porphyrin, or calcium *meso*-tetraphenyl

porphyrin in THF was pipetted onto the carbon paste working electrode of a Dropsens

DRP-110C screen-printed electrode (SPE) and left to dry at room temperature for 5

minutes, allowing a film to deposit on the surface. The modified SPEs were then primed

in 50 µL of phosphate buffered solution, 7.1 pH using cyclic voltammetry (CV) of the

scanning range -1.2 - 0 V, 50 mV/s scan rate, 5 cycles.

The primed electrodes were then calibrated to a blank 50 µL solution of either PBS or

LB, ~7 pH using squarewave anodic stripping voltammetry (SWASV) with a 30 second

deposition time, 2 seconds of quiet time, and scanning range from -1.2 - 0 V with a scan

increment=0.004 V, pulse amplitude=0.025 V, and frequency=15 Hz. SWASV was then

performed on 50 µL samples in PBS or LB containing the following concentrations of

trehalose: 2.5, 5.0, 7.5, 10.0 x 10^{-7}, 10^{-6}, and 10^{-5} M to generate calibration curves on four

separate SPEs.

Electrochemical impedance spectroscopy (EIS) was measured in LB to assess impedance

changes before and after deposition of trehalose on the modified electrode. Parameters

used for EIS 100kHz to 0.1 Hz at open-circuit potential with an AC perturbation of 0.005

V.

To assess double-layer capacitance (C_{dl}) of the modified SPEs before and after electrodeposition, cyclic voltammetry was implemented in a scanning range of $0 - 0.15$ V at scan rates from $5 - 30$ mV/s. The charging current at 0.1 V was then used to establish a linear regression versus scan rate to determine C_{dl} in Farads as given by **Equation 4.1**, where i_C is charging current and v is scan rate [164].

$$C_{dl} = \frac{i_C}{v} \qquad (\textbf{Equation 4.1})$$

4.2.4. Physical Characterization of Metallophthalocyanine and Metalloporphyrins

Working electrodes of the screen-printed electrode were cut and analyzed with scanning electron microscopy (SEM, Hitachi S-3400N, Japan) before and after electrodeposition to characterize changes resulting from trehalose interaction with dropcasted molecule. Attenuated total reflection - Fourier-transformed infrared spectroscopy (ATR-FTIR, Thermo Nicolet 380 FTIR) was performed on the three molecules to confirm the structure in powder form. Powders were also dissolved in deuterated chloroform to give 30 mg/mL for nuclear magnetic resonance spectroscopy (H-NMR, Bruker Avance 600 MHz).

4.2.5. E. coli Growth Procedure

A single colony of K-12 strain *E. coli* grown on tryptic soy agar was inoculated into Luria-Bertani broth (LB) (Fisher, USA). Once bacteria reached the mid-log phase, 100µL of bacteria suspension was added into each culture tube which contains 10 mL fresh LB broth. Culture tubes were placed in the incubator at 4°C and 37°C for 0, 6, 24 and 48

hours. After the incubation time, series of dilutions of each sample were made from which 10 μL was plated on the agar plate and grown for overnight. The next day, the number of colonies was counted. Then, bacteria were autoclaved for 30 mins. After centrifugation, autoclaved broth supernatants were stored at -20°C until electrochemical testing.

4.2.6. Density Function Theory Calculations

The molecular orbitals and electrostatic potential energies (ESP) of magnesium(ii) phthalocyanine, magnesium(ii) *meso*-tetraphenyl porphyrin, calcium(ii) *meso*-tetraphenyl porphyrin, and trehalose were calculated using density functional theory (DFT) method, where the PM7 functional with 6-31+G(d) basis set were used as implemented in Gaussian 09 [196]. The geometries of each structure were fully optimized using the same level of theory prior to ESP and Molecular Orbital calculations.

4.3. Results and Discussion

4.3.1.Physical and Electrochemical Characterization of Metallophthalocyanine and Metalloporphyrins

Following procurement of the powdered magnesium porphyrin and calcium porphyrin, the two synthesized metalloporphyrins were analyzed with ATR-FTIR, demonstrating signature bands of magnesium *meso*-tetraphenyl porphyrin ((d, 8H), 7.82-7.70 (m, 12H); FT-IR: 1666, 1597, 1481, 1443, 1334, 1203, 1180, 1072, 995, 795, 756, 710 cm-1) and calcium *meso*-tetraphenyl porphyrin (1473, 1443, 1350, 1073, 964, 872, 795, 725, 694 cm^{-1}). H-NMR of the metalloporphyrins demonstrated peaks signature of the synthesized

MgPr (δ (ppm) 8.88 (s, 8H), 8.26 (d, 8H), 7.82-7.70 (m, 12H) and CaPr (δ (ppm) 8.88 (s, 8H), 8.25 (d, 8H), 7.88-7.68 (m, 12H) [197, 198]. Commercially, few alkali-earth metallophthalocyanines and metalloporphyrins are readily available, with MgPc being a notable exception. Their synthesis, however, is straightforward and relies on simple processing which make them an attractive option for cost effective catalysts. Additionally, the preparation of these compounds lacks the use of caustic, environmentally harmful substance and could be developed as an environmentally friendly technology.
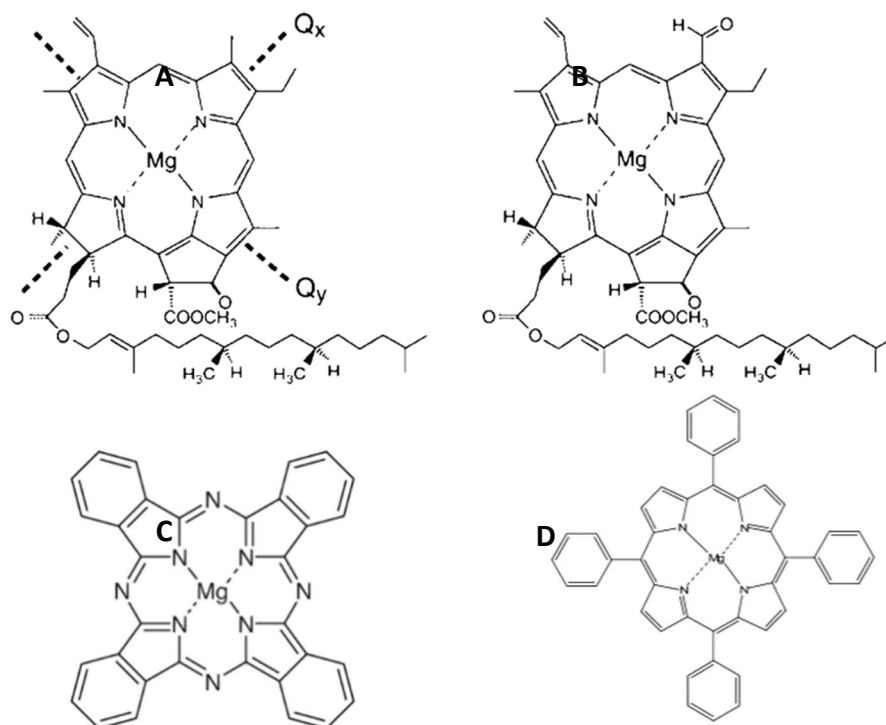
Figure 4. 2. Chlorophyll A and Chlorophyll B (A, B) compared to Magnesium phthalocyanine and magnesium meso-tetraporphyrin (C, D)

It is worth noting that the structures between MgPc, MgPr, and the naturally occurring chlorophylls are remarkably similar as chlorophyll consists of a Mg^{+2} ion in a porphyrin ring, comparison shown in **Figure 4.2**. These structural similarities may also extend to N or O donor ligand binding capabilities and help explain some of the electrochemical behavior displayed by the three molecules to binding trehalose. Magnesium phthalocyanine demonstrates a similar mechanism which was investigated in its interactions with oxygen in water molecules [199]. These interactions demonstrated clear modifications to the electrochemical behavior.
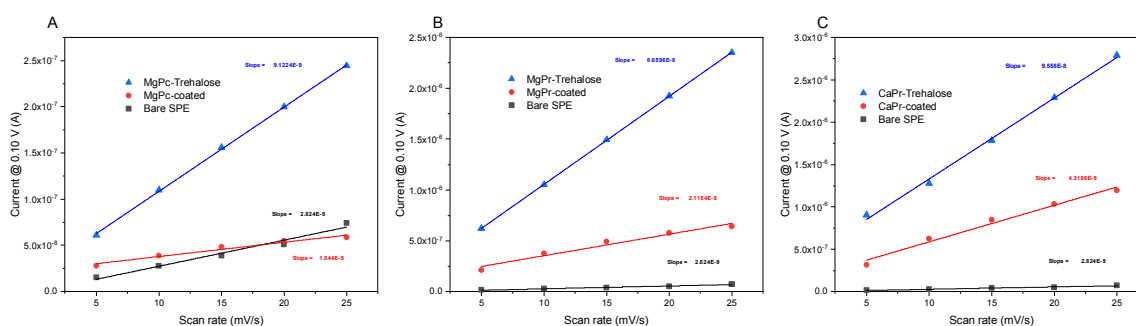
Figure 4. 3. Non-faradaic charging current of cyclic voltammograms at scan rates of 5-25 mV/s where slope equals double layer capacitance (C_{dl}) and is directly correlated to electrochemically active surface area. Black is the uncoated carbon paste screen-printed electrode, red denotes drop casted molecule on the working electrode, and blue represents the electrode post 30 sec of electrodeposition of 10mM trehalose in LB for A. MgPc, B. MgPr, and C. CaPr

An increase of double-layer capacitance in the system post-deposition was confirmed with C_{dl} measurements. These results demonstrate a greater than 4-fold increase in double-layer capacitance for all three molecules (**Figure 4.3**). Electrochemical impedance spectroscopy conducted on the molecules demonstrated an appreciably higher impedance in MgPc at 92 kΩ, 22kΩ higher than the bare carbon paste working electrodes

of the DRP-110 SPEs. Impedance became significantly reduced to 2.9 kΩ following a 30

second deposition of 500 nmol of trehalose (50µL of a 10 mM trehalose in LB solution).

Conversely, the two porphyrins MgPr and CaPr resulted in a lower impedance post-drop

casting and a significantly lower impedance post-electrodeposition (**Figure 4.4**). This

may possibly be the result of the geometry of the molecules, shown optimized in **Figure

4.5** with ESP maps. While MgPc has a mostly planar conformation, MgPr and CaPr

demonstrate a saddle-like shape with the positively charged region of the molecules in a

pocket-like structure. The high impedance can be attributed to the contents of the LB as it

consists of Casein Peptone 10 g/L, Yeast extract 5 g/L, Sodium Chloride 10 g/L. Despite

these intrinsic potential interferents, the system still showed significant reduction in

impedance and supports an increase in conductivity [200].
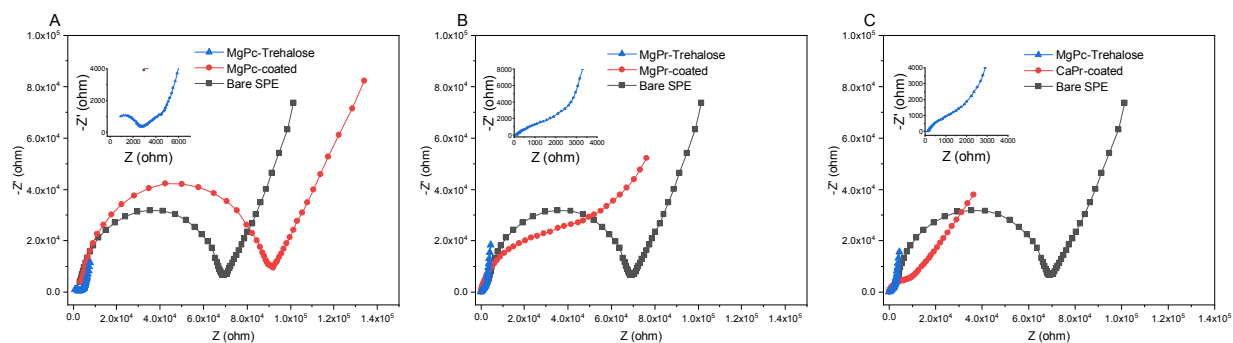
Figure 4. 4. Electrochemical impedance spectroscopy Nyquist plots of an uncoated electrode (black), coated electrode (red), and a coated electrode with trehalose deposited on the surface for A. MgPc, B. MgPr, and C. CaPr. Parameters for EIS were 100kHz to 0.1 Hz at open-circuit potential with an AC perturbation of 0.005 V.

4.3.2. Density Functional Theory Modeling Results

A   B   C
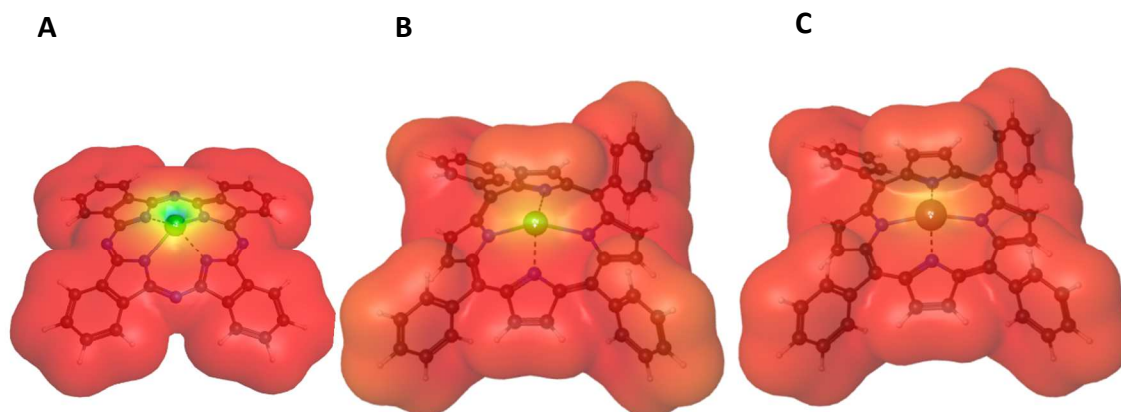
Figure 4. 5. Electrostatic Potential maps with Gaussian optimized 3D geometry of magnesium phthalocyanine (A), magnesium meso-tetraphenylporphyrin (B), and calcium meso-tetraphenylporphyrin (C). The red regions indicate a negative charge while green regions indicate a positive charge.

To better understand potential interactions between trehalose and the drop-casted molecules in this experiment, density functional theory calculations were used to assess highest occupied molecular orbital-lowest unoccupied molecular orbital (HOMO-LUMO) interactions between the analyte sugar and the metallophthalocyanine or metalloporphyrin coatings (**Figure 4.6.**) (values in **Table 4.1**). Modeling of the LUMO of the metallophthalocyanine and metalloporphyrins demonstrated that the positively charged alkali earth metal ion in MgPc is easily accessible due to its dish-like, nearly-2D shape. This shape makes the Mg^{+2} easily accessible for nucleophilic attack by a variety of oxyanions and can result in stacking of MgPc due to water molecule conjugation. These complexes can spontaneously assemble in aqueous solutions and may negatively impact catalytic activity [199]. This was observed when MgPc in THF solution was left in ambient temperature overnight. The solution changed from royal blue to green and all interactions with trehalose did not appear to proceed resulting in unchanged values in

both EIS and C$_{dl}$. Due to this behavior, all solutions had to be made the day of testing and could not be reused on subsequent days. Electrodes with dry, drop-casted films of MgPc did not display the same loss of reactivity with trehalose or color change which may imply water or free oxyanions being a factor in its short shelf life as a solution. The porphyrins' LUMO is less accessible due to the 3-dimensional saddle-shape as shown in **Figure 4.6B & 4.6C**. This conformation likely prevents the stacking with water molecules as observed in the more accessible LUMO of the flatter MgPc molecule that is open for nucleophilic attack but still allows for reactions with negatively-charged oxygen [198]. This may also contribute to selectivity and stability in the proposed trehalose detection platform.
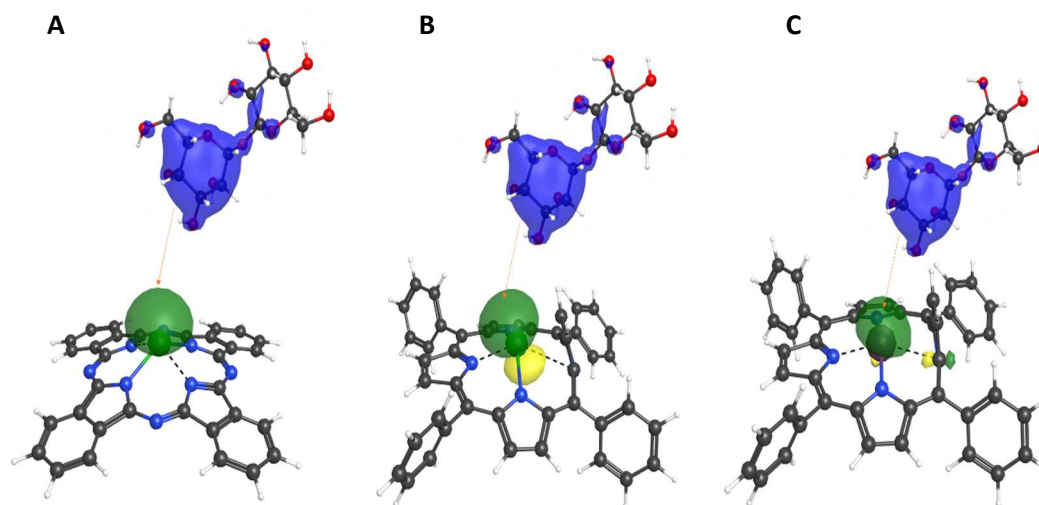
Figure 4. 6. Theorized interactions of HOMO of trehalose (blue) interacting with LUMO of the drop casted molecule A.) Magnesium phthalocyanine, B.) Magnesium porphyrin, and C.) Calcium porphyrin. HOMO-LUMO values for each molecule pictured available in Table S1.

Table 4. 1. HOMO-LUMO energies and their corresponding energy gaps for the three alkali earth-metal organic frameworks and the analyte, trehalose. Energies calculated using PM7 functional with 6-31+G(d) basis set were used as implemented in Gaussian 09.

Compound	LUMO Energy [eV]	HOMO Energy [eV]	Energy Gap (E_g) [eV]
Magnesium Phthalocyanine	-5.605	-44.327	38.722
Magnesium *meso*-tetraporphyrin	7.891	-37.143	45.034
Calcium *meso*-tetraporphyrin	1.361	-37.416	38.777
Trehalose	1.905	-32.164	34.069

4.3.3. Visualizing the Deposition of Trehalose

For visualization of the deposition event on the coated electrodes, SEM was utilized. **Figure 4.4** demonstrates the coated electrodes before and after the deposition of 500 nmol of trehalose (50µL of a 10 mM trehalose in LB buffer, 7.2 pH) and directly correlates to the C_{dl} and impedance of **Figures 4.3 and 4.4,** respectively. Thin films coatings can be seen in the post-deposition photos for MgPc, MgPr, and CaPr in **Figure 4.7D, E, and F**. The formation of the films is incomplete and results in gaps and fissures evident on the surface. Deposition of monosaccharide and polysaccharide films on transition metals is evident with some self-assembled dendrite formation witnessed and is particularly evident on copper with multiple disaccharides however little is available on its behavior with alkali earth metal solid compounds [201] [202]. The behavior of the trehalose may also follow similar behavior and be taking part in a self-assembly event during the electrodeposition stage.
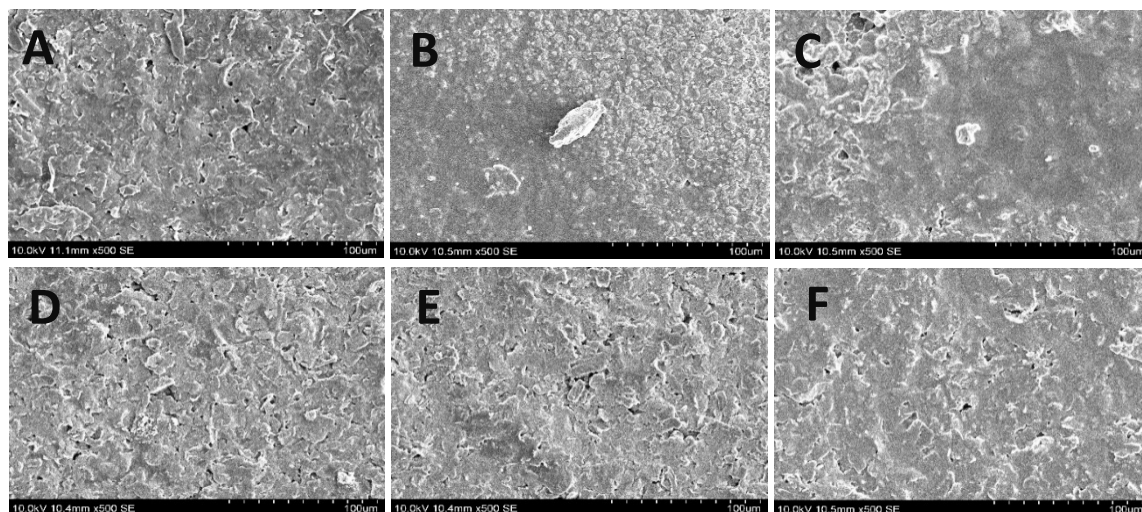
Figure 4. 7. SEM images at 500x magnification, V accelerating voltage showing before (top) and after (bottom) electrodeposition of thin trehalose films at -1.2 V on magnesium phthalocyanine (A, D), magnesium porphyrin (B, E), and calcium porphyrin (C, F)

4.3.4. Electrochemical Quantification of Trehalose

For the quantification of trehalose, squarewave anodic stripping voltammetry was used due to its conveniently short run time and quantitative ability which has been assessed frequently in the deposition and subsequent detection of heavy metal ions in complex media. The deposition voltage of -1.2 V was chosen because it was sufficiently negative to drive deposition of trehalose to peak levels in 30 seconds without initiating a hydrogen evolution reaction in the buffer that higher voltages would have elicited [203]. Screen-printed electrodes were used as opposed to a standard three-electrode system because they are relatively cheap, robust, disposable, and they enable the testing of 50μL samples rather than a sample large enough to immerse three separate electrodes. This mitigates the amount of sample needed to be sacrificed for testing and limits exposure to the operator.
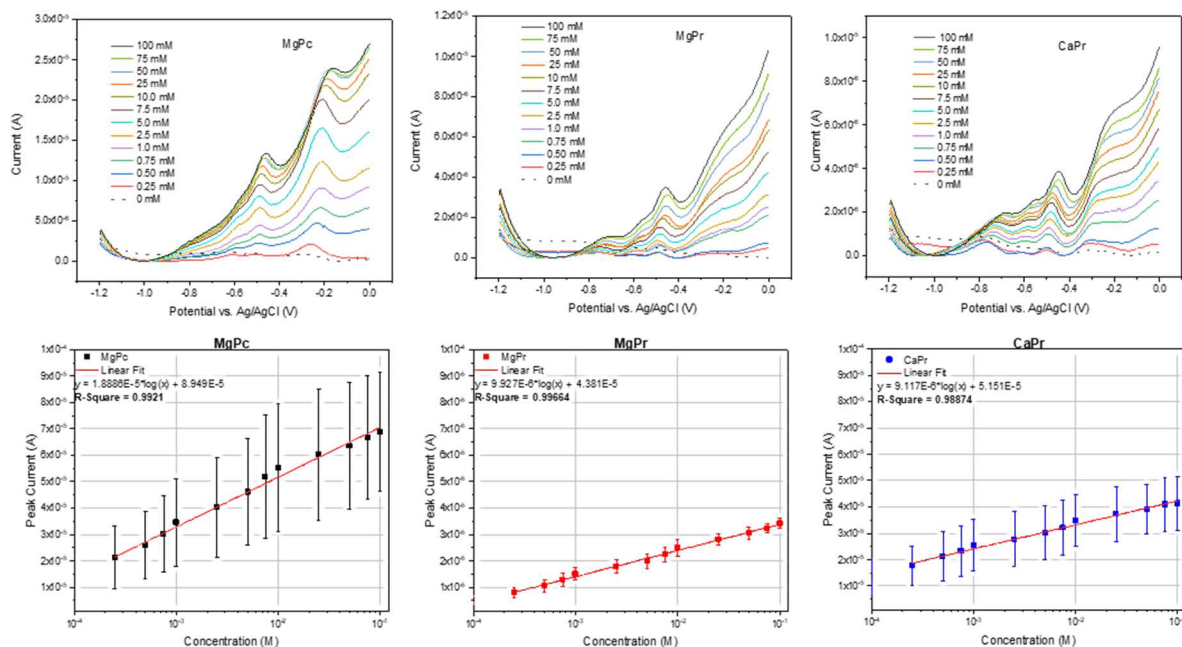
Figure 4. 8. Baseline corrected square-wave stripping voltammograms (top) and calibration curves for currents at 0.248 V for n=4 (bottom) of trehalose in LB at concentrations of 0.25 mM – 100 mM for MgPc (R^2=0.9921), MgPr (R^2=0.9966), and CaPr (R^2=0.9887). Parameters for SWASV are a 30 second deposition time, 2 seconds of quiet time, and scanning range from -1.2 - 0 V with a scan increment=0.004 V, pulse amplitude=0.025 V, and frequency=15 Hz.

As shown in **Figure 4.8 (top)** interaction with increasing concentrations of trehalose in LB resulted in oxidation peaks with highly linear correlation at -0.452 V and -0.248 V. -0.248 V was chosen as peak potential for all three molecules because its peak current linearity was greater than $R^2 = 0.99$ despite not displaying defined peaks in the two *meso*-tetraphenyl porphyrin-coated treatment groups MgPr and CaPr. **Table 4.2** shows limit of detection (LOD) and limit of quantification (LOQ) for the three dropcasted screen-printed electrodes. MgPc displayed a higher sensitivity to trehalose concentration with the value 1.89 x 10^{-5} A/M twice as sensitive as MgPr but varied greatly between its four trials. MgPr and CaPr performed more reliably with very low standard deviation despite

their lower sensitivities. Interestingly, CaPr displayed an additional oxidation peak that

shifted to lower potentials with increasing concentration when compared to MgPc and

MgPr. This may be owed to Ca^{+2} higher reactivity. Ca^{+2}'s reactivity could also be an

explanation for why its linear response to trehalose is lower than the two Mg^{+2} molecules

as it may have interacted with less specificity towards trehalose and instead formed

complexes with components of the LB. Due to MgPc's unpredictable performance and

instability and CaPr's poor linearity, MgPr was determined to be optimal for repeatable

detection of trehalose with its optimal LOD of 0.195 mM versus MgPc's 0.198 mM and

CaPr's 0.610 mM.

Table 4. 2. Comparison of alkali earth metal-organic framework-based squarewave anodic stripping
voltammetry to recently evaluated contemporary trehalose detection methods

Sensing Platform	Buffer (pH)	Processing Time (hr.min.sec)	LOD S:N = 3) mM)	LOQ (S:N = 10) (mM)	Reference
HPLC-RID*	7.3	0.33.00	0.6	2.2	[189]
LC-MS/MS**	7.3	0.31.00	0.000022	0.000028	[189]
Trehalase Enzyme Kit	7.0	1.00.00	0.0063	0.021	[189]
SWASV*** (MgPc)	7.2	0.00.45	0.198	0.660	*This work*
SWASV*** (MgPr)	7.2	0.00.45	0.195	0.495	*This work*
SWASV*** (CaPr)	7.2	0.00.45	0.61	3.3	*This work*

HPLC-RID (high-performance liquid chromatography-refractive index detector)
**LC-MS/MS (liquid chromatography with tandem mass spectrometry)
***SWASV (Squarewave anodic stripping voltammetry)

4.3.5. Trehalose Detection as a Monitor of E. coli Activity
After assessing the three coatings' ability to detect and quantify added trehalose in LB, *E.*

coli were inoculated in a new trial to assess whether the three treatments could quantify

trehalose synthesized by the bacteria. *E. coli*, like many bacteria, synthesize trehalose

from glucose via the trehalose synthase controlled by *otsA* and *otsB* expression for osmoregulation in extreme environments [204, 205]. Trehalose is essential for viability of bacteria in cold environments, so it was valuable to investigate whether an increase in trehalose production per viable bacterium could be assessed via the novel electrochemical platform. Because the system was calibrated in the complex LB medium, interferents from the LB could be negated and would have to be a result of *E. coli* metabolites. **Figure 4.9** demonstrates trehalose quantification via fitting to the linear log calibration curve for all three molecules with slight variation between MgPc, MgPr, and CaPr. Original data show an exponential increase in trehalose concentration until 24 hours for both 4°C and 37°C treatment groups of *E. coli* in LB. However, after corrected to trehalose concentration per colony forming unit (CFU), an interesting trend arose. For 4°C, *E. coli* appeared to have a significant increase in trehalose per CFU, peaking at 12 hours of incubation. Following that point, trehalose concentration decreased as well as the growth rate of bacteria. Conversely, for the 37°C group, trehalose concentration per CFU linearly decreased with time.

One explanation for this phenomenon could be that the *E. coli* exposed to a cold temperature upregulated expression of genes associated with trehalose production in order to stay viable until becoming dormant in the cold temperature between 12 and 24 hours of incubation [205]. The benefit of the proposed electrochemical system is that it can measure these fluctuations in real-time (post ~15 mins of autoclaving or potentially faster with lower volumes of sample) without requiring lengthy processing. This distinction could add utility to current viable count methods as it lacks the

implementation of caustic chemicals and reduces the amount of sample sacrificed for
testing.
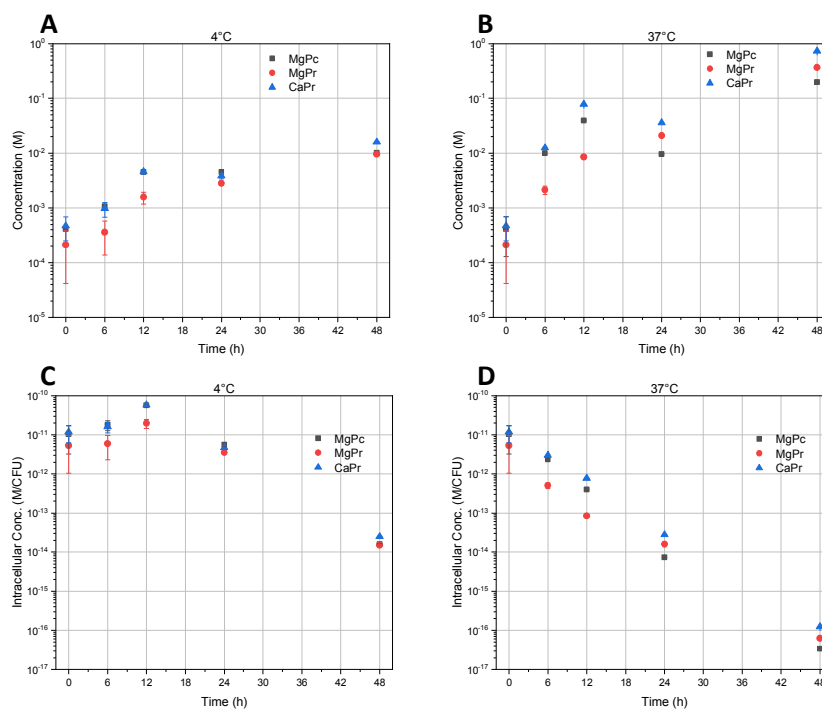
Figure 4. 9. Trehalose concentrations measured from *E. coli* lysate in lysogeny broth using screen-printed
electrodes modified with MgPc (black) MgPr (red) and CaPr (blue). Values were measured in Amperes at
0.248 V using squarewave anodic stripping voltammetry and calculated from calibration curves of MgPc,
MgPr, and CaPr in Figure 5. A and B (top) depict concentrations with standard deviation of whole volume
concentration of trehalose for 4°C and 37°C grown *E. coli*. C and D (bottom) are corrected to show peak
current value per colony forming unit of *E. coli*. Parameters for SWASV are a 30 second deposition time, 2
seconds of quiet time, and scanning range from -1.2 - 0 V with a scan increment=0.004 V, pulse
amplitude=0.025 V, and frequency=15 Hz.

Compared to contemporary methods of sensing, MgPr-modified SPEs have a lower LOD

and LOQ than HPLC-RID and require much less processing and run time than LC-

MS/MS and the trehalase kit. Electrochemical systems have the added ability to be

engineered as point-of-care devices and Internet-of-Things compatible for remote and on-site use as opposed to chromatography and spectroscopy-based methods [175].

4.4. Conclusion

In this paper, we investigated a new approach for applying the commercially available magnesium phthalocyanine as well as our synthesized magnesium porphyrin and calcium porphyrin to electrochemically detect the polysaccharide trehalose via SWASV as a drop-casted film on a screen-printed electrode. The study was focused on characterizing the unique interactions the disaccharide trehalose has with alkali earth metal ions in the +2 state, forming thin films visible with SEM and greatly increasing the double layer capacitance of the working electrode. All three molecules demonstrated highly linear calibration curves but alkali earth metal *meso*-tetraphenyl porphyrins had higher repeatability and lower standard deviation than magnesium phthalocyanine, in part due to their stability. Between the two porphyrins, the magnesium(ii) *meso*-tetraphenyl porphyrin displayed the best performance. As trehalose sensing has little to no precedent in both on-site enzymatic and non-enzymatic sensing, this sensor is the first of its kind and has potential to offer great utility in a multitude of medical, agricultural, and industrial safety and quality control applications.

4.5. Acknowledgments

Dakota State University's High-performance Computing Center. This work was financially supported by the South Dakota Beef Industry Council and the NSF/EPSCoR Track I (no. OIA-1849206).

4.6. Competing Interests

The authors declare no conflicts of interest.

CHAPTER 5: CONCLUSIONS & FUTURE DIRECTIONS

5.1 Conclusions

5.1.1. Overview

Electrochemical biosensors are a rapidly developing technology that continues to diversify and develop to meet the growing need for accurate and simple detection systems such as point-of-care devices. Utilizing redox reactions or changes in conductivity allows detection of analytes that were previously tedious or time-consuming to quantify through standard methods such as HPLC or GC-MS. In this work, the application of biomaterials to electrochemical biosensors was accomplished for analytes in three distinct systems.

5.1.2. Chapter 2 Conclusion

In the first experimental chapter, Chapter 2, a novel system applying lignin-derived graphene oxide and kappa-carrageenan in a composite film of various ratios was created. Kappa-carrageenan was chosen due to its unique effects on the nociceptor system and dopamine levels when administered to rats to stimulate analgesia as well as its structural similarity (two sulfate groups on a disaccharide structure) to the highly conductive glycosaminoglycan, keratan sulfate. This film was drop casted on the surface of a glassy carbon electrode and used to detect dopamine in 0.1M PBS solution by oxidizing dopamine on the surface of the graphene oxide to σ-dopaminehydroquinone. The optimized sensor exhibited a linear range of 1 - 250 μmol L^{-1} and a limit of detection of 0.14 μmol L^{-1} (s/n=3).

5.1.3. Chapter 3 Conclusion

In Chapter 3, nickel sulfide was electrodeposited onto the surface of a glassy carbon working electrode and then utilized to amperometrically detect nitrite via its electrooxidation to nitrate in 0.1M PBS. Nickel sulfide was chosen as a mimic to the catalytic center of nitrogen fixing bacteria's nitrite to nitrate specific enzymes, which are also transition metal sulfides. The two distinct linear ranges exhibited were $0.04 - 1$ µM, $1 - 5.3$ µM of nitrite and a detection limit of 0.01 µM. The facile synthesis, cost-effective reagents, and excellent performance at low concentrations of nitrite confirmed the usefulness of this platform and created potential for future modification through adding conductive materials.

5.1.4. Chapter 4 Conclusion

For Chapter 4, the cryoprotective sugar trehalose was chosen as an analyte to detect as a correlation to microbial presence in complex media due to their increased production of trehalose in cold, dry environments. Alkali earth metallophthalocyanine, magnesium phthalocyanine, and alkali earth metalloporphyrins, magnesium meso-tetraphenyl porphyrin and calcium meso-tetraphenylporphyrin were chosen as modifications for the screen-printed electrode. This was due to literary evidence of unique structures formed between trehalose and alkali earth metal ions of a +2 charge. To calculate potential interactions between these molecules and trehalose, density functional theory was used to predict HOMO-LUMO interactions. Magnesium phthalocyanine was predicted to be the most reactive with trehalose due to its smaller energy bandgap and did display the highest current response but performed inconsistently between trials. Out of the three alkali earth

metal molecules, magnesium meso-tetraphenylporphyrin performed best with the smallest standard deviation between n=4 tests in Luria-Bertani broth.

5.2 Future Directions

5.2.1. The Future of Electrochemical Biosensing Platforms

Despite the limitations of electrochemical biosensors, they are an exciting prospect for a future of simplified sensors with easy-to-use protocols and green components. The great benefit of electrochemical sensors is that they do not have to exist in isolation and can be synergistic with existing technology rather than replacing it outright. A promising example of this type of combined technology is electrochemical high-performance liquid chromatography. This system, which has developed remarkably over the past three decades, consists of an electrochemical sensor utilized in an HPLC post-column to detect elution peaks in amperes rather than absorbance, eliminating the need for a UV signature and allowing a more customizable system for highly sensitive quantification [206-208].

Electrochemical ELISAs have seen similar improvements by moving the assays away from absorbance toward electrochemical or electrochemistry-driven chemiluminescence for quantification that exceeds the standard ELISAs [209, 210]. Similarly, coupling electrochemistry with disposable lateral flow tests has had great success in recent years, relying on the conjugation of antibodies with a redox probe or other easily quantifiable material to monitor binding events. This innovation is transforming what was once a semi-quantitative test with difficult data processing to a simplistic quantitative

technology [211, 212]. In future iterations of the research presented in this dissertation, several major considerations could be made.

5.2.2. Stabilizing the GO:KC Film

For dopamine sensing with the proposed GO:KC film in Chapter 2, stability of the film as a stock solution was poor following an extended period. Cross-linking the kappa carrageenan with stabilizing agents such as calcium chloride or introducing another polysaccharide (e.g., agar, other carrageenans) could potentially improve performance for stability but may come at the cost of conductivity. With a lower overall conductivity, sensitivity of the platform could see a mild to drastic decrease due to the insulating properties of other polysaccharides or changes to surface area due to cross-linking the gel.

To solve this, the carrageenan could be phosphorylated to drastically improve conductivity prior to synthesizing the composite GO:KC film as in **Liew et. al 2017** [213]. Briefly, 10g of a carrageenan blend of kappa- and iota-carrageenans could be dissolved in 500mL of 1% glacial acetic acid, adding 5g of phosphoric acid in 50mL of deionized water with 5mL of formaldehyde simultaneously at 70°C and maintaining temperature while mixing for 8h until a pale-yellow solution forms. Then the solid could be precipitated out by acetone and vacuum dried for use in the sensor propose in Chapter 2.

5.2.3. Fine Tuning the Structure of NiS and Boosting Catalytic Efficiency

One of the primary ways the NiS nitrite oxidation sensor could be improved is through the nano-structure of the catalyst itself. While sufficiently effective in its electrodeposited form, there is potential to increase NiS catalytic effiency through calcination to form better crystalline structure [158]. The semi-amorphous NiS deposited on the electrode in Chapter 3 suffered from slowing reaction kinetics. As a result, it is likely that the linear range shifted midway through the detection range due to a loss of conductivity.

5.2.4. Incorporating Conductive Carbon Materials in the Alkali Earth Metalloporphyrin-based Trehalose Sensor

Because the electrochemical trehalose sensor has the least precedent in literature, it also has the greatest potential for improvement as a sensing platform. Chapter 4 verified that there is some degree of interaction between the trehalose sugar and alkali earth metal ions in complex media such as LB on its own but it lacked a significant conductivity, especially in the meso-tetraphenylporphyrin compounds. To improve this factor, the compounds could be dropcasted or electrodeposited on conductive carbon nanotubes as accomplished in previous work [112].

Being phthalocyanine and porphyrins respectively, the three molecules in Chapter 4 have potential for functionalization to form metal organic framework coatings with covalent linkages between molecules rather than self-assembled films as in dropcasting. This could also greatly enhance conductivity and prevent nonspecific interactions with the ring-shaped phthalocyanine and porphyrin molecules [214, 215].

APPENDIX A: ACCEPTED GRANT PROPOSAL

Accepted Grant Proposal to South Dakota Beef Industry Council 2019

SOUTH DAKOTA BEEF INDUSTRY COUNCIL RESEARCH FULL PROPOSAL

TITLE: [**GRAPHENE-BASED ELECTROCHEMICAL SENSOR FOR DETECTION OF SALMONELLA IN BEEF PRODUCTS**]

PROJECT LEADER(S): [**Zhengrong Gu,** Ag & Biosystems Engineering Dept., South Dakota

State University, Address: 1400 N Campus Dr., Brookings, SD 57007, Email:

zhengrong.gu@sdstate.edu,] Phone: 605-688-5372

PROJECTED DATES: [start Oct. 10, 2019, and completion Oct 09, 2021. 2-year project.]

PROJECTED COSTS: 1st yr.: $34,652___ 2nd yr.: $35,483___ Total: _$70,135___

SUMMARY:

Salmonella contamination poses great risks to human health and the beef product industry

alike. In the USA in 2018, >12 million lb. of beef was recalled due to *Salmonella* alone.

To prevent more recalls and potentially devastating health crises, a new *Salmonella*

sensor based on graphene is being proposed. The sensor will utilize a composite of

biomass-derived graphene and cheap, natural polymers to quantify *Salmonella*

metabolites and ultimately a specific biomarker gene of *Salmonella* through their

electrochemical signatures. Preliminary studies with these materials and the model

molecule dopamine have already demonstrated a limit of detection of 5 x 10^{-8} mol/L (~80

nanograms/mL) with great potential for further optimization.

STATEMENT OF PROBLEM:

According to the USDA Food Safety and Inspection Service's Summary of Recall Cases, 12,093,271 lbs. of raw non-intact beef were recalled for *Salmonella* contamination in 2018 [216]. Additionally, anti-microbial resistant (AMR) *Salmonella* cases have reached ~6,200 culture-confirmed infections in the United States by December 2016 [217]. A prominent form of this AMR *Salmonella* is the Dublin serotype, a cattle-adapted type of the pathogen . There is a clear, negative relationship between the rise of zoonotic *Salmonella* contamination and the food industry that needs to be addressed through preventative measures that spare consumers from potentially lethal health risks and minimize product loss for beef producers. The optimal solution to both issues is rapid, more reliable detection of *Salmonella* contamination in beef animals and beef products alike.

Currently, *Salmonella* detection in beef products relies heavily on polymerase-chain reaction (PCR), which selectively replicates the DNA of chemically degraded *Salmonella* using a single-stranded primer and selected enzymes in order to have enough DNA to quantify via fluorescent tag molecules [218]. While usually highly accurate, this process requires many temperature cycles and has proven to be less than efficient at preventing large-scale recalls due to its time constraints and expertise requirements. Similarly, agar plates cultured from swabs of meat samples are used to count colony forming units (CFUs). This requires considerable time (>24 hrs.) to achieve a quantifiable level of growth from samples of contaminated products. By which time, they may have already contaminated clean products and inoculated more *Salmonella*. To combat these

shortcomings, producers need access to real-time detection systems so that they may protect consumers and prevent loss of valuable products.

RESEARCH AREA ADDRESSED:

Pathogen sensing, electrochemistry, rapid bacterial detection in industrial capacity, food product loss mitigation

PROPOSED RESEARCH:

This proposal will attempt to mitigate potential human health hazards and large-scale beef product losses through rapid electrochemical sensing of *Salmonella* metabolites and/or species-specific DNA sequences. Electrochemical sensors are quickly becoming standard in a variety of biological applications. Most notably, blood glucose sensors have become significantly faster, cheaper and more reliable upon the redox sensor utilizing glucose oxidase [219].

Linear sweep potential voltammetry is method that is quickly gaining traction in biosensing as it elicits highly sensitive and repeatable results. Some variations on this method include differential pulse voltammetry (DPV) and square-wave voltammetry (SWV), both of which are being proposed as methods in this research. DPV enables us to sense a target molecule's peak on a current vs. potential graph. The potential of the peak determines the molecule's identity while the current of the peak allows us to quantify its concentration.

Graphene is a material composed entirely of carbon atoms bound to each other in a 2-dimensional, hexagonal lattice (**Figure 1**). A difficult material to synthesize until Nobel prize-winning methods in 2010, graphene is quickly becoming an optimal material for sensing due to its exemplary charge transfer ability [220]. As a material for sensing, graphene has already been implemented extensively for electrochemistry. In this research, we will use it to amplify signals created by a chosen material's redox behavior with a target. In this proposal, we will focus on biopolymers.
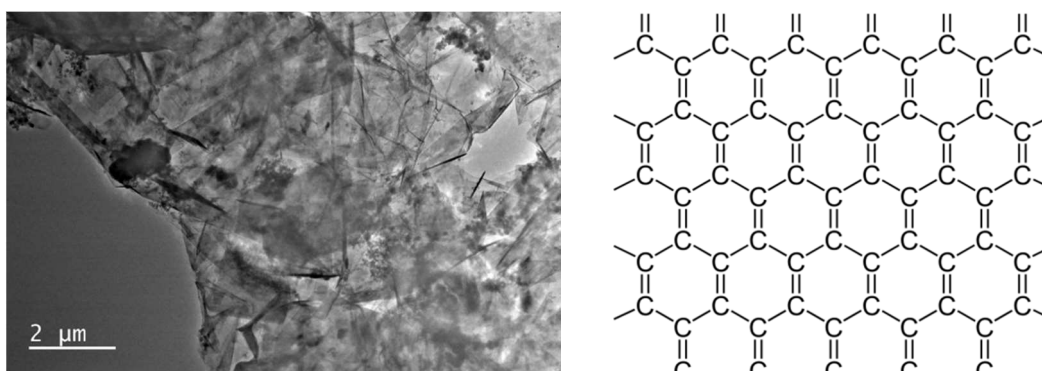
Figure A.1. Transmission electron micrograph (left) and Lewis structure (right) of graphene

Naturally occurring biopolymers are ubiquitous throughout the whole of biology and form the structure of complex life. They can be composed of anything from strands of proteins, in the case of silk, to polysaccharides such as chitosan or cellulose. Utilizing functional groups on the polymer, we can target specific molecules, evident in several studies utilizing chitosan for sensing different variables in blood [51, 221, 222]. For this research, a polymer that interacts chemically with our target molecule, also known as a biomarker, will be chosen.

Biomarkers are molecules associated with tracking or identifying specific organisms or biological phenomena. They can include, but are not limited to, metabolites such as sugars, proteins, lipids, volatile organic compounds, and DNA sequences of genes specific to a species, genus, etc. [223]. When considering *Salmonella* and electrochemical sensing, we have determined two separate biomarkers to pursue simultaneously in our research: trehalose and DNA sequences of the Vi capsular antigen gene in *Salmonella.*

Trehalose, pictured in **Figure 2**, is a disaccharide associated with promoting thermal stability and quick access to energy across the spectrum of biology. According to several studies, *Salmonella spp.* are especially prone to producing this sugar to prevent desiccation and membrane damage due to extreme temperatures [224-226]. When temperatures return to favorable levels, *Salmonella* will employ the enzyme trehalase to cleave trehalose into two glucose molecules that will quickly be reabsorbed by the cells for energy [227]. According to one study specifically focusing on *Salmonella* survival behavior in stressful conditions like those of a meat storage facility, trehalose biosynthesis was more likely to occur [228]. Several studies have successfully undertaken trehalose quantification through solely chemical means via high-performance liquid chromatography (HPLC) and Gas Chromatography-Mass Spectrometry (GC-MS). Through HPLC, one lab was able to detect trehalose synthesis peaked at in aerobic respiration 96 hr post inoculation at 9 pmol/cell, nearly double that of anaerobic respiration in yeast [229]. A later study was able to quantify as low as 0.07 mmol of trehalose in yeast via HPLC [178]. Aside from simple molecular targets such as trehalose, even more specific targets exist such as nucleic acids.
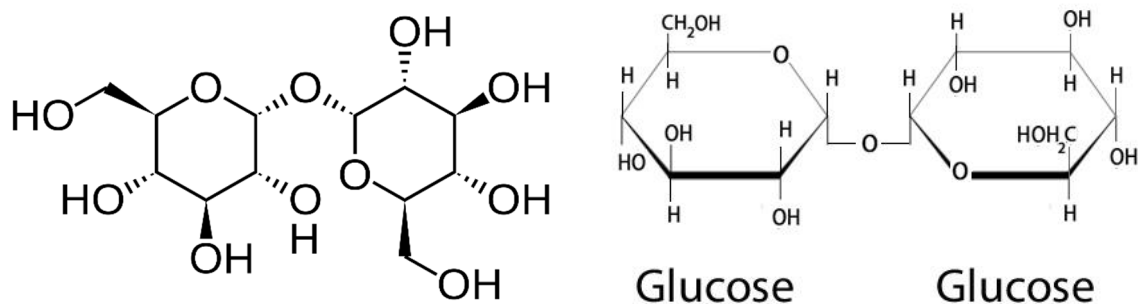
Figure A.2. Two different depictions of the sugar trehalose**,** a 1,1 glycosidic bond between to α-glucose units.; utilized by Salmonella spp. to prevent desiccation and thermal stress

Due to DNA's highly selective binding and its unique order of base pairs in respect to the organism from which it is extracted, DNA has potential to be one of the most specific and reliable biosensors for virtually all living organisms and their specific sequences. For this research, we will target the Vi capsular antigen gene of *Salmonella*. The conserved Vi capsular antigen gene region is responsible for a universal feature on *Salmonella* [230]. Being present in all *Salmonella spp.*, the Vi capsular antigen gene region is an optimal target for specificity in identifying *Salmonella* on meat [231].

OBJECTIVES:
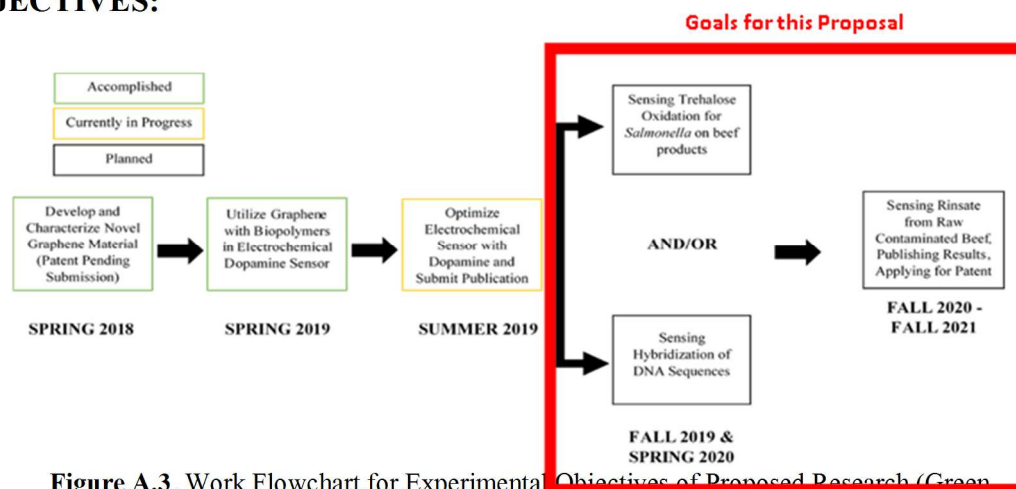
Figure A.3. Work Flowchart for Experimental Objectives of Proposed Research (Green Outline=Accomplished, Yellow Outline=In Progress, Black Outline=Planned)

The overall objective of this research is to develop a graphene/biopolymer composite-based electrochemical sensor for detecting *Salmonella* based on its biomarkers. To maximize productivity and ensure scientific progress, we will instigate several potential pathways for this research to progress. We will focus on the previously outlined novel biomarkers for *Salmonella*.

A. Trehalose

Initially, we will focus on the *Salmonella* metabolite **<u>trehalose</u>**. Being a natural mechanism for *Salmonella* to survive extreme temperatures, it is likely that the sugar trehalose will be present at quantifiable levels on infected meat in cold storage and processing facilities. As a sugar, it will readily dissolve in liquid from a low-volume misting apparatus that can then be collected and quantified via a 3-electrode system as in the concept example, **Figure 4**. Using previously cited methods for trehalose quantification, we will compare our novel results with existing methods to assess potential for optimal results. If suitable results are obtained at realistic, in-facility concentrations, we will develop this option.
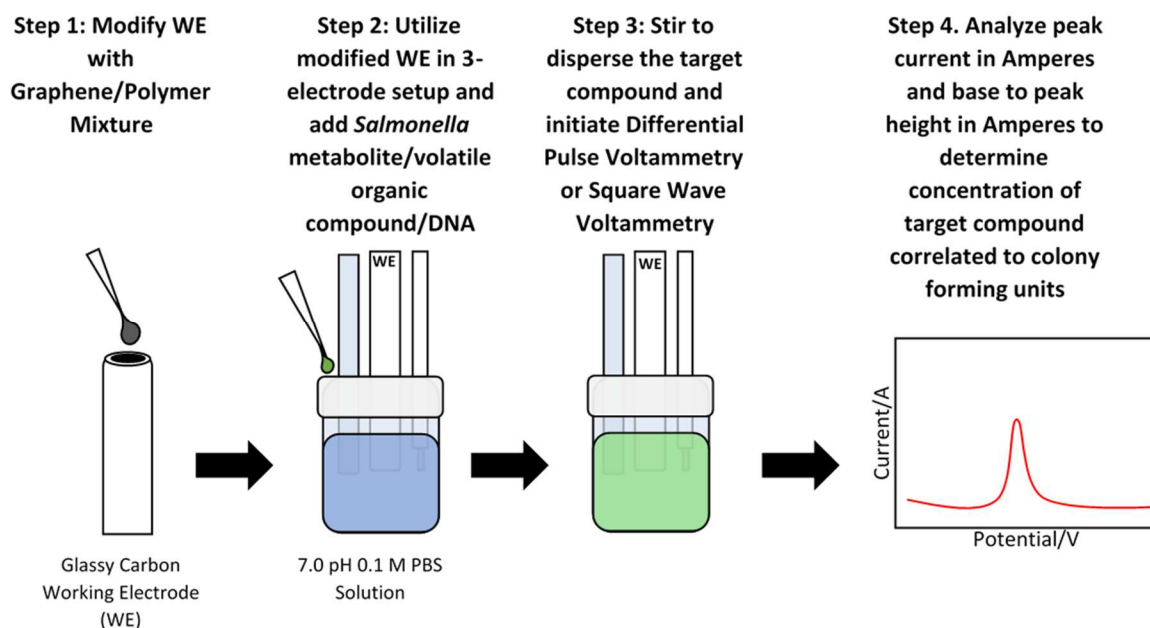
Figure A.4. Proposed experimental scheme for determining target compound concentration in 10 mL of PBS via differential pulse voltammetry and/or square wave voltammetry

B. DNA Sequences Specific to *Salmonella spp.*

Utilizing the Vi capsular antigen gene as a target, we will order synthetic complementary DNA probes adsorbed to magnetic nanoparticles for detecting DNA from lysed bacterial cells (concept shown in **Figure 5**). Fe3O4 and FeCo nanoparticles with size distribution between 20 to 50 nm, synthesized through co-precipitation of Fe2+ and Fe3+ salts (e. g. Fe(NO3)2 and Fe(NO3)3) in alkaline medium will be used as transition metal catalysts to prepare graphene coating layer from DDGS. All thermochemical processes will be carried out in a tube furnace under accurately controlled atmospheric and heating conditions. For details, Fe3O4 and FeCo nanoparticles suspension will be mixed completely and evenly with DDGS. The mixture will be further dried with freeze drying, then carbonized at 400 C in N2

atmosphere for 20 min. The as-prepared char and nano-magnetic particles mixture will be cooled down and soaked into KOH solution for 1 hour. This mixture will be dried at 105 C for 24 hours. After drying, the graphenization and activation will be carried out at 700 C for 1 h in N2 atmosphere. The obtained samples will be cooled down in furnace with N2 atmosphere protection. Then graphene coated magnetic nanoparticles will be washed with deionized water to pH 7, and dried at 105 C overnight under vacuum before further characterization or evaluation. The DNA will be accessed either by mechanical lysis with silica particles or chemical lysis via isopropyl alcohol and heat (~70 C). We will investigate DNA in the picomolar (pM) – micromolar (uM) range.

EXPERIMENTAL DESIGN:

Utilizing the methods described the Objectives section, we will ultimately culminate this research in a design for monitoring rinse water (or saline solution) from the surface of meat products for *Salmonella* trehalose and/or DNA sequences from the Vi capsular antigen region (**Figure 6**). The initial concepts of both sensor platforms, trehalose and DNA, will be explored simultaneously to efficiently explore the best
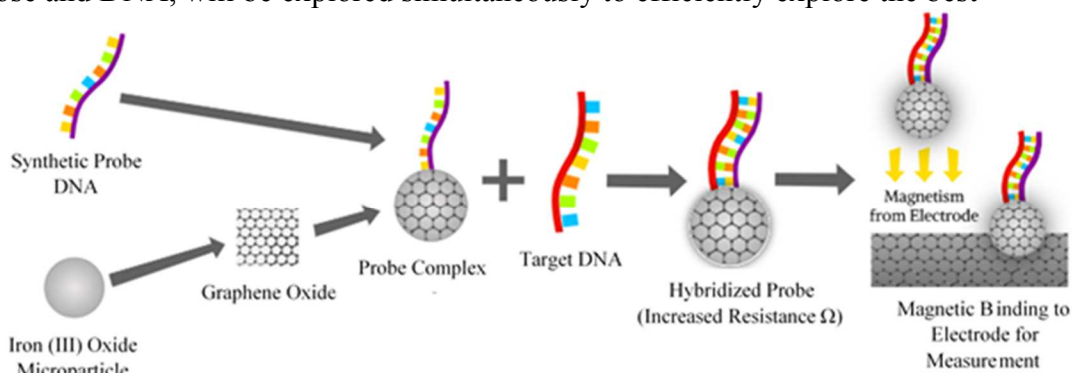
Figure A.5. Concept for capturing Salmonella target DNA with coated nanoparticles which will then bind to glassy carbon electrode

sensing method for *Salmonella*. We will plan to operate with large (100uM)

concentrations of trehalose and DNA respectively in the first phase of these experiments

and then systematically decrease the dosage to realistic, in-facility concentrations.
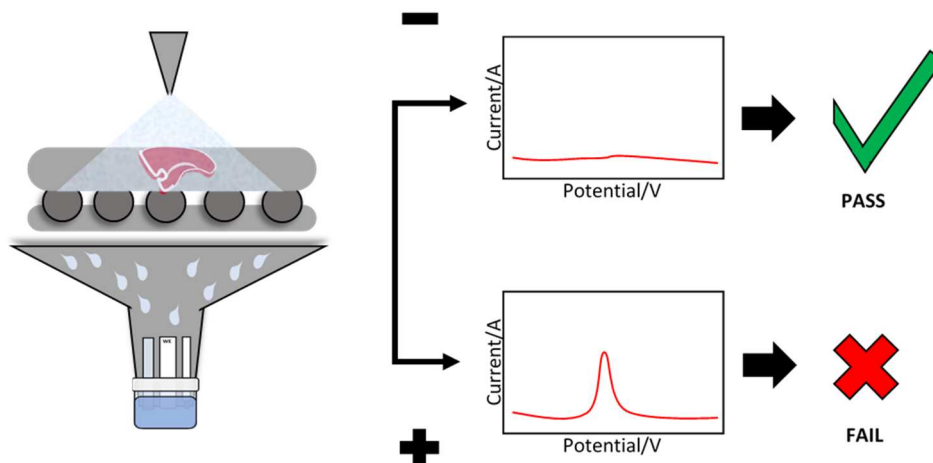
Figure A.6. Example of a final concept for Salmonella 3-electrode detection via rinsate containing target molecule from beef product on conveyor belt

PRELIMINARY RESULTS:

Utilizing our novel method graphene and a combination of biopolymers, we were

able to competitively sense dopamine in 0.1 M PBS solution. With our results, we were

able to generate R^2 values of 0.99172 and 0.99542 for ranges of 0.5 uM-17uM and

50nM-1.5nM, shown in **Figure 7**.
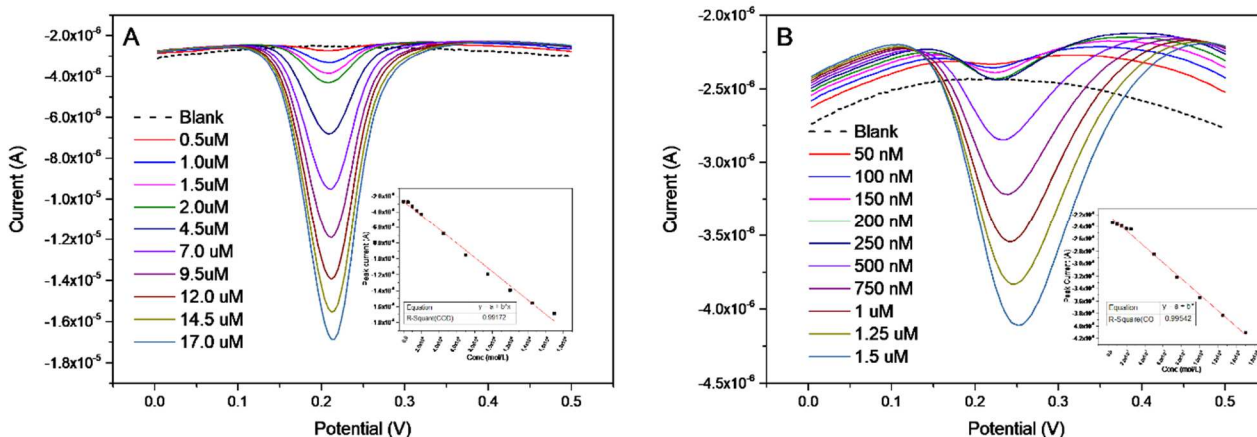
Figure A.7. Preliminary results of patent-pending graphene material with carrageenan as a composite film drop-casted onto glassy carbon working electrode for dopamine detection at A) 5 x 10-7 mol/L – 1.7 x 10-6 mol/L (R2 for peak current=0.99172) and B) 5 x 10-8 m

STATISTICAL ANALYSIS:

Due to the linear relationship of calibration curves using modified glassy carbon electrodes and the relatively simple processing for determining a line of fit, statistical analysis for this research will be straightforward and simplistic. Results of trehalose and DNA detection will be replicated five times to afford four degrees of freedom. Analysis of variance, confidence intervals, and Student's T-test will all be utilized to determine the limit of detection, replicability, and sensitivity of the sensing platform. **Figure 8** displays linear fit of sensing with the novel graphene material/biopolymer composite on glassy carbon, R^2=0.99172. Results such as **Figure 8** are typical when utilizing materials that elicit predictable redox behaviors with target molecules.
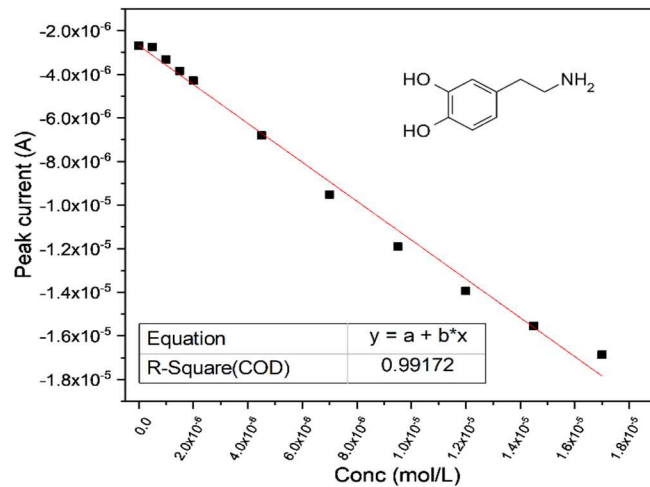
Figure A.8. Linear calibration curve of preliminary results for model drug dopamine (top right) using graphene/biopolymer modified glassy carbon electrode

APPENDIX B: ENERGY STORAGE RESEARCH

Rapid thermochemical conversion of lignin to porous activated carbon for energy storage in supercapacitors and microbial fuel cells

Abstract: Naturally occurring biopolymers are an abundant resource with great potential for energy storage following thermochemical conversion to activated carbon and/or graphene-like materials due to their unique structural and chemical compositions. Lignin is one of the world's most abundant biopolymers but is generally regarded as a waste product due to the difficulty and cost associated with converting it to more useful derivatives. Alkali lignin was converted to graphene oxide directly on current collector material in a base-catalyzed thermochemical conversion in <1 min. Nickel foam is favored as a current collector material because of its high conductivity and high surface area for holding active materials but due to its cost, environmental toxicity, and potential threat to microbes in microbial fuel cells (MFC), it was substituted with carbon cloth and carbon aerogel respectively. Cyclic voltammetry and electrochemical impedance spectroscopy were measured on all samples. Alkali lignin on carbon aerogel yielded the highest specific capacitance at 119 F/g. After 1000 charge/discharge cycles, the aerogel sample had a charge retention rate of 94.26% while carbon cloth samples maintained a rate of 60% after 1000 cycles.

Introduction

Supercapacitors represent one of the most promising technologies for better energy storage in multiple platforms including electric vehicles, wind turbines, and other electrical devices due to their highly tunable nature, environmental friendliness, and variety of materials available for synthesis [232]. Despite this promise, they have yet to compete with more established technologies such as lithium-ion batteries due in part to their low energy density [233]. To improve these shortcomings, new conductive materials such as graphene have been focal to improving supercapacitor performance due to the material's unique properties.

Graphene is the material of choice for many supercapacitors today because of its high surface area, modifiable surface functional groups, and extremely thin nanosheets. Theoretically, graphene should perform at a specific capacitance of 550 F g^{-1} but typically fails this performance due to aggregation of graphene sheets as a result of poor conditions for synthesis, which are typically difficult to maintain in most conventional settings [234, 235]. In a typical synthesis, a pristine form of graphite is exfoliated in hydrazine via a process termed Hummer's Method to obtain high quality graphene oxide which is then reduced via a variety of methods to obtain pristine graphene nanosheets [236]. Newer, more facile methods are being produced but they still suffer from a great deal of complexity when compared to other, simpler preparations for graphene's main competitors for electrode active material, petroleum-derived carbon blacks, activated carbons, etc. [237]. The major shortcoming of many of these materials is that they are not

environmentally or fiscally sustainable, which limits the impact of high-capacity supercapacitors using carbon materials in today's energy market [238].

To meet this demand, new materials are being developed from low-value biomaterials and wastes. One of the more prominent materials being used for this purpose is lignin, a structural, polymeric component of most plants that is generally regarded as waste in the paper manufacturing industry due to its undesirable effect on paper quality [239]. One reason lignin is a high-priority candidate for graphenization is its repeating phenolic lignol subunits which already resemble graphene's sp3-hybridized carbon hexagonal structure [240]. A particularly innovative method of lignin conversion that has been pursued recently was the direct graphene oxide synthesis of lignin via laser lithography [241].

In this study, graphene oxide is synthesized via a new, capacitive discharge method directly on the lignin slurry-coated current collecting material to minimize the number of steps and eliminate the need for a binder such as PTFE. This new, facile method presents opportunities in supercapacitor preparation without the need for tedious preparation as in standard methods.

Materials and Methods

Electrode Material Preparation and Assembly

Electrodes were prepared by applying a thin layer of an alkali lignin and 3M KOH paste to either carbon cloth (CC) or carbon aerogel (CA) current collectors (2 cm dia.). The lignin on each electrode was then converted into a graphene-like material using a one-step thermochemical conversion process in which a high voltage low current capacitive discharge was applied directly on the dried paste-covered current collector. Once converted, the electrodes were indirectly sprayed with ethanol to rinse away unconverted lignin and dried in a 105°C incubator for 15 mins followed by 12 h overnight in a vacuum oven at 65°C. Two electrodes of the same substrate were then assembled into coin cells with a 6M KOH electrolyte. The coin cell assembly is shown in **Figure B.1.**
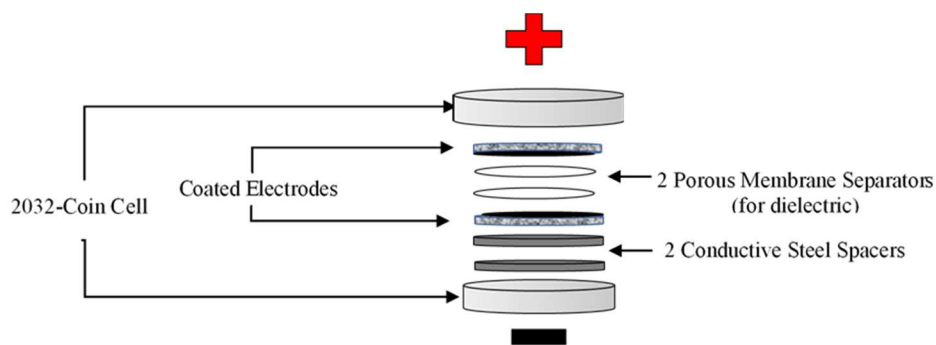
Figure B. 1. Anatomy of 2032-type Coin Cell Supercapacitor with an aqueous KOH electrolyte saturating each layer

Physical Characterization

Transmission electron microscopy and high-resolution transmission electron microscopy were performed on a JEOL JEM-2100 with an accelerating voltage of 200kV on a Cu grid with carbon film background, .Scanning electron microscopy was performed on a Hitachi S-3400N microscope with 100kV accelerating voltage. Powder x-ray

diffractometry was performed on a Rigaku SmartLab, λ= 1.5418 Å). Raman spectroscopy was performed on a Horiba labRAM spectrometer.

Electrochemical Analysis and Characterization

All electrochemical tests were performed on a Biologic SP-150 electrochemical workstation. Cyclic voltammetry (n=4, scanning rate=100 mV/s) and electrochemical impedance spectroscopy were used to observe the current and resistance of the supercapacitor. An additional cyclic voltammogram (n=5000 scanning rate=100 mV/s) was run on a cell with carbon cloth as the substrate to test for cyclic stability. The equation below was used to calculate the specific capacitance of each cell.

$$Csp=(2*I)/(m*dV/dt) \qquad \textbf{(Equation B.1.)}$$

Where I is the current applied in Amperes, m is the average loading on each electrode in grams, and dV/dt is the scanning rate of the cyclic voltammogram in V/s.

Results and Discussion:

Physical Characterization Results

Microscopy of the novel lignin material demonstrated a highly porous structure on both the micro- and nano- level as shown in **Figure B.2**.This demonstrated that during the

conversion processes detailed in the methods, pores were likely formed during the discharge of the capacitor, resulting in the heated gaseous component rapidly escaping the lignin slurry and forming the complex heterostructure demonstrated. This is congruent with studies that used similarly rapid methods of synthesis for graphene and hierarchical porous activated carbons [242-244]. High resolution-transmission electron microscopy demonstrated a successful crystal lattice formation through this conversion method, as shown in **Figure B.4.** This lattice, which demonstrates a crystal lattice gap between 3.2 – 3.4 Å, agrees with graphene nanostructural characterization and is demonstrable in both instances of Figure B.3 (left and right).
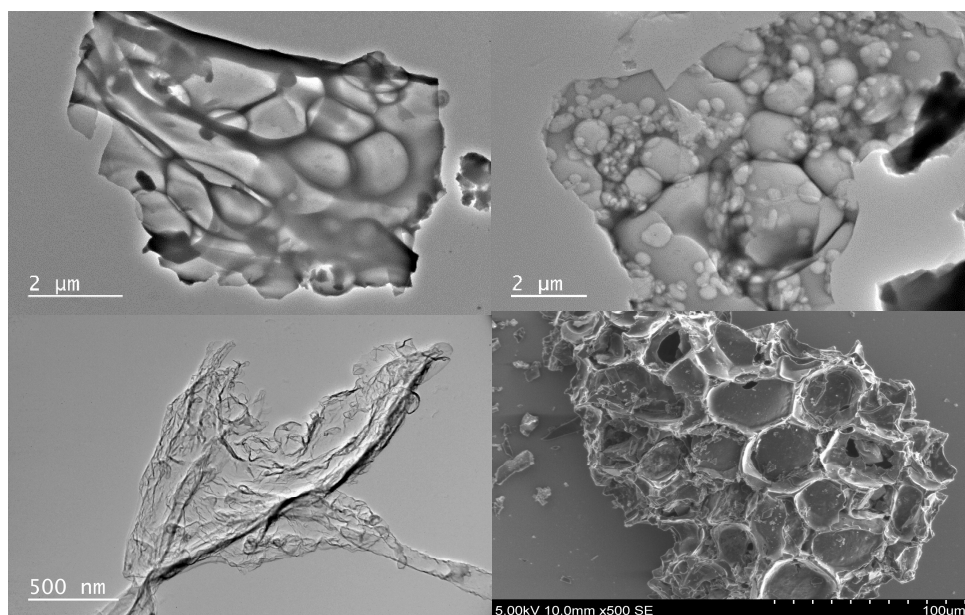
Figure B. 2. TEM (Top left and right, bottom left) and SEM (bottom right) of graphene oxide synthesized via novel thermochemical conversion
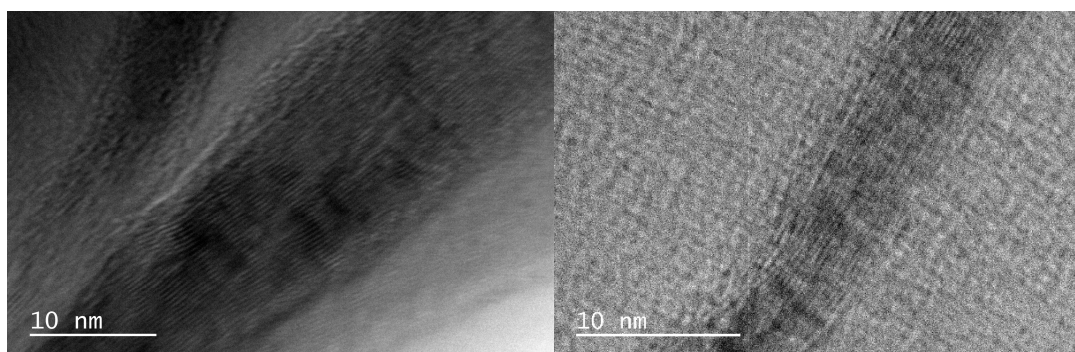
Figure B. 3. HR-TEM at 1.2 M x magnification, 200 kV accelerating voltage of lignin-derived graphene crystal lattices (0.34 nm)

Figure B.4. represents the powder x-ray diffraction data for the lignin-derived graphene and shows a prominent peak at 26° as well as a weaker peak at 55°, as is expected with crystalline graphene [245]. Raman spectroscopy in **Figure B.5.** also supports sp-sp2 graphene formation from the lignin substrate but lacks a prominent 2-D band which could be a result of graphene nanosheet aggregation either during the synthesis itself or when preparing the sample for spectroscopy [118].
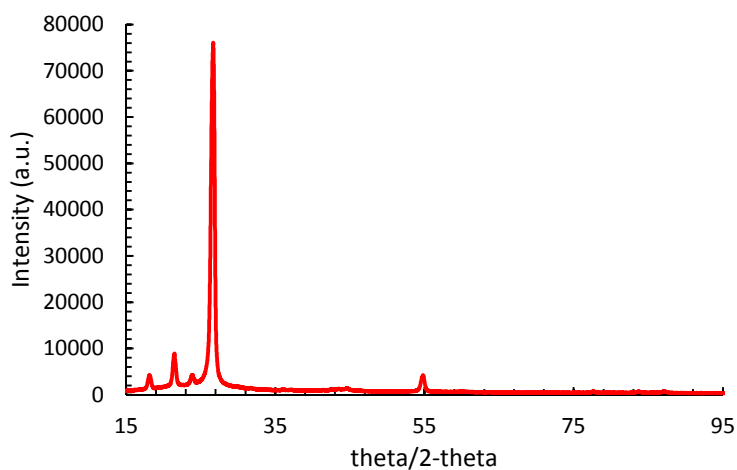
Figure B. 4. Powder XRD of graphene oxide powder scraped manually from surface of carbon cloth current collector
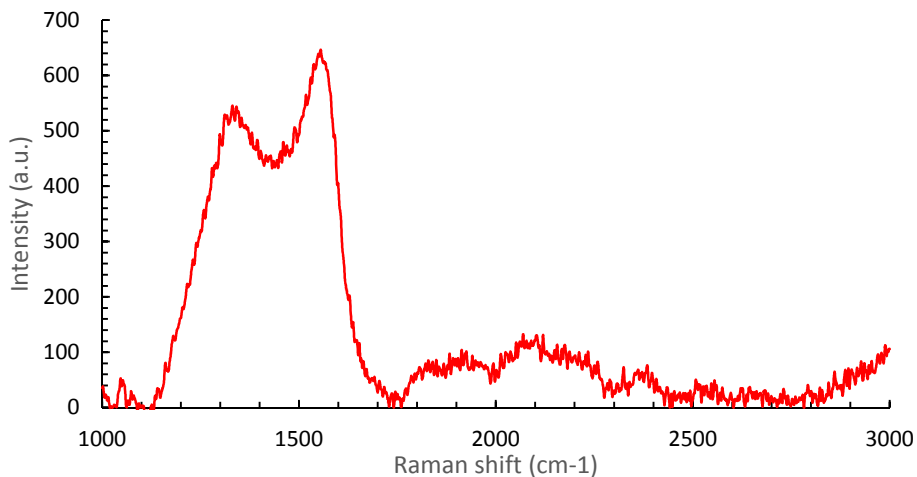
Figure B. 5. Raman spectroscopy of lignin-derived graphene oxide

Specific Capacitive Performance and Impedance Values

The application of active lignin to a carbon cloth current collector increased the specific capacity of the supercapacitor from 0.06 F/g to 69.80 F/g (**Figure B.6.)**. The specific capacity of the supercapacitor using a carbon aerogel current collector increased by a factor of 21.24 from 5.56 F/g (blank CA) to 119.05 F/g (**Figure B.8.**). The carbon cloth supercapacitor exhibited a Csp of 69.80 F/g, a resistance of 2.12 Ω, and a 54.55% retention rate over 5000 cycles (**Figure B.9.**). The carbon aerogel supercapacitor exhibited a Csp of 119.05 F/g, and a resistance of 2.75 Ω. Carbon aerogel performed better as a current collector than carbon cloth however carbon cloth is far more cost effective. When only unconverted lignin was applied to the substrates, the specific capacitances were still lower than that of the supercapacitors with converted lignin. In agreement with the electron microscopy, it is likely that the novel process produced graphene-like material that is responsible for the increase of specific capacity for each substrate.
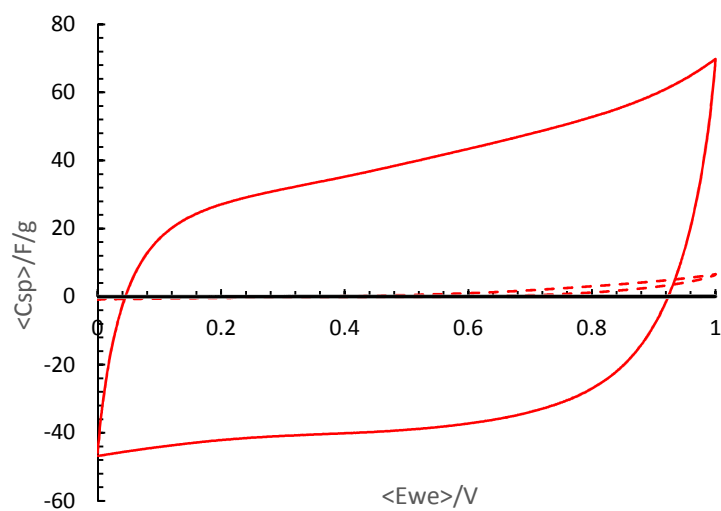
Figure B. 6. Supercapacitor CV performance of samples on carbon cloth. Unconverted lignin (red dashed line) exhibited only slightly higher specific capacitance (Csp) of ~2 F/g than blank carbon cloth (black dashed line) and converted blank carbon cloth (black solid line) which both obtain <1 F/g. Converted lignin on carbon cloth (solid red line) exhibited a Csp of 69.79 F/g.
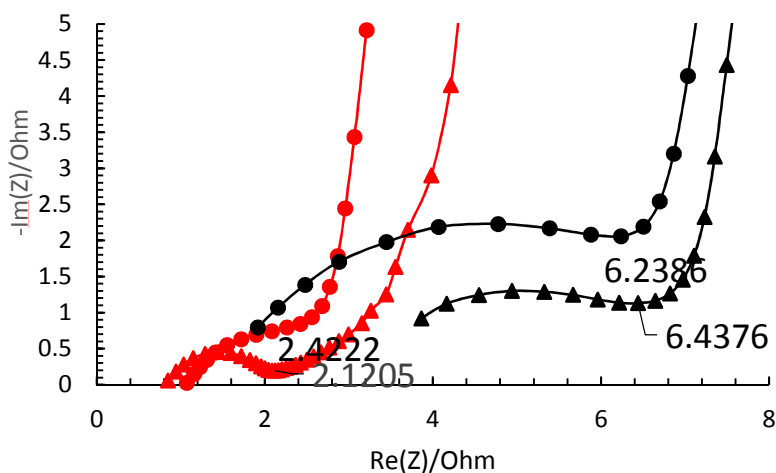
Figure B. 7. EIS performance of carbon cloth samples. Unconverted lignin on carbon cloth (red circles) exhibited a resistance of 2.4 Ω while converted lignin on carbon cloth (red triangles) exhibited a slightly lower resistance of 2.12 Ω. Unconverted bare carbon cloth (black circles) exhibited a 6.2 Ω resistance while converted bare carbon cloth (Black triangles) exhibited a resistance of 6.43 Ω.
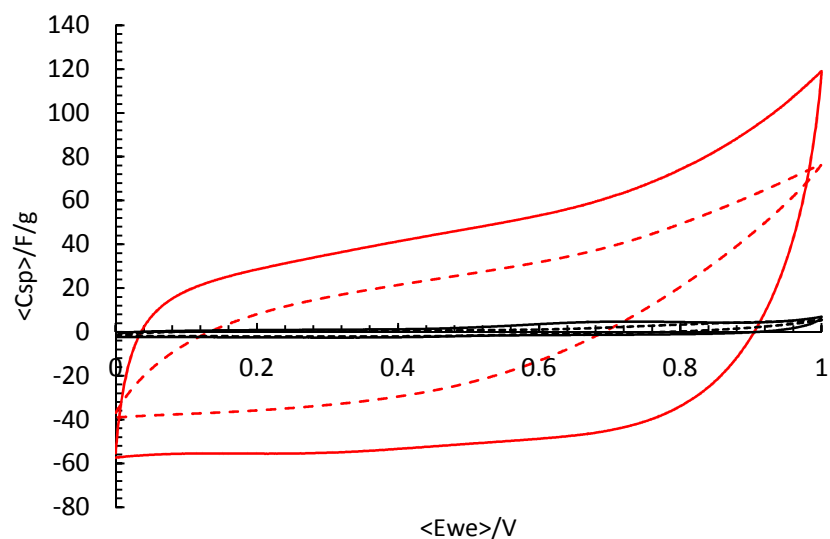
Figure B. 8. CV of carbon aerogel samples. Blank aerogel and converted blank aerogel (dashed black line and solid black line respectively). Nonconverted lignin (red dashed line) (solid red line)
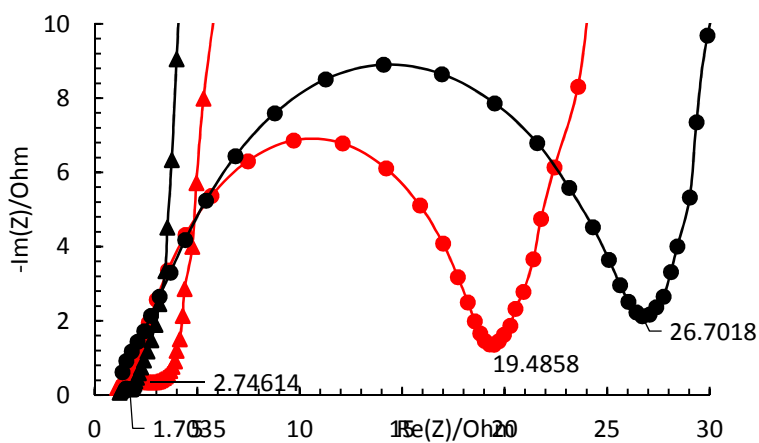
Figure B. 9. EIS of carbon aerogel samples. Converted lignin (green triangles) had a far lower resistance value of 2.7 Ω compared to noncoverted lignin (green circles) at 20 Ω. A blank unconverted aerogel (red circles) had the highest resistance of 26.7 Ω while converted blank aerogel (red triangles) had the lowest resistance at 1.7 Ω.

The resistances of the supercapacitors decreased when lignin was present on the electrodes due to the lignin mixture acting as a more conductive medium for current to flow through due its high KOH content. Resistance slightly increased when converting a blank carbon cloth electrode, most likely due to the process converting the polymers in the carbon cloth into a substance with a higher resistance than the unprocessed carbon cloth. For the carbon aerogel supercapacitors, the resistance of the converted lignin cell may be higher than that of the converted blank cell because of traces of unconverted lignin raising its resistance. The near vertical lines after the dips in the Nyquist Impedance plots are indicative of ideal supercapacitor behavior due to low Rct values for converted lignin on the surface of both carbon cloth and carbon aerogel [246].

Cycle Retention

The carbon aerogel supercapacitor with active lignin retained 54.55% of its current after 5000 cycles, decreasing to 11.44 mA from its initial 20.97 mA. The current remained relatively constant from cycles 5-5000 cycles, keeping a retention rate of 94.26% (**Figure B.10.**). The current density of the fully processed carbon cloth supercapacitor was 3.49 A/g, and that of the fully processed carbon aerogel supercapacitor was 5.95 A/g. The carbon aerogel substrate served as an easier material for electrical current to flow through which could be owed to its graphite like structure, higher measured conductivity, and higher overall quality. The carbon cloth, which was commercially purchased carbonized polymer fibers, lacked the mechanical stability of the aerogel and would fray into small

pieces in the KOH electrolyte. These small fibers could have fouled the dielectric space between electrodes and adversely affected performance.
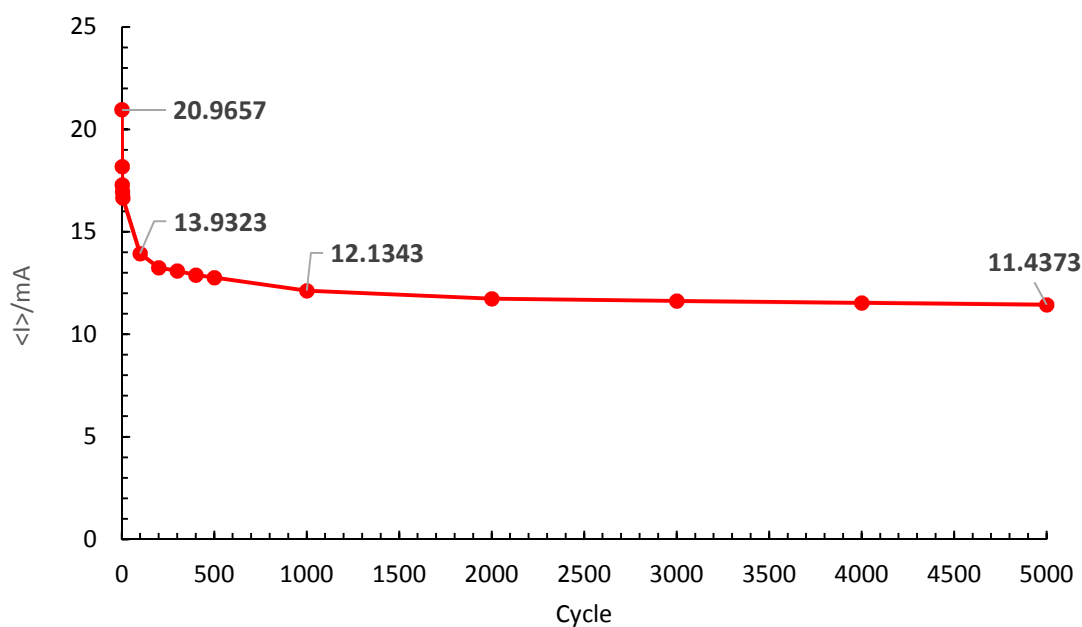
Figure B. 10. Current retention for converted lignin on carbon aerogelr for 5000 cycles

Conclusion

Overall, a new method to synthesize graphene from a base catalyzed lignin slurry directly on the surface of a current collector was created for use in supercapacitors. The electrodes produced in this new method performed well in a 2032-type coin cell setup with a capacitance of 69.80 F g^{-1} for lignin-graphene oxide synthesized on carbon cloth and 119.05 F g^{-1} for lignin-graphene oxide synthesized on carbon aerogel. For the graphene oxide on aerogel, current retention rate remained at 95% of its charge for charge/discharge cycles 5-5000.

APPENDIX C: PUBLICATIONS

1.   Lu, S., **Hummel, M**., Kang, S., Pathak, R., He, W., Qi, X., & Gu, Z. (2021). Density Functional Theory Investigation of the NiO@ Graphene Composite as a Urea Oxidation Catalyst in the Alkaline Electrolyte. *ACS Omega*.

2.   He, W., Chen, K., Pathak, R., **Hummel, M**., Lamsal, B. S., Gu, Z., ... & Zhou, Y. (2021). Achieving High Pseudocapacitance Anode by An In Situ Nanocrystallization Strategy for Ultrastable Sodium-Ion Batteries. *ACS Applied Materials & Interfaces*.

3.   He, W., Chen, K., Pathak, R., **Hummel, M**., Reza, K. M., Ghimire, N., ... & Zhou, Y. (2021). High-mass-loading Sn-based anode boosted by pseudocapacitance for long-life sodium-ion batteries. *Chemical Engineering Journal*, *414*, 128638.

4.   Lu, S., Jia, H., **Hummel, M**., Wu, Y., Wang, K., Qi, X., & Gu, Z. (2021). Two-dimensional conductive phthalocyanine-based metal–organic frameworks for electrochemical nitrite sensing. *RSC Advances*, *11*(8), 4472-4477.

5.   Lu, S., **Hummel, M**., Gu, Z., Wang, Y., Wang, K., Pathak, R., ... & Liu, X. (2021). Highly efficient urea oxidation via nesting nano-nickel oxide in eggshell membrane-derived carbon. *ACS Sustainable Chemistry & Engineering*, *9*(4), 1703-1713.

6.   Lu, S., **Hummel, M**., Wang, X., He, W., Pathak, R., Dong, X., ... & Gu, Z. (2020). Communication—In Situ Electrodeposition of Nickel Phosphide on Ni Foam for Non-Enzymatic Detection of Nitrite. *Journal of the Electrochemical Society*, *167*(14), 146517.

7.   **Hummel, M**., Lu, S., Nelson, Z., Jia, H., Pathak, R., Zhou, Y., & Gu, Z. (2020). Kappa-Carrageenan/Graphene Oxide Carbon Composite Film for Electrochemical Sensing of Dopamine. *Journal of The Electrochemical Society*, *167*(11), 116506.

8.   Lu, S., Gu, Z., **Hummel, M**., Zhou, Y., Wang, K., Xu, B. B., ... & Liu, X. (2020). Nickel oxide immobilized on the carbonized eggshell membrane for electrochemical detection of urea. *Journal of The Electrochemical Society*, *167*(10), 106509.

9.   Rahman, M. T., Maruf, A. A., Faisal, S., Pathak, R., Reza, K. M., Gurung, A., ... & Qiao, Q. (2020). Metallic 1T Phase Tungsten Disulfide Microflowers for Trace Level Detection of Hg2+ Ions. *Advanced Sustainable Systems*, *4*(9), 2000068.

10.   Lu, S., **Hummel, M**., Chen, K., Zhou, Y., Kang, S., & Gu, Z. (2020). Synthesis of Au@ ZIF-8 nanocomposites for enhanced electrochemical detection of dopamine. *Electrochemistry Communications*, *114*, 106715.

11.   Lu, S., **Hummel, M**., Kang, S., & Gu, Z. (2020). Selective voltammetric determination of nitrite using cobalt phthalocyanine modified on multiwalled carbon nanotubes. *Journal of The Electrochemical Society*, *167*(4), 046515.

12.   Nie, M., Du, S., Li, Q., **Hummel, M**., Gu, Z., & Lu, S. (2020). Tungsten carbide as supports for trimetallic AuPdPt electrocatalysts for methanol oxidation. *Journal of The Electrochemical Society*, *167*(4), 044510.

13.   Gu, Y., **Hummel, M**., Muthukumarappan, K., Zhao, Z., & Gu, Z. (2019). Synthesis and characterization of Allyl terpene Maleate Monomer. *Scientific reports*, *9*(1), 1-11.

14.   Cheng, S., **Hummel, M**., Dahal, B., Gu, Z., Kharel, P., & Martínez-Monteagudo, S. I. (2020). A two-step process for the synthesis of sweetening syrup from aqueous lactose. *LWT*, *117*, 108659.

15.   Lu, S., **Hummel, M.**, Gu, Z., Gu, Y., Cen, Z., Wei, L., ... & Yang, C. (2019). Trash to treasure: A novel chemical route to synthesis of NiO/C for hydrogen production. *International Journal of Hydrogen Energy*, *44*(31), 16144-16153.

16.   Pathak, R., Gurung, A., Elbohy, H., Chen, K., Reza, K. M., Bahrami, B., **Hummel, M.,** ... & Qiao, Q. (2018). Self-recovery in Li-metal hybrid lithium-ion batteries via WO 3 reduction. *Nanoscale*, *10*(34), 15956-15966.

BIBLIOGRAPHY

1. Lozano, M.G., et al., *Biosensors for food quality and safety monitoring: fundamentals and applications*, in *Enzymes in food biotechnology*. 2019, Elsevier. p. 691-709.

2. Kissinger, P.T., *Biosensors—a perspective.* Biosensors and Bioelectronics, 2005. **20**(12): p. 2512-2516.

3. Yeom, S.-H., et al., *Nanostructures in biosensor-a review.* Front. Biosci, 2011. **16**: p. 997-1023.

4. Rogers, K.R., *Principles of affinity-based biosensors.* Molecular biotechnology, 2000. **14**(2): p. 109-129.

5. Cammann, K., et al., *Chemical sensors and biosensors—principles and applications.* Angewandte Chemie International Edition in English, 1991. **30**(5): p. 516-539.

6. Lubert, K.H. and K. Kalcher, *History of electroanalytical methods.* Electroanalysis, 2010. **22**(17-18): p. 1937-1946.

7. Stock, J.T. and M.V. Orna, *Electrochemistry, past and present.* Vol. 390. 1989: ACS Publications.

8. Hibbert, D.B., *Introduction to electrochemistry.* 1993: Macmillan International Higher Education.

9. Zoski, C.G., *Handbook of electrochemistry.* 2006: Elsevier.

10. Florea, A., et al., *Electrochemical biosensors as potential diagnostic devices for autoimmune diseases.* Biosensors, 2019. **9**(1): p. 38.

11. Wang, J., *Electrochemical biosensors: towards point-of-care cancer diagnostics.* Biosensors and Bioelectronics, 2006. **21**(10): p. 1887-1892.

12. Mandpe, P., et al., *Glucose oxidase-based biosensor for glucose detection from biological fluids.* Sensor Review, 2020.

13. Matthews, D., et al., *Pen-sized digital 30-second blood glucose meter.* Lancet (British edition), 1987. **1**(8536): p. 778-779.

14. Venkatasetty, H., *Electrochemical multigas sensors for air monitoring assembly.* SAE transactions, 1988: p. 341-346.

15. Attaallah, R., et al., *Nanobiosensors for bioclinical applications: pros and cons*, in *Green Nanoparticles*. 2020, Springer, Cham. p. 117-149.

16.   Jamal, R.B., S. Shipovskov, and E.E. Ferapontova, *Electrochemical immuno-and aptamer-based assays for bacteria: Pros and cons over traditional detection schemes.* Sensors, 2020. **20**(19): p. 5561.

17.   Durgalakshmi, D., S. Rajendran, and A.M. Al-Enizi, *Electrochemistry: Different Materials and Applications: An Overview.* New Technologies for Electrochemical Applications, 2020: p. 1-24.

18.   Hitchman, M.L., et al., *Study of the factors affecting mass transport in electrochemical gas sensors.* Analyst, 1997. **122**(11): p. 1411-1418.

19.   Hutton, L.A., et al., *Examination of the factors affecting the electrochemical performance of oxygen-terminated polycrystalline boron-doped diamond electrodes.* Analytical chemistry, 2013. **85**(15): p. 7230-7240.

20.   Privett, B.J., J.H. Shin, and M.H. Schoenfisch, *Electrochemical sensors.* Analytical chemistry, 2008. **80**(12): p. 4499-4517.

21.   Dees, D., et al., *Alternating current impedance electrochemical modeling of lithium-ion positive electrodes.* Journal of the Electrochemical Society, 2005. **152**(7): p. A1409.

22.   Steinmetz, C.P., *Theory and calculation of alternating current phenomena.* Vol. 4. 1916: McGraw-Hill Book Company, Incorporated.

23.   Tsaparlis, G., *Teaching and learning electrochemistry.* Israel Journal of Chemistry, 2019. **59**(6-7): p. 478-492.

24.   Karaoglanoff, V.Z., *Über Oxydations-und Reduktionsvorgänge bei der Elektrolyse von Eisensalzlösungen.* Zeitschrift für Elektrochemie und angewandte physikalische Chemie, 1906. **12**(1): p. 5-16.

25.   Zutshi, K., *Introduction to polarography and allied techniques.* 2006: New Age International.

26.   Ngamchuea, K., et al., *Planar diffusion to macro disc electrodes—what electrode size is required for the Cottrell and Randles-Sevcik equations to apply quantitatively?* Journal of Solid State Electrochemistry, 2014. **18**(12): p. 3251-3257.

27.   Neghmouche, N., A. Khelef, and T. Lanez, *Electrochemistry characterization of ferrocene/ferricenium redox couple at glassycarbon electrode.* Journal of Fundamental and Applied Sciences, 2009. **1**(2): p. 23-30.

28.   Neghmouche, N. and T. Lanez, *Calculation of electrochemical parameters starting from the polarization curves of ferrocene at glassy carbon electrode.* International Letters of Chemistry, Physics and Astronomy, 2013. **4**: p. 37-45.

29.   Leftheriotis, G., S. Papaefthimiou, and P. Yianoulis, *Dependence of the estimated diffusion coefficient of LixWO3 films on the scan rate of cyclic voltammetry experiments.* Solid State Ionics, 2007. **178**(3-4): p. 259-263.

30.   Eftekhari, A., *Comments on "Li diffusion in LiNi 0.5 Mn 0.5 O 2 thin film electrodes prepared by pulsed laser deposition" by Xia et al.* Electrochimica Acta, 2010. **55**(9): p. 3434.

31.   Kulesza, P.J. and J.A. Cox, *Solid-State Voltammetry—Analytical Prospects.* Electroanalysis: An International Journal Devoted to Fundamental and Practical Aspects of Electroanalysis, 1998. **10**(2): p. 73-80.

32.   Hammond, J.L., et al., *Electrochemical biosensors and nanobiosensors.* Essays in biochemistry, 2016. **60**(1): p. 69-80.

33.   Rho, S., et al., *Electrochemical DNA biosensors based on thin gold films sputtered on capacitive nanoporous niobium oxide.* Biosensors and bioelectronics, 2008. **23**(6): p. 852-856.

34.   Cesewski, E. and B.N. Johnson, *Electrochemical biosensors for pathogen detection.* Biosensors and Bioelectronics, 2020. **159**: p. 112214.

35.   Berggren, C., B. Bjarnason, and G. Johansson, *Capacitive biosensors.* Electroanalysis: An International Journal Devoted to Fundamental and Practical Aspects of Electroanalysis, 2001. **13**(3): p. 173-180.

36.   Guan, J.-G., Y.-Q. Miao, and Q.-J. Zhang, *Impedimetric biosensors.* Journal of bioscience and bioengineering, 2004. **97**(4): p. 219-226.

37.   Riquelme, M.V., et al., *Optimizing blocking of nonspecific bacterial attachment to impedimetric biosensors.* Sensing and bio-sensing research, 2016. **8**: p. 47-54.

38.   Lu, Y., et al., *A review of the identification and detection of heavy metal ions in the environment by voltammetry.* Talanta, 2018. **178**: p. 324-338.

39.   Di, J. and F. Zhang, *Voltammetry determination of trace manganese with pretreatment glassy carbon electrode by linear sweep voltammetry.* Talanta, 2003. **60**(1): p. 31-36.

40.   Yan, D., et al., *Theory of linear sweep voltammetry with diffuse charge: Unsupported electrolytes, thin films, and leaky membranes.* Physical Review E, 2017. **95**(3): p. 033303.

41.   Chai, H., et al., *Validity and Reproducibility of Various Linear Sweep Voltammetry Tests of Anode and Cathode Electrodes in Microbial Electrolysis Cells.* 2020.

42.   Appel, A.M. and M.L. Helm, *Determining the overpotential for a molecular electrocatalyst.* 2014, ACS Publications.

43. Bard, A.J. and L.R. Faulkner, *Fundamentals and applications.* Electrochemical methods, 2001. **2**(482): p. 580-632.

44. Tsai, W., et al., *Characterization and adsorption properties of eggshells and eggshell membrane.* Bioresource technology, 2006. **97**(3): p. 488-493.

45. Liu, Y., et al., *Hierarchical CuO nanorod arrays in situ generated on three-dimensional copper foam via cyclic voltammetry oxidation for high-performance supercapacitors.* Journal of Materials Chemistry A, 2018. **6**(22): p. 10474-10483.

46. Espinoza, E.M., et al., *Practical aspects of cyclic voltammetry: How to estimate reduction potentials when irreversibility prevails.* Journal of The Electrochemical Society, 2019. **166**(5): p. H3175.

47. Osterbauer, K.J., et al., *Effects of nitrite and erythorbate on Clostridium perfringens growth during extended cooling of cured ham.* Journal of food protection, 2017. **80**(10): p. 1697-1704.

48. Dhara, K. and R.M. Debiprosad, *Review on nanomaterials-enabled electrochemical sensors for ascorbic acid detection.* Analytical biochemistry, 2019. **586**: p. 113415.

49. Wu, D., et al., *Sensitive electrochemical sensor for simultaneous determination of dopamine, ascorbic acid, and uric acid enhanced by amino-group functionalized mesoporous Fe3O4@ graphene sheets.* Electrochimica Acta, 2014. **116**: p. 244-249.

50. Bagheri, H., et al., *A novel electrochemical platform for sensitive and simultaneous determination of dopamine, uric acid and ascorbic acid based on Fe3O4SnO2Gr ternary nanocomposite.* Microchemical Journal, 2017. **131**: p. 120-129.

51. Qi, S., et al., *Determination of ascorbic acid, dopamine, and uric acid by a novel electrochemical sensor based on pristine graphene.* Electrochimica Acta, 2015. **161**: p. 395-402.

52. Ates, M., *A review study of (bio) sensor systems based on conducting polymers.* Materials Science and Engineering: C, 2013. **33**(4): p. 1853-1859.

53. Shao, Y., et al., *Graphene based electrochemical sensors and biosensors: a review.* Electroanalysis: An International Journal Devoted to Fundamental and Practical Aspects of Electroanalysis, 2010. **22**(10): p. 1027-1036.

54. Hoyer, B. and N. Jensen, *Use of sodium dodecyl sulfate for suppression of electrode fouling in the voltammetric detection of biologically relevant compounds.* Electroanalysis: An International Journal Devoted to Fundamental and Practical Aspects of Electroanalysis, 2005. **17**(22): p. 2037-2042.

55. Borrill, A.J., N.E. Reily, and J.V. Macpherson, *Addressing the practicalities of anodic stripping voltammetry for heavy metal detection: a tutorial review.* Analyst, 2019. **144**(23): p. 6834-6849.

56. Pizarro, J., et al., *Inexpensive and green electrochemical sensor for the determination of Cd (II) and Pb (II) by square wave anodic stripping voltammetry in bivalve mollusks.* Food chemistry, 2020. **321**: p. 126682.

57. Zhang, Z., et al., *Electrochemical enzyme biosensor for carnitine detection based on cathodic stripping voltammetry.* Sensors and Actuators B: Chemical, 2020. **321**: p. 128473.

58. Albishri, H.M. and D. Abd El-Hady, *Hyphenation of enzyme/graphene oxide-ionic liquid/glassy carbon biosensors with anodic differential pulse stripping voltammetry for reliable determination of choline and acetylcholine in human serum.* Talanta, 2019. **200**: p. 107-114.

59. Glavan, A.C., et al., *Folding analytical devices for electrochemical ELISA in hydrophobic RH paper.* Analytical chemistry, 2014. **86**(24): p. 11999-12007.

60. Arya, S.K. and P. Estrela, *Electrochemical ELISA-based platform for bladder cancer protein biomarker detection in urine.* Biosensors and Bioelectronics, 2018. **117**: p. 620-627.

61. Singh, B., E. Flampouri, and E. Dempsey, *Electrochemical enzyme-linked immunosorbent assay (e-ELISA) for parasitic nematode Ostertagia ostertagi (brown stomach worm) infections in dairy cattle.* Analyst, 2019. **144**(19): p. 5748-5754.

62. Juang, D.S., et al., *Proton-ELISA: Electrochemical immunoassay on a dual-gated ISFET array.* Biosensors and Bioelectronics, 2018. **117**: p. 175-182.

63. Hwang, D.-W., et al., *Recent advances in electrochemical non-enzymatic glucose sensors–a review.* Analytica chimica acta, 2018. **1033**: p. 1-34.

64. Rhouati, A., M. Majdinasab, and A. Hayat, *A perspective on non-enzymatic electrochemical nanosensors for direct detection of pesticides.* Current Opinion in Electrochemistry, 2018. **11**: p. 12-18.

65. Han, D., et al., *Simultaneous determination of ascorbic acid, dopamine and uric acid with chitosan‐graphene modified electrode.* Electroanalysis, 2010. **22**(17-18): p. 2001-2008.

66. Xiao, T., et al., *In vivo analysis with electrochemical sensors and biosensors.* Analytical chemistry, 2017. **89**(1): p. 300-313.

67. Lee, J., et al., *Metal–organic framework materials as catalysts.* Chemical Society Reviews, 2009. **38**(5): p. 1450-1459.

68. Li, H., et al., *Design and synthesis of an exceptionally stable and highly porous metal-organic framework.* nature, 1999. **402**(6759): p. 276-279.

69. Zhang, X., et al., *Structural and functional components of the skate sensory organ ampullae of lorenzini.* ACS chemical biology, 2018. **13**(6): p. 1677-1685.

70. Horkay, F., J.F. Douglas, and S.R. Raghavan, *Rheological Properties of Cartilage Glycosaminoglycans and Proteoglycans.* Macromolecules, 2021. **54**(5): p. 2316-2324.

71. Bui, V.T., et al., *Rheology and microstructure of mixtures of iota and kappa-carrageenan.* Food hydrocolloids, 2019. **89**: p. 180-187.

72. Pachiadaki, M.G., et al., *Major role of nitrite-oxidizing bacteria in dark ocean carbon fixation.* Science, 2017. **358**(6366): p. 1046-1051.

73. Timmons, A.J. and M.D. Symes, *Converting between the oxides of nitrogen using metal–ligand coordination complexes.* Chemical Society Reviews, 2015. **44**(19): p. 6708-6722.

74. Imlay, J.A., *Common mechanisms of bacterial metal homeostasis.* 2021.

75. Oku, K., et al., *Interaction between trehalose and alkaline-earth metal ions.* Bioscience, biotechnology, and biochemistry, 2005. **69**(1): p. 7-12.

76. Liyaghatdar, Z., et al., *Trehalose radial networks protect Renilla luciferase helical layers against thermal inactivation.* International journal of biological macromolecules, 2017. **105**: p. 66-73.

77. Smirnova, D., et al., *Firefly Luciferase Bioluminescence as a Tool for Searching Magnetic Isotope Effects in ATP-Dependent Enzyme Reactions.* Moscow University Chemistry Bulletin, 2018. **73**(4): p. 158-165.

78. Monzani, E., et al., *Dopamine, Oxidative Stress and Protein–Quinone Modifications in Parkinson's and Other Neurodegenerative Diseases.* Angewandte Chemie International Edition, 2019. **58**(20): p. 6512-6527.

79. Volkow, N.D., R.A. Wise, and R. Baler, *The dopamine motive system: implications for drug and food addiction.* Nature Reviews Neuroscience, 2017. **18**(12): p. 741.

80. Palanisamy, S., S. Ku, and S.-M. Chen, *Dopamine sensor based on a glassy carbon electrode modified with a reduced graphene oxide and palladium nanoparticles composite.* Microchimica Acta, 2013. **180**(11-12): p. 1037-1042.

81. Selvolini, G., C. Lazzarini, and G. Marrazza, *Electrochemical Nanocomposite Single-Use Sensor for Dopamine Detection.* Sensors, 2019. **19**(14): p. 3097.

82. Moon, J.-M., et al., *Conducting polymer-based electrochemical biosensors for neurotransmitters: A review.* Biosensors and Bioelectronics, 2018. **102**: p. 540-552.

83. Sajid, M., et al., *Chemically modified electrodes for electrochemical detection of dopamine in the presence of uric acid and ascorbic acid: a review.* TrAC Trends in Analytical Chemistry, 2016. **76**: p. 15-29.

84. Syedmoradi, L., et al., *Point of care testing: The impact of nanotechnology.* Biosensors and Bioelectronics, 2017. **87**: p. 373-387.

85. Zarei, M., *Portable biosensing devices for point-of-care diagnostics: Recent developments and applications.* TrAC Trends in Analytical Chemistry, 2017. **91**: p. 26-41.

86. Phung, V.-D., et al., *Reliable and quantitative SERS detection of dopamine levels in human blood plasma using a plasmonic Au/Ag nanocluster substrate.* Nanoscale, 2018. **10**(47): p. 22493-22503.

87. Zhao, J., et al., *Graphene quantum dots as effective probes for label-free fluorescence detection of dopamine.* Sensors and Actuators B: Chemical, 2016. **223**: p. 246-251.

88. Caetano, F.R., et al., *Gold nanoparticles supported on multi-walled carbon nanotubes produced by biphasic modified method and dopamine sensing application.* Sensors and Actuators B: Chemical, 2017. **243**: p. 43-50.

89. Mobarak, N., et al., *Chemical interaction and conductivity of carboxymethyl κ-carrageenan based green polymer electrolyte.* Solid state ionics, 2012. **224**: p. 51-57.

90. Huang, Y., et al., *Flexible quasi-solid-state zinc ion batteries enabled by highly conductive carrageenan bio-polymer electrolyte.* RSC Advances, 2019. **9**(29): p. 16313-16319.

91. Liu, J., et al., *Review for carrageenan-based pharmaceutical biomaterials: favourable physical features versus adverse biological effects.* Carbohydrate Polymers, 2015. **121**: p. 27-36.

92. Geonzon, L.C., R.G. Bacabac, and S. Matsukawa, *Network structure and gelation mechanism of kappa and iota carrageenan elucidated by multiple particle tracking.* Food hydrocolloids, 2019. **92**: p. 173-180.

93. Jol, C.N., et al., *A novel high-performance anion-exchange chromatographic method for the analysis of carrageenans and agars containing 3, 6-anhydrogalactose.* Analytical Biochemistry, 1999. **268**(2): p. 213-222.

94.   Mobarak, N.N., et al. *Chemical Interaction, Conductivity and Thermal Properties of kappa carrageenan based Polymer Electrolytes*. in *Advanced Materials Research*. 2015. Trans Tech Publ.

95.   Stanfa, L.C., A.F. Sullivan, and A.H. Dickenson, *Alterations in neuronal excitability and the potency of spinal mu, delta and kappa opioids after carrageenan-induced inflammation*. Pain, 1992. **50**(3): p. 345-354.

96.   Harris-Bozer, A.L. and Y.B. Peng, *Inflammatory pain by carrageenan recruits low-frequency local field potential changes in the anterior cingulate cortex*. Neuroscience letters, 2016. **632**: p. 8-14.

97.   Gao, X., et al., *Effects of intraplantar injection of carrageenan on central dopamine release*. Brain research bulletin, 2001. **54**(4): p. 391-394.

98.   Coffeen, U., et al., *Inflammatory nociception diminishes dopamine release and increases dopamine D2 receptor mRNA in the rat's insular cortex*. Molecular pain, 2010. **6**(1): p. 75.

99.   Alam, M.B., et al., *Protopine attenuates inflammation stimulated by carrageenan and LPS via the MAPK/NF-κB pathway*. Food and Chemical Toxicology, 2019: p. 110583.

100.   Kovalska, E., et al., *Multi-layer graphene as a selective detector for future lung cancer biosensing platforms*. Nanoscale, 2019. **11**(5): p. 2476-2483.

101.   Goldsmith, B.R., et al., *Digital biosensing by foundry-fabricated graphene sensors*. Scientific reports, 2019. **9**(1): p. 434.

102.   Lee, J.-H., S.-J. Park, and J.-W. Choi, *Electrical property of graphene and its application to electrochemical biosensing*. Nanomaterials, 2019. **9**(2): p. 297.

103.   Justino, C.I., et al., *Graphene based sensors and biosensors*. TrAC Trends in Analytical Chemistry, 2017. **91**: p. 53-66.

104.   Vashist, S.K. and J.H. Luong, *Recent advances in electrochemical biosensing schemes using graphene and graphene-based nanocomposites*. Carbon, 2015. **84**: p. 519-550.

105.   Jin, H., et al., *A facile method for preparing nitrogen-doped graphene and its application in supercapacitors*. Journal of power sources, 2015. **273**: p. 1156-1162.

106.   Li, X., L. Colombo, and R.S. Ruoff, *Synthesis of graphene films on copper foils by chemical vapor deposition*. Advanced Materials, 2016. **28**(29): p. 6247-6252.

107.   Feng, X., et al., *Three-dimensional nitrogen-doped graphene as an ultrasensitive electrochemical sensor for the detection of dopamine*. Nanoscale, 2015. **7**(6): p. 2427-2432.

108. Sajid, M., N. Baig, and K. Alhooshani, *Chemically modified electrodes for electrochemical detection of dopamine: Challenges and opportunities.* TrAC Trends in Analytical Chemistry, 2019. **118**: p. 368-385.

109. Kozlowska, J., K. Pauter, and A. Sionkowska, *Carrageenan-based hydrogels: Effect of sorbitol and glycerin on the stability, swelling and mechanical properties.* Polymer Testing, 2018. **67**: p. 7-11.

110. Derkach, S., et al., *Molecular structure and properties of κ-carrageenan-gelatin gels.* Carbohydrate polymers, 2018. **197**: p. 66-74.

111. Sahoo, P., et al., *Chitosan complexed carboxymethylated iota-carrageenan oral insulin particles: Stability, permeability and in vivo evaluation.* Materials Today Communications, 2019. **20**: p. 100557.

112. Lu, S., et al., *Selective voltammetric determination of nitrite using cobalt phthalocyanine modified on multiwalled carbon nanotubes.* Journal of The Electrochemical Society, 2020. **167**(4): p. 046515.

113. Stobinski, L., et al., *Graphene oxide and reduced graphene oxide studied by the XRD, TEM and electron spectroscopy methods.* Journal of Electron Spectroscopy and Related Phenomena, 2014. **195**: p. 145-154.

114. Prasad, K., Y. Kaneko, and J.i. Kadokawa, *Novel gelling systems of κ-, ι-and λ-carrageenans and their composite gels with cellulose using ionic liquid.* Macromolecular bioscience, 2009. **9**(4): p. 376-382.

115. Chen, W., et al., *Preparation of lignin-based porous carbon with hierarchical oxygen-enriched structure for high-performance supercapacitors.* Journal of colloid and interface science, 2019. **540**: p. 524-534.

116. Balqis, A.I., et al., *Effects of plasticizers on the physicochemical properties of kappa-carrageenan films extracted from Eucheuma cottonii.* International journal of biological macromolecules, 2017. **103**: p. 721-732.

117. Jiang, J., et al., *In-situ fabrication of graphene-nickel matrix composites.* Materials Letters, 2018. **220**: p. 178-181.

118. Wu, J., et al., *Investigation of the microstructures of graphene quantum dots (GQDs) by surface-enhanced Raman spectroscopy.* Nanomaterials, 2018. **8**(10): p. 864.

119. Wang, K., et al., *Low-temperature plasma exfoliated n-doped graphene for symmetrical electrode supercapacitors.* Nano Energy, 2017. **31**: p. 486-494.

120. Lim, Y.-M., et al., *Preparation and biocompatibility study of gelatin/kappa-carrageenan scaffolds.* Macromolecular research, 2010. **18**(1): p. 29-34.

121. McKim, J.M., et al., *Clarifying the confusion between poligeenan, degraded carrageenan, and carrageenan: A review of the chemistry, nomenclature, and in vivo toxicology by the oral route.* Critical reviews in food science and nutrition, 2019. **59**(19): p. 3054-3073.

122. Hrapovic, S., et al., *Preparation of polymer–carbon nanotube composite materials and their applications for enzyme entrapment.* Analytical letters, 2008. **41**(2): p. 278-288.

123. Harreither, W., et al., *Carbon nanotube fiber microelectrodes show a higher resistance to dopamine fouling.* Analytical chemistry, 2013. **85**(15): p. 7447-7453.

124. Lu, S., et al., *Synthesis of Au@ ZIF-8 nanocomposites for enhanced electrochemical detection of dopamine.* Electrochemistry Communications, 2020: p. 106715.

125. Roychoudhury, A., S. Basu, and S.K. Jha, *Dopamine biosensor based on surface functionalized nanostructured nickel oxide platform.* Biosensors and Bioelectronics, 2016. **84**: p. 72-81.

126. Shahbazi, M., et al., *Kinetic study of κ-carrageenan degradation and its impact on mechanical and structural properties of chitosan/κ-carrageenan film.* Carbohydrate polymers, 2016. **142**: p. 167-176.

127. Ozoemena, O.C., et al., *Electrochemical Sensing of Dopamine Using Onion-like Carbons and Their Carbon Nanofiber Composites.* Electrocatalysis, 2019: p. 1-11.

128. Orzari, L.O., et al., *A novel disposable self-adhesive inked paper device for electrochemical sensing of dopamine and serotonin neurotransmitters and biosensing of glucose.* Biosensors and Bioelectronics, 2019. **138**: p. 111310.

129. Awad, G.E., et al., *Functionalized κ-carrageenan/hyperbranched poly (amidoamine) for protease immobilization: Thermodynamics and stability studies.* International Journal of Biological Macromolecules, 2020.

130. Priya, T., et al., *A novel voltammetric sensor for the simultaneous detection of Cd2+ and Pb2+ using graphene oxide/κ-carrageenan/l-cysteine nanocomposite.* Carbohydrate polymers, 2018. **182**: p. 199-206.

131. Parvizishad, M., et al., *A review of adverse effects and benefits of nitrate and nitrite in drinking water and food on human health.* Health Scope, 2017. **6**(3).

132. Jackson, J.K., et al., *The role of inorganic nitrate and nitrite in cardiovascular disease risk factors: a systematic review and meta-analysis of human evidence.* Nutrition reviews, 2018. **76**(5): p. 348-371.

133. Ensafi, A.A. and M. Amini, *A highly selective optical sensor for catalytic determination of ultra-trace amounts of nitrite in water and foods based on brilliant*

cresyl blue as a sensing reagent. Sensors and Actuators B: Chemical, 2010. **147**(1): p. 61-66.

134. Jobgen, W.S., et al., *Analysis of nitrite and nitrate in biological samples using high-performance liquid chromatography.* Journal of Chromatography B, 2007. **851**(1-2): p. 71-82.

135. Zhou, L., et al., *An amperometric sensor based on ionic liquid and carbon nanotube modified composite electrode for the determination of nitrite in milk.* Sensors and Actuators B: Chemical, 2013. **181**: p. 65-70.

136. Lu, S., et al., *Communication—In Situ Electrodeposition of Nickel Phosphide on Ni Foam for Non-Enzymatic Detection of Nitrite.* Journal of the Electrochemical Society, 2020. **167**(14): p. 146517.

137. Lutfi Yola, M. and N. Atar, *A review: molecularly imprinted electrochemical sensors for determination of biomolecules/drug.* Current Analytical Chemistry, 2017. **13**(1): p. 13-17.

138. Li, X., J. Ping, and Y. Ying, *Recent developments in carbon nanomaterial-enabled electrochemical sensors for nitrite detection.* TrAC Trends in Analytical Chemistry, 2019. **113**: p. 1-12.

139. Wierzbicka, E., *Novel methods of nitrate and nitrite determination-a review.* Journal of Elementology, 2020. **25**(1).

140. Alam, M.S., et al., *Enhanced electrocatalytic effects of Pd particles immobilized on GC surface on the nitrite oxidation reactions.* Journal of Electroanalytical Chemistry, 2019. **839**: p. 1-8.

141. Zhao, Z., et al., *Synthesis and electrochemical properties of Co3O4-rGO/CNTs composites towards highly sensitive nitrite detection.* Applied Surface Science, 2019. **485**: p. 274-282.

142. Kung, C.-W., et al., *Porphyrin-based metal–organic framework thin films for electrochemical nitrite detection.* Electrochemistry Communications, 2015. **58**: p. 51-56.

143. Wendler, F., P. Aurosmit, and O. Kanoun, *CNT-enhanced carbon electrode for nitrite detection and water analysis*, in *Impedance Spectroscopy*. 2018, De Gruyter. p. 143-150.

144. Yan, M., et al., *Research progress on nitrite electrochemical sensor.* Chinese Journal of Analytical Chemistry, 2018. **46**(2): p. 147-155.

145. Liu, L., et al., *Enhanced His@ AuNCs oxidase-like activity by reduced graphene oxide and its application for colorimetric and electrochemical detection of nitrite.* Analytical and bioanalytical chemistry, 2019. **411**(10): p. 2189-2200.

146. Jacob, J., et al., *Oxidation kinetics and inverse isotope effect of marine nitrite-oxidizing isolates.* Aquatic Microbial Ecology, 2017. **80**(3): p. 289-300.

147. Taylor, A.E., D.D. Myrold, and P.J. Bottomley, *Temperature affects the kinetics of nitrite oxidation and nitrification coupling in four agricultural soils.* Soil Biology and Biochemistry, 2019. **136**: p. 107523.

148. Geng, P., et al., *Transition metal sulfides based on graphene for electrochemical energy storage.* Advanced Energy Materials, 2018. **8**(15): p. 1703259.

149. Landers, A.T., et al., *The predominance of hydrogen evolution on transition metal sulfides and phosphides under CO2 reduction conditions: an experimental and theoretical study.* ACS Energy Letters, 2018. **3**(6): p. 1450-1457.

150. Cao, F., et al., *One-pot synthesis of flowerlike Ni 7 S 6 and its application in selective hydrogenation of chloronitrobenzene.* Journal of Materials Chemistry, 2010. **20**(6): p. 1078-1085.

151. Wu, W., et al., *Sensing nitrite with a glassy carbon electrode modified with a three-dimensional network consisting of Ni 7 S 6 and multi-walled carbon nanotubes.* Microchimica Acta, 2016. **183**(12): p. 3159-3166.

152. Kim, J.-S., et al., *The discharge properties of Na/Ni3S2 cell at ambient temperature.* Journal of Power Sources, 2008. **178**(2): p. 852-856.

153. Lelevic, A. and F.C. Walsh, *Electrodeposition of NiP alloy coatings: a review.* Surface and Coatings Technology, 2019. **369**: p. 198-220.

154. Yuan, X., et al., *Preparation of amorphous-nanocrystalline composite structured Ni–P electrodeposits.* Surface and Coatings Technology, 2007. **202**(2): p. 294-300.

155. Lin, C., et al., *Electrodeposition of nickel-phosphorus alloy from sulfamate baths with improved current efficiency.* Journal of The Electrochemical Society, 2006. **153**(6): p. C387.

156. Shi, L., C. Sun, and W. Liu, *Electrodeposited nickel–cobalt composite coating containing MoS2.* Applied Surface Science, 2008. **254**(21): p. 6880-6885.

157. Lu, Z., et al., *Stable ultrahigh specific capacitance of NiO nanorod arrays.* Nano research, 2011. **4**(7): p. 658-665.

158. Wilkin, R.T. and D.A. Rogers, *Nickel sulfide formation at low temperature: initial precipitates, solubility and transformation products.* Environmental Chemistry, 2010. **7**(6): p. 514-523.

159. Wang, J., et al., *Nanostructured nickel sulfide synthesized via a polyol route as a cathode material for the rechargeable lithium battery.* Electrochemistry communications, 2007. **9**(8): p. 1877-1880.

160. Fazli, Y., et al., *Electrochemical synthesis and structure characterization of nickel sulfide nanoparticles.* Materials science in semiconductor processing, 2014. **27**: p. 362-367.

161. Huang, S., et al., *The composition of nanoparticulate nickel sulfide.* Chemical Geology, 2010. **277**(3-4): p. 207-213.

162. Gu, H., X.d. Su, and K.P. Loh, *Electrochemical impedance sensing of DNA hybridization on conducting polymer film-modified diamond.* The Journal of Physical Chemistry B, 2005. **109**(28): p. 13611-13618.

163. Yeo, B.S. and A.T. Bell, *In situ Raman study of nickel oxide and gold-supported nickel oxide catalysts for the electrochemical evolution of oxygen.* The Journal of Physical Chemistry C, 2012. **116**(15): p. 8394-8400.

164. Trasatti, S. and O. Petrii, *Real surface area measurements in electrochemistry.* Pure Appl. Chem, 1991. **63**(5): p. 711-734.

165. Guidelli, R., F. Pergola, and G. Raspi, *Voltammetric behavior of nitrite ion on platinum in neutral and weakly acidic media.* Analytical chemistry, 1972. **44**(4): p. 745-755.

166. Li, G., et al., *Recent developments on graphene-based electrochemical sensors toward nitrite.* Journal of the Electrochemical Society, 2019. **166**(12): p. B881.

167. Zhai, M., et al., *Solvothermal synthesis of flower-like structure Cu-Mn bimetallic sulfide on Ni-foam for high-performance symmetric supercapacitors.* International Journal of Hydrogen Energy, 2019. **44**(26): p. 13456-13465.

168. Wu, K., et al., *Cobalt and nickel bimetallic sulfide nanoparticles immobilized on montmorillonite demonstrating peroxidase-like activity for H 2 O 2 detection.* New Journal of Chemistry, 2018. **42**(23): p. 18749-18758.

169. Li, S.-S., et al., *Simple synthesis of worm-like Au–Pd nanostructures supported on reduced graphene oxide for highly sensitive detection of nitrite.* Sensors and Actuators B: Chemical, 2015. **208**: p. 468-474.

170. Wang, Z., et al., *Synthesis of crystalline silver nanoplates and their application for detection of nitrite in foods.* Journal of Electroanalytical Chemistry, 2012. **664**: p. 135-138.

171. Feng, J.-J., et al., *One-pot hydrothermal synthesis of uniform β-MnO2 nanorods for nitrite sensing.* Journal of colloid and interface science, 2011. **359**(1): p. 1-8.

172. Kuss, S., H.M. Amin, and R.G. Compton, *Electrochemical detection of pathogenic bacteria—recent strategies, advances and challenges.* Chemistry–An Asian Journal, 2018. **13**(19): p. 2758-2769.

173. da Silva Neves, M.M.P., et al., *Future trends in the market for electrochemical biosensing.* Current Opinion in Electrochemistry, 2018. **10**: p. 107-111.

174. Felix, F.S. and L. Angnes, *Electrochemical immunosensors–a powerful tool for analytical applications.* Biosensors and Bioelectronics, 2018. **102**: p. 470-478.

175. Sun, A.C. and D.A. Hall, *Point‐of‐care smartphone‐based electrochemical biosensing.* Electroanalysis, 2019. **31**(1): p. 2-16.

176. Vanherp, L., et al., *Trehalose as quantitative biomarker for in vivo diagnosis and treatment follow-up in cryptococcomas.* Translational Research, 2020.

177. Yee, E.H., et al., *Detection of biomarkers of periodontal disease in human saliva using stabilized, vertical flow immunoassays.* ACS sensors, 2017. **2**(11): p. 1589-1593.

178. Kus-Liśkiewicz, M., A. Górka, and M. Gonchar, *Simple assay of trehalose in industrial yeast.* Food chemistry, 2014. **158**: p. 335-339.

179. Elbein, A.D., et al., *New insights on trehalose: a multifunctional molecule.* Glycobiology, 2003. **13**(4): p. 17R-27R.

180. Iordachescu, M. and R. Imai, *Trehalose biosynthesis in response to abiotic stresses.* Journal of integrative plant biology, 2008. **50**(10): p. 1223-1229.

181. Thammahong, A., et al., *Central role of the trehalose biosynthesis pathway in the pathogenesis of human fungal infections: opportunities and challenges for therapeutic development.* Microbiology and Molecular Biology Reviews, 2017. **81**(2).

182. Vanaporn, M. and R.W. Titball, *Trehalose and bacterial virulence.* Virulence, 2020. **11**(1): p. 1192-1202.

183. Actor, J.K., *Trehalose dimycolate (cord factor) as a contributing factor to tuberculosis pathogenesis*, in *Tuberculosis Host-Pathogen Interactions*. 2019, Springer. p. 43-61.

184. Kamariza, M., et al., *Rapid detection of Mycobacterium tuberculosis in sputum with a solvatochromic trehalose probe.* Science translational medicine, 2018. **10**(430): p. eaam6310.

185. Luo, X.-T., et al., *Sensitive analysis of trehalose-6-phosphate and related sugar phosphates in plant tissues by chemical derivatization combined with hydrophilic interaction liquid chromatography–tandem mass spectrometry.* Journal of Chromatography A, 2019. **1592**: p. 82-90.

186. Datta, M. and D. Desai, *Trehalose: An Anonymity Turns Into Necessity.* High Value Fermentation Products: Human Health, 2019. **1**: p. 309-321.

187. Collins, J., H. Danhof, and R.A. Britton, *The role of trehalose in the global spread of epidemic Clostridium difficile.* Gut Microbes, 2019. **10**(2): p. 204-209.

188. Hallsworth, J.E. and N. Magan, *A rapid HPLC protocol for detection of polyols and trehalose.* Journal of microbiological methods, 1997. **29**(1): p. 7-13.

189. Hayner, G.A., S. Khetan, and M.G. Paulick, *Quantification of the disaccharide trehalose from biological samples: a comparison of analytical methods.* ACS omega, 2017. **2**(9): p. 5813-5823.

190. Tunnacliffe, A., A.G.a. de Castro, and M. Manzanera, *Anhydrobiotic engineering of bacterial and mammalian cells: is intracellular trehalose sufficient?* Cryobiology, 2001. **43**(2): p. 124-132.

191. Zhang, Q. and T. Yan, *Correlation of intracellular trehalose concentration with desiccation resistance of soil Escherichia coli populations.* Applied and environmental microbiology, 2012. **78**(20): p. 7407-7413.

192. Kushwaha, S., et al., *Cloning, expression, purification and kinetics of trehalose-6-phosphate phosphatase of filarial parasite Brugia malayi.* Acta tropica, 2011. **119**(2-3): p. 151-159.

193. Caner, S., et al., *The structure of the Mycobacterium smegmatis trehalose synthase reveals an unusual active site configuration and acarbose-binding mode.* Glycobiology, 2013. **23**(9): p. 1075-1083.

194. Cross, M., et al., *Probing function and structure of trehalose‑6‑phosphate phosphatases from pathogenic organisms suggests distinct molecular groupings.* The FASEB Journal, 2017. **31**(3): p. 920-926.

195. Fujimoto, T., et al., *Crystal Structure of α, α‑Trehalose−Calcium Chloride Monohydrate Complex.* Journal of carbohydrate chemistry, 2006. **25**(7): p. 521-532.

196. Frisch, M.J.T., G. W.; Schlegel, H. B.; Scuseria, G. E.; Robb, M. A.; Cheeseman, J. R.; Scalmani, G.; Barone, V.; Mennucci, B.; Petersson, G. A.; et al., *Gaussian, Inc.* 2009.

197. Janczak, J. and R. Kubiak, *X-ray single crystal investigations of magnesium phthalocyanine. The 4+ 1 coordination of the Mg ion and its consequence.* Polyhedron, 2001. **20**(24-25): p. 2901-2909.

198. Zhang, J., et al., *Spectroscopic and kinetic studies of photochemical reaction of magnesium tetraphenylporphyrin with oxygen.* The Journal of Physical Chemistry A, 2009. **113**(18): p. 5367-5374.

199. Kinzhybalo, V., R. Kubiak, and J. Janczak, *Reactivity of the magnesium phthalocyanine in dry 3, 5-lutidine, in 3, 5-lutidine/DMSO and in 3, 5-lutidine/acetylacetone systems.* Polyhedron, 2016. **115**: p. 142-154.

200. Mei, B.-A., et al., *Physical interpretations of Nyquist plots for EDLC electrodes and devices.* The Journal of Physical Chemistry C, 2018. **122**(1): p. 194-206.

201. El-Mallah, N.M., A.-M.M. Ahmed, and L.F. Gado, *Electrodeposition of Copper in Presence of Carbohydrates.* Journal of Dispersion Science and Technology, 2010. **31**(11): p. 1579-1590.

202. Abb, S., et al., *Polymorphism in carbohydrate self-assembly at surfaces: STM imaging and theoretical modelling of trehalose on Cu (100).* RSC advances, 2019. **9**(61): p. 35813-35819.

203. Segura, R., et al., *Development of electrochemical sensors for the determination of selenium using gold nanoparticles modified electrodes.* Sensors and Actuators B: Chemical, 2015. **220**: p. 263-269.

204. Wu, Y., et al., *Establishing a synergetic carbon utilization mechanism for non-catabolic use of glucose in microbial synthesis of trehalose.* Metabolic engineering, 2017. **39**: p. 1-8.

205. Kandror, O., A. DeLeon, and A.L. Goldberg, *Trehalose synthesis is induced upon exposure of Escherichia coli to cold and is essential for viability at low temperatures.* Proceedings of the national academy of sciences, 2002. **99**(15): p. 9727-9732.

206. Potter, P., J. Meek, and N.H. Neff, *Acetylcholine and choline in neuronal tissue measured by HPLC with electrochemical detection.* Journal of neurochemistry, 1983. **41**(1): p. 188-194.

207. Yap, L.-P., et al., *Determination of GSH, GSSG, and GSNO using HPLC with electrochemical detection.* Methods in enzymology, 2010. **473**: p. 137-147.

208. Flanagan, R.J., D. Perrett, and R. Whelpton, *Electrochemical detection in HPLC: Analysis of drugs and poisons*. Vol. 10. 2005: Royal Society of Chemistry.

209. Arya, S.K. and P. Estrela, *Recent advances in enhancement strategies for electrochemical ELISA-based immunoassays for cancer biomarker detection.* Sensors, 2018. **18**(7): p. 2010.

210. Pang, Y.-H., et al., *Rolling circle amplified DNAzyme followed with covalent organic frameworks: Cascade signal amplification of electrochemical ELISA for alfatoxin M1 sensing.* Electrochimica Acta, 2020. **341**: p. 136055.

211. Ruiz-Vega, G., et al., *Electrochemical lateral flow devices: towards rapid immunomagnetic assays.* ChemElectroChem, 2017. **4**(4): p. 880-889.

212. Van Amerongen, A., et al., *Lateral flow immunoassays*, in *Handbook of Immunoassay Technologies*. 2018, Elsevier. p. 157-182.

213. Liew, J.W.Y., et al., *Synthesis and characterization of modified κ-carrageenan for enhanced proton conductivity as polymer electrolyte membrane.* Plos one, 2017. **12**(9): p. e0185313.

214. Imran, M., et al., *Emerging applications of porphyrins and metalloporphyrins in biomedicine and diagnostic magnetic resonance imaging.* Biosensors, 2018. **8**(4): p. 95.

215. Zhao, Y., et al., *Porphyrin-based metal–organic frameworks: protonation induced Q band absorption.* Nanoscale, 2019. **11**(25): p. 12250-12258.

216. USDA-FSIS, *Summary of Recall Cases in Calendar Year 2018.* 2020.

217. Medalla, F., et al., *Estimated incidence of antimicrobial drug–resistant nontyphoidal Salmonella infections, United States, 2004–2012.* Emerging infectious diseases, 2017. **23**(1): p. 29.

218. Wei, Q., et al., *Rapid detection and control of psychrotrophic microorganisms in cold storage foods: A review.* Trends in Food Science & Technology, 2019. **86**: p. 453-464.

219. Ding, S. and M. Schumacher, *Sensor monitoring of physical activity to improve glucose management in diabetic patients: a review.* Sensors, 2016. **16**(4): p. 589.

220. Nag, A., A. Mitra, and S.C. Mukhopadhyay, *Graphene and its sensor-based applications: A review.* Sensors and Actuators A: Physical, 2018. **270**: p. 177-194.

221. Xu, J., Y. Wang, and S. Hu, *Nanocomposites of graphene and graphene oxides: synthesis, molecular functionalization and application in electrochemical sensors and biosensors. A review.* Microchimica Acta, 2017. **184**(1): p. 1-44.

222. Yusoff, N., et al., *Gold nanoparticle based optical and electrochemical sensing of dopamine.* Microchimica Acta, 2015. **182**(13): p. 2091-2114.

223. Sonker, M., V. Sahore, and A.T. Woolley, *Recent advances in microfluidic sample preparation and separation techniques for molecular biomarker analysis: A critical review.* Analytica chimica acta, 2017. **986**: p. 1-11.

224. Jadhav, S.R., et al., *Identification of putative biomarkers specific to foodborne pathogens using metabolomics*, in *Foodborne bacterial pathogens*. 2019, Springer. p. 149-164.

225. Howells, A.M., et al., *Role of trehalose biosynthesis in environmental survival and virulence of Salmonella enterica serovar Typhimurium.* Research in microbiology, 2002. **153**(5): p. 281-287.

226. Postma, P., H. Keizer, and P. Koolwijk, *Transport of trehalose in Salmonella typhimurium.* Journal of bacteriology, 1986. **168**(3): p. 1107-1111.

227. Maréchal, L.R., *Transport and metabolism of trehalose in Escherichia coli and Salmonella typhimurium.* Archives of microbiology, 1984. **137**(1): p. 70-73.

228. Li, H., et al., *Transcriptomic analysis of Salmonella desiccation resistance.* Foodborne Pathogens and Disease, 2012. **9**(12): p. 1143-1151.

229. Murray, D., Y. Hayashida, and K. Nishimura, *Trehalose analysis using ion exchange HPLC coupled with electrochemical detection.* Biotechnology techniques, 1997. **11**(4): p. 269-270.

230. Tabrizi, M.A. and M. Shamsipur, *A label-free electrochemical DNA biosensor based on covalent immobilization of salmonella DNA sequences on the nanoporous glassy carbon electrode.* Biosensors and Bioelectronics, 2015. **69**: p. 100-105.

231. Singh, A., et al., *DNA functionalized direct electro-deposited gold nanoaggregates for efficient detection of Salmonella typhi.* Bioelectrochemistry, 2015. **105**: p. 7-15.

232. Ke, Q. and J. Wang, *Graphene-based materials for supercapacitor electrodes–A review.* Journal of Materiomics, 2016. **2**(1): p. 37-54.

233. Iro, Z.S., C. Subramani, and S. Dash, *A brief review on electrode materials for supercapacitor.* Int. J. Electrochem. Sci, 2016. **11**(12): p. 10628-10643.

234. Xia, J., et al., *Measurement of the quantum capacitance of graphene.* Nature nanotechnology, 2009. **4**(8): p. 505-509.

235. Wang, X., et al., *Rolling up graphene oxide sheets into micro/nanoscrolls by nanoparticle aggregation.* Journal of Materials Chemistry, 2012. **22**(34): p. 17441-17444.

236. Chen, J., et al., *An improved Hummers method for eco-friendly synthesis of graphene oxide.* Carbon, 2013. **64**: p. 225-229.

237. Vangari, M., T. Pryor, and L. Jiang, *Supercapacitors: review of materials and fabrication methods.* Journal of Energy Engineering, 2013. **139**(2): p. 72-79.

238. Borenstein, A., et al., *Carbon-based composite materials for supercapacitor electrodes: a review.* Journal of Materials Chemistry A, 2017. **5**(25): p. 12653-12672.

239. Haq, I., P. Mazumder, and A.S. Kalamdhad, *Recent advances in removal of lignin from paper industry wastewater and its industrial applications–A review.* Bioresource Technology, 2020. **312**: p. 123636.

240. Yang, Q., et al., *Fabrication of high-concentration and stable aqueous suspensions of graphene nanosheets by noncovalent functionalization with lignin and cellulose derivatives.* The Journal of Physical Chemistry C, 2010. **114**(9): p. 3811-3816.

241. Zhang, W., et al., *Lignin Laser Lithography: A Direct-Write Method for Fabricating 3D Graphene Electrodes for Microsupercapacitors.* Advanced Energy Materials, 2018. **8**(27): p. 1801840.

242. Hesas, R.H., et al., *The effects of a microwave heating method on the production of activated carbon from agricultural waste: A review.* Journal of Analytical and Applied pyrolysis, 2013. **100**: p. 1-11.

243. Correa, C.R., T. Otto, and A. Kruse, *Influence of the biomass components on the pore formation of activated carbon.* Biomass and bioenergy, 2017. **97**: p. 53-64.

244. Shi, Y., et al., *Rapid Production of Thermally Exfoliated Graphene with a Large Specific Surface Area by Introducing a Spray Predrying Process.* Industrial & Engineering Chemistry Research, 2021.

245. Manoratne, C., S. Rosa, and I. Kottegoda, *XRD-HTA, UV visible, FTIR and SEM interpretation of reduced graphene oxide synthesized from high purity vein graphite.* Material Science Research India, 2017. **14**(1): p. 19-30.

246. Ghosh, S., et al., *Mesoporous carbon nanofiber engineered for improved supercapacitor performance.* Korean Journal of Chemical Engineering, 2019. **36**(2): p. 312-320.